TriDurLE

National Center for Transportation Infrastructure Durability & Life-Extension

Project ID: 2020-UCD-01 **Grant # 69A3551947137**

Fiber Reinforced Polymer (FRP) Seismic Retrofit of Reinforced Concrete Bridge Columns Vulnerable to Long-Duration Subduction Zone Earthquakes

By

William Nickelson
Ruben Jerves
Christopher Motter, co-PI
Adam Phillips, co-PI

Department of Civil and Environmental Engineering
Washington State University
Pullman, WA 99164

for

National University Transportation Center TriDurLE
Department of Civil & Environmental Engineering
405 Spokane Street PO Box 642910
Washington State University Pullman, WA 99164-2910

May 2022

Acknowledgments

This report is based on a thesis by William Nickelson in partial fulfillment of the requirements for a M.S. degree from Washington State University. This research was sponsored by the National Center for Transportation Infrastructure Durability & Life-Extension at Washington State University and by the U.S. Department of Transportation. This support is gratefully acknowledged. Simpson Strong Tie (SST) is thanked for providing in-kind donations of fiber reinforced polymer and resin, in addition to installation of the steel jackets used in the test columns. Nucor is thanked for in-kind donations of Grade 40 reinforcement used in the test columns. Scott Lewis, Joshah Jennings, Levi Arnold, and Roshan Ghimire are thanked for assistance with laboratory testing.

Disclaimer

Table of Contents

List of Figures

List of Tables

Executive Summary

Many bridges in the western United States, including those built for the Interstate Highway System in the 1950s and 1960s, have seismically vulnerable reinforced concrete (RC) columns. The seismic performance of many of these bridges is essential to post-earthquake mobility, as bridges are relied upon as critical lifelines into urban centers after natural disasters. Some states, including California and Washington, have introduced retrofit programs to enhance the seismic ductility of vulnerable columns. The retrofit involves wrapping the column with either a structural steel or fiber reinforced polymer (FRP) jacket, which enhances the deformation capacity of the column to improve the seismic performance. Previous research on jacketed columns has focused on strike-slip earthquakes, rather than long-duration, subduction-type earthquakes that are characteristic of the Cascadia Subduction Zone.

This research was focused on characterization of the behavior of FRP jacketed bridge columns under long-duration earthquakes. Six tests were conducted on cantilever bridge columns with FRP jackets at the base. The FRP jackets were 0.40” and extended over a height of one column diameter. The FRP had specified strength of 128-ksi and elastic modulus of 14.2ksi in the circumferential direction. Test variables for the columns included longitudinal reinforcement ratio, longitudinal bar diameter, axial load ratio, and loading protocol. All tested columns had lateral deformation capacity of at least 6% drift, with lateral deformation capacity considered to occur at 20% strength loss. Axial failure was not achieved in any of the test columns, and the tests were stopped after multiple cycles at 10% drift. Five of the six test columns were nominally identical to a set of previously tested columns with FRP jackets. The lateral deformation capacity of each column with an FRP jacket met or exceeded that of the equivalent column with a steel jacket.

A model was formulated to predict the deformation capacity of FRP jacketed columns. The model included a column model followed by a fatigue model to estimate bar fracture. The column was modeled in OpenSees using an elastic beam column element over the height of the column, with two zero-length bond slip elements at the base. The two elements represented bond slip of longitudinal reinforcement from the footing and from the jacketed column. The OpenSees model was run to determine the stress-strain history in the outermost longitudinal reinforcement. The strain history was used in a fatigue model to predict the drift at fracture of the first longitudinal bar. The modeling approach was validated to test data from the experimental study. The model was used to estimate the deformation capacity of FRP jacketed bridge columns.

1. Introduction

1.1. Problem Statement

Significant damage to reinforced concrete bridge columns was observed following the 1971 San Fernando, CA earthquake (Fung et al, 1971). Subsequent research led to an improved understanding of the design issues, and, in 1983, AASHTO issued new bridge design guidelines with changes aimed at addressing the issue of nonductile bridge columns in new construction. The seismic vulnerabilities of pre-1971 bridge columns were again exposed by the 1989 Loma Prieta, CA (NIST, 1990; EERI, 1990) and 1994 Northridge, CA earthquakes (EERI, 1994; Buckle, 1994). Based on the damage observed in these earthquakes and research on the topic, it is clear that there is a need for seismic retrofit of pre-1971 reinforced concrete bridge columns in areas of high seismicity. Many bridges in the U.S. were constructed prior to 1971, including state bridges constructed in the 1950s and 1960s as part of the national Interstate Highway System. These bridges represent important lifelines for cities in the aftermath of a large earthquake.

Deficiencies in pre-1971 reinforced concrete bridge columns include insufficient lap splice lengths of 20 times the longitudinal reinforcement diameter (i.e., $20d_b$), inadequate shear strength, and inadequate flexural ductility due to insufficient transverse reinforcement (typically #4 hoops at 12” hoops) (Chai et al, 1991). Initial research on retrofit of seismically deficient bridge columns focused on the use of steel jackets (Chai et al, 1991; Priestley et al, 1994a,b), and this research led to field implementation in Washington and California. For circular columns, the jackets were typically installed by seam welding two half-plates of semi-circular cross-section. The jackets were oversized, and the gap that was left between the jacket and the column, which was typically 1-2”, was filled with grout. For rectangular columns, the jackets were elliptical, and concrete was used to fill the voids between the jacket and the column. If enhancement to column shear strength was needed to prevent shear failure, the jackets were provided over the full height of the column. Alternatively, the jackets were provided only in plastic hinge zones (i.e., at the base of the column for cantilevers, and at the top and the bottom of the column for fixed-fixed columns) if enhancement to shear strength was not needed. In this case, the jackets can provide adequate confinement to prevent splice failure of $20d_b$ lap splices and to prevent crushing of concrete. A small gap (~2”) was left between the base of the steel jacket and the footing in order to avoid contact that would allow load transfer between the footing and the jacket as the column deforms under earthquake demands.

Recommendations on steel jacket design are provided in the FHWA guidelines (2006) and stem from research (Chai et al, 1991; Priestley et al, 1994a,b). The recommendations specify the jacket thickness needed to prevent concrete crushing or splice failure. If these failure modes are avoided, fatigue failure of longitudinal reinforcement is expected to occur at the gap between the bottom of the steel jacket and the top of the footing. Chai et al (1991) determined that load sharing was occurring between the steel jacket and the column, such that the jacket provided an enhancement to flexural strength. The enhancement to flexural strength limited the spread of plasticity, and Chai et al (1991) recommended that the zone of plasticity (i.e., plastic hinge length) could be modeled as being equal to the gap length between the jacket and the footing plus bond slip of the longitudinal reinforcement into the footing and into the steel jacket.

Much of the research on steel jackets was conducted in the 1990s, at a time when steel jackets were a more cost-efficient option relative to fiber reinforced polymer (FRP). FRP has become less cost inhibitive with time, and the use of FRP jackets is particularly beneficial in cases where a steel jacket retrofit may be inadequate. FRP jackets may offer an advantage over steel jackets by better accommodating the vertical spread of plasticity, which may be achieved by orienting the FRP fibers in the circumferential direction. The improved spread of plasticity leads to a larger plastic hinge length. This means that for a given curvature demand at the base of the column, the FRP jacket accommodates a larger deformation capacity than the steel jacket, leading to a reduced collapse likelihood in earthquakes. Previous research has not focused on the behavior of FRP jacketed columns in long duration earthquakes. Existing models to predict the deformation capacity of FRP jacket retrofitted columns based on fatigue failure of reinforcement do not exist.

1.2. Objectives

The first objective of the research was to experimentally assess the deformation capacity of FRP jacketed bridge columns, with properties characteristic of Washington State bridges, subjected to Cascadia Subduction Zone earthquake demands. The second objective was to formulate a model to determine the deformation capacity of FRP jacket retrofitted bridge columns. The model was intended to be suitable for use in nonlinear time history analyses, making it a suitable tool for analyzing the behavior of FRP jacket retrofitted bridge columns in a given earthquake ground motion. The data needed for model calibration/validation was generated from the experimental program. Six approximately one-half-scale to two-thirds-scale bridge columns with FRP jacket retrofits were constructed and tested. The test program was intended to address gaps from previous studies by including the range of practical parameters that influence column deformation capacity. A lumped plasticity model for the retrofitted columns was developed and validated with experimental results. In this model, deformation capacity was based on fatigue fracture of reinforcement.

1.3. Expected Contributions

Results from testing of FRP jacketed columns were used to provide an assessment of the deformation capacity of WSDOT bridge columns in Cascadia Subduction Zone earthquakes. The tests produced a unique dataset for FRP jacketed columns subjected to long duration earthquake demands that may be used for model calibration/validation. The model formulated in this study was validated to this data. This model may be used to assess the failure probability of any FRP jacket retrofitted bridge column for a given earthquake ground motion, making it a useful tool to aid in the design of FRP retrofits. This study addresses TriDurle research thrust #5: Addressing natural hazards and extreme disaster events that threaten the durability and service life of transportation infrastructure.

1.4. Report Overview

This report includes five chapters and a list of references. An introduction is provided in Chapter 1, and a literature review is provided in Chapter 2. The experimental study is presented in Chapter 3, which included two subsections. An overview of the experimental program was provided in the first subsection. This included methods of construction, testing, and material properties. Test results were provided and discussed in the second subsection. This included a summary of damage, load-deformation column response, stiffness, reinforcement strains, column curvatures, and components of deformation. Information on column modeling was provided in Chapter 4, which also included two subsections. A description of the column model was provided in the first subsection, with model validation described in the second subsection. A summary and list of conclusions are provided in Chapter 5. A list of references follows Chapter 5.

2. Literature Review

A number of previous experimental studies have been conducted on circular reinforced concrete columns with FRP jackets. Xiao and Ma (1997) tested three columns that had longitudinal reinforcement at the base of the column with lap splice lengths of 20 times the bar diameter. Two of the three columns were retrofit with FRP jackets prior to testing. The unretrofitted column failed due to lap splice failure at low ductility. This column was repaired, retrofit with FRP, and tested again. For all three retrofitted columns, the level of confinement provided by the jackets was such that bond failure occurred gradually, allowing for ductility demands in the range of four to six at 20% loss of lateral load-carrying capacity. Xiao and Ma (1997) used the test results to develop and validate a deformation capacity model that accounted for the influence of confinement on bond slip in the splice region.

Haroun and Elsanadedy (2005a,b) conducted tests on FRP jacketed circular columns that also had lap splice lengths of 20 times the longitudinal bar diameter. The jackets used were such that the reported failure occurred due to concrete crushing or longitudinal bar buckling rather than bond. Similar failure modes were reported for the tests of Ghosh and Sheikh (2007).

For FRP jacket retrofit of reinforced concrete bridge columns, failure may occur due to concrete crushing accompanied by jacket rupture or low-cycle fatigue fracture of longitudinal reinforcement. The likelihood of jacket rupture is mitigated by providing a jacket of suitable thickness based on the Mander et al (1988) confined concrete model, which is reflected in the

FHWA guidelines (2006). It is shown in Section x on column modeling that for cases in which reinforcement fatigue fracture governs failure, the parameters that impact column deformation capacity are the neutral axis depth (influenced by the axial load ratio and longitudinal reinforcement ratio), plastic hinge length (influenced by the longitudinal bar diameter and column diameter), and the loading history. Systematic variation of these parameters is not evident from the summary of previous tests provided in Table 1, and the proposed experimental program is intended to address this issue.

Previous experimental programs (Xiao and Ma, 1997; Haroun and Elsanadedy, 2005a,b; Ghosh and Sheikh, 2007; Breña and Schlick, 2007) used loading protocols that were developed using strike-slip earthquake ground motions (e.g., Krawinkler, 1992). Subduction zone earthquakes produce longer duration ground motions than strike-slip earthquakes, which results in greater cumulative plastic deformation in flexure-yielding components and the increased potential for fatigue failure. The USGS has recently released updated hazard maps that require increased levels of seismicity for structural design in regions affected by the Cascadia Subduction Zone (CSZ). These new maps reflect the geologic evidence indicating that the CSZ is capable of producing M9 megathrust earthquakes at the interface between the Juan de Fuca and North American plates (Atwater et al. 1995). Such an event has a 10-14% chance of occurring in the next 50 years (Goldfinger et al. 2012). In an M9 CSZ earthquake, strong ground shaking is expected in Washington, Oregon, northern California, and Alaska. Due to the lack of an accurate metric to assess the deformation capacity of FRP jacket retrofitted columns, there is uncertainty as to the expected performance of retrofitted bridge columns in Cascadia Subduction Zone earthquakes. The proposed research will result in the development of a new model that may be used to determine if and when a FRP jacketed bridge column fails under a specific seismic demand, such as a CSZ-type ground motion. The model will be calibrated/validated using test data generated through an experimental study on FRP jacketed columns. The tests are expected to generate a unique dataset for model calibration relative to data that is available from previous tests. Specifically, the columns will be tested under loading protocols reflective of long-duration earthquakes. Past experimental studies on RC columns with FRP jackets (Xiao and Ma, 1997; Haroun and Elsanadedy, 2005a,b; Ghosh and Sheikh, 2007; Breña and Schlick, 2007) have not considered long-duration earthquake demands. In addition to the difference in loading protocol, the level of FRP confinement used for the test columns in the proposed study will be higher than that typically used in previous studies. In previous studies, failure typically occurred due to concrete crushing or longitudinal reinforcement buckling. The combination of increased confinement and increased cycle content for the columns in the proposed study is expected to produce fatigue failure of reinforcement. Furthermore, direct comparison between steel jackets and FRP jackets has not been considered in an experimental study that isolates this test variable. To address this shortcoming, the six FRP jacketed columns tested as part of the proposed research were identical to a set of six steel jacketed columns tested by the P.I.’s as part of a study funded by WSDOT.

Table 2.1: Parameters of Past Tests on Reinforced Concrete Circular Bridge Columns Retrofitted with FRP Jackets

Experimental Program	Specimen Name	Total Longitudinal Steel Area/ Gross Concrete Area	Axial Load Ratio, P/(Agf'c)	Diameter or Length	Shear Span Ratio (M /VD or M/VL)	Longitudinal Bar Diameter (inches)	Lap Splice Length / Longitudinal Bar Diameter	FRP Thickness (inches)	FRP Ultimate Stress (ksi)	FRP Elastic Modulus (ksi)
Xiao and Ma (1997)	C2-RT4	0.0195	0.050	24	4	0.75	20	0.5	80	7000
Xiao and Ma (1997)	C3-RT5	0.0195	0.050	24	4	0.75	20	0.625	80	7000
Haroun and Elsanadedy (2005a)	CF-R1	0.0195	0.061	24	6	0.75	20	0.028	604	33568
Haroun and Elsanadedy (2005a)	CF-R2	0.0195	0.060	24	6	0.75	20	0.028	642	33365
Haroun and Elsanadedy (2005a)	CF-R3	0.0195	0.067	24	6	0.75	20	0.449	108	5293
Haroun and Elsanadedy (2005a)	CF-R4	0.0195	0.059	24	6	0.75	20	0.067	635	32770
Haroun and Elsanadedy (2005a)	CF-R5	0.0195	0.056	24	6	0.75	20	0.5	93	5278
Haroun and Elsanadedy (2005a)	CF-R6	0.0195	0.067	24	6	0.75	20	0.327	136	9135
Haroun and Elsanadedy (2005b)	CS-R1	0.0195	0.054	24	2	0.75	20	0.028	604	33568
Haroun and Elsanadedy (2005b)	CS-R2	0.0195	0.056	24	2	0.75	20	0.028	642	33365
Haroun and Elsanadedy (2005b)	CS-R3	0.0195	0.065	24	2	0.75	20	0.406	61	2683
Haroun and Elsanadedy (2005b)	CS-R4	0.0195	0.059	24	2	0.75	20	0.047	181	15051
Ghosh and Sheikh (2007)	CAF1-2N	0.0172	0.050	14	5.65	0.75	24.67	0.04	148	11458
Ghosh and Sheikh (2007)	CAF1-5N	0.0172	0.270	14	5.65	0.75	24.67	0.04	148	11458
Ghosh and Sheikh (2007)	CBF1-6N	0.0172	0.050	14	5.65	0.75	24.67	0.04	148	11458
Brena Schlick (2007)	CFRP-05	0.0254	0.050	9.5	4.5	0.5	24	0.0065	550	33000
Brena Schlick (2007)	KFRP-05	0.0254	0.050	9.5	4.5	0.5	24	0.011	290	17400
Brena Schlick (2007)	CFRP-15	0.0254	0.150	9.5	4.5	0.5	24	0.0065	550	33000
Brena Schlick (2007)	KFRP-15	0.0254	0.150	9.5	4.5	0.5	24	0.011	290	17400

3. Column Testing

3.1. Methodology

3.1.1. Test Specimen Details

Each test specimen consisted of a column, a footing, and a loading head. A test matrix for the six test columns is provided in Table 3.1, with drawings of the columns provided in Figure 3.1. The test columns were nominally identical to those tested by McGuiness (2021), except that carbon fiber reinforced polymer (CFRP) jackets were used in place of steel jackets. The reinforced concrete column parameters matched those tested by McGuiness (2021), except that C(S)-6.0-#7(1.3)-0.05, the tallest column in the McGuiness (2021) study, was replaced by a column with details identical to C(S)-4.0-#7(1.3)-0.05 and C(S)-4.0-#7(1.3)-0.05-EQ. Test variables in the experimental study included longitudinal reinforcement diameter, longitudinal reinforcement ratio, axial load ratio, and loading protocol. Design parameters among the test columns are inherent in the naming convention. For example, C(CFRP)-4.0-#7(1.3)-0.05 designates a circular column with CFRP jacket in "C(CFRP)", with a "4.0" span to depth ratio (H/D = 4.0), using "#7" longitudinal reinforcement with 1.3% longitudinal reinforcement ratio (A_s/A_g = 0.013), and 5% axial load ratio ($P/(f'_c A_g)$ = 0.05). A fully reversed cyclic loading protocol was used for five of the six columns, whereas C(CFRP)-4.0-#7(1.3)-0.05-EQ was subjected to a loading history determined from analysis of a bridge to a specific earthquake. C(CFRP)-4.0-#7(1.3)-0.05-2X was subjected to twice the number of cycles at each increment as C(CFRP)-4.0-#7(1.3)-0.05. More details on the loading protocols are provided in Section 3.6. The columns were tested as cantilevers, and the column height, *H*, was the measured distance from the top of footing to the line of action of the applied lateral load. The height of the circular column section was 9” less than *H* to facilitate inclusion of the loading head. Column diameter, *D*, was 24”. All test columns had nominally identical 1” clear cover, c_b, Grade 40 longitudinal and transverse reinforcement, and #3 hoops with a lap-splice length, l_b, of 16” and center-to-center vertical spacing, *s*, of 8” used as transverse reinforcement. No hooks were provided on transverse reinforcement lap splices.

The footing and loading head were consistent with those used in the McGuiness (2021) tests, with details provided in Figure 3.2 and Figure 3.3. C(CFRP)-4.0-#7(1.3)-0.05-2X, which did not have an equivalent test in the McGuiness (2021) study, had the same footing as C(CFRP)-4.0-#7(1.3)-0.05. Voids were provided in the footing using SCH40 PVC pipe, located as shown in Figure 3.3, to allow the footing to be post-tensioned to the laboratory strong floor and to facilitate lifting and moving of the test specimens before and after testing.

The CFRP jackets were designed to provide a level of confinement stiffness that was greater than that provided by the 3/16” steel jackets used in the columns tested by McGuiness (2021). The specified CFRP modulus of elasticity was 14,200 ksi in the CFRP direction that was oriented circumferentially around the columns. Five sheets of 0.08” thick CFPR were used, resulting in a thickness of 0.40”, which provides circumferential stiffness of 14,200 ksi * 0.40” = 5,680 k/in relative to 29,000 ksi * 0.1875” = 5,437.5 k/in for the steel jacket. The CFRP jackets were used over the lower 24” inches of the column, which is the column diameter. The steel jackets used in the columns tested by McGuiness spanned the full circular portion of the column, with the exception of a 1” gap at the top and bottom.

Table 3.1: Test Matrix

Column I.D.	Long. Bar Size	# Long. Bars	A_s/A_g	$P/(A_g f_c')$	H/D	Loading Protocol
C(CFRP)-4.0-#7(1.3)-0.05	#7	10	0.0133	0.05	4.0	Cyclic
C(CFRP)-4.0-#5(1.4)-0.05	#5	20	0.0137	0.05	4.0	Cyclic
C(CFRP)-4.0-#7(2.7)-0.05	#7	20	0.0265	0.05	4.0	Cyclic
C(CFRP)-4.0-#7(1.3)-0.05-EQ	#7	10	0.0133	0.05	4.0	EQ
C(CFRP)-4.0-#7(1.3)-0.05-2X	#7	10	0.0133	0.05	4.0	2x Cyclic
C9CFRP)-4.0-#7(1.3)-0.15	#7	10	0.0133	0.15	4.0	Cyclic

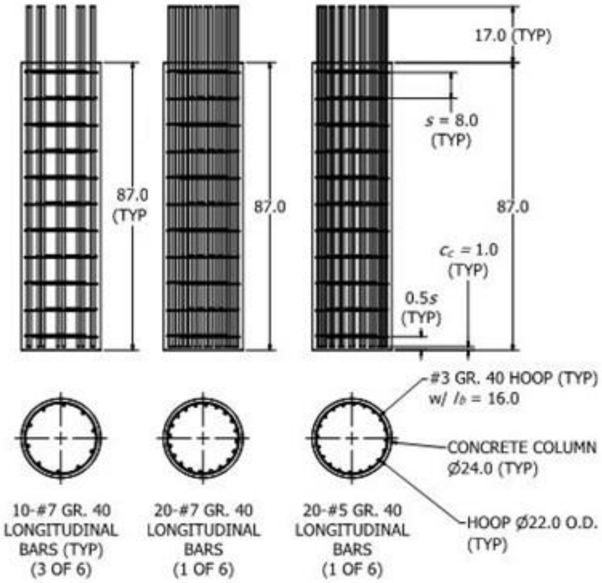

Figure 3.1: Column Reinforcement Layout

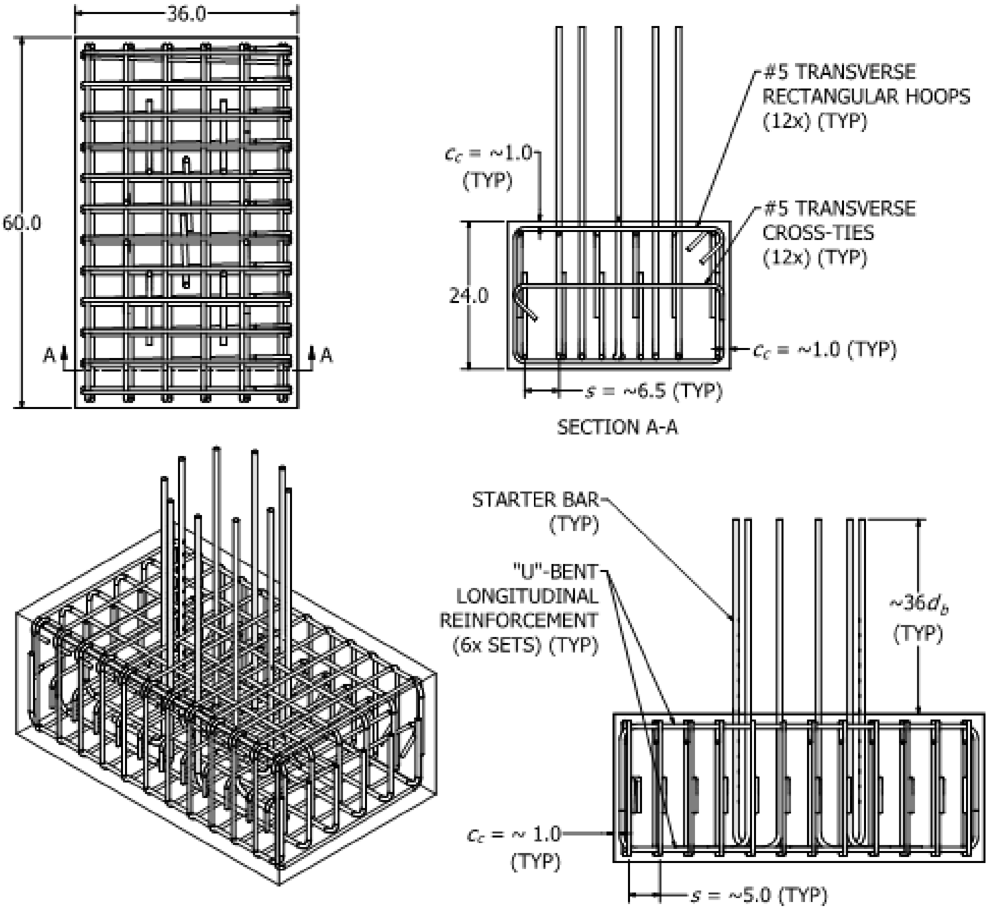

Figure 3.2: General Footing Reinforcement Details (10-#7 Starter Base Depicted) (Dimensions in Inches)

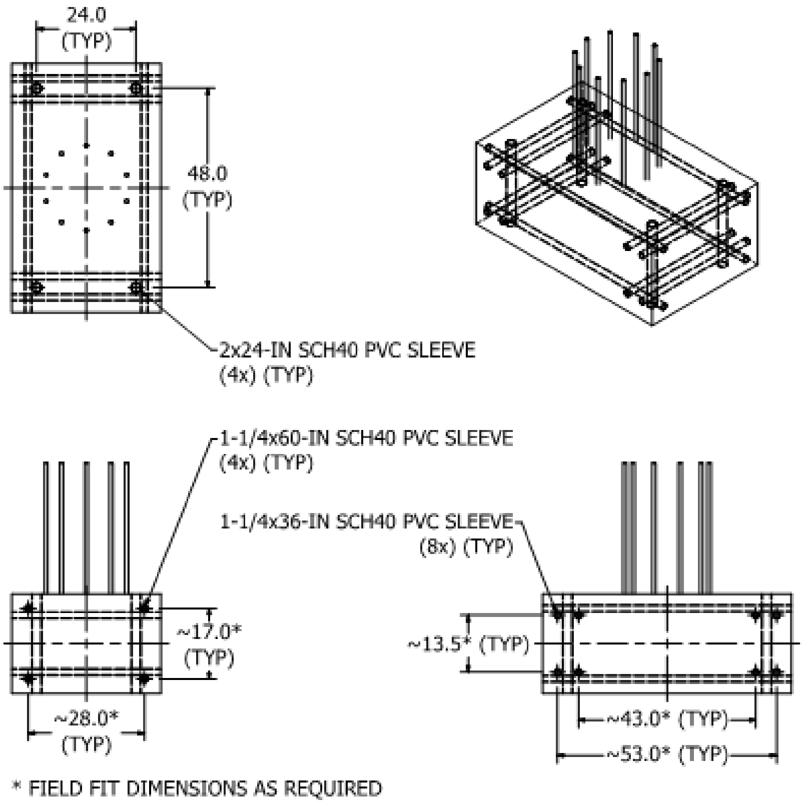

Figure 3.3: Footing Sleeve Details (10-#7 Starter Bars Depicted) (Dimension in Inches)

3.1.2. Test Specimen Construction

Each column was constructed in two pours, with a cold joint at the base of the column. Formwork consisted of 3/4 CDX plywood, 2” x 4” framing lumber, and tubular forms, made from heavy cardboard, for the circular portion of the column. Six sets of forms were constructed, as depicted in Figure 3.4a, to enable pouring from the same load of concrete. Footing reinforcement cages were tied externally prior to being placed inside the formwork. Column starter bars were tied to footing reinforcement while located within the column cross-section using plywood drilled holes for the bars. Strain gauges in the footing concrete were wired away from the footing-column interface. Further description of the strain gauge layout is provided in Section 3.5. Vertical PVC sleeves were precisely located in the footing to match the pattern in the strong floor. Formwork heights allowed direct tailgate delivery of ready-mix concrete for the footing. The cold joint between the footing and subsequent column pour was intentionally roughened to magnitudes greater than ¼-in. The remaining exposed footing surfaces were troweled to a smooth uniform finish. Column reinforcement cages where tied horizontally.

After completion of the footing pours, the column cages were rotated into the vertical position, and affixed to the footing starter bars with contact lap splices of longitudinal reinforcement to starter bars. Spacers were installed on reinforcement, and column forms were then installed by lowering from above. Proper vertical alignment of column forms was provided by timber bracing between the top of the forms to ground level brace points, as depicted in Figure 3.5a. The wires of strain gauges cast into the column, similar to the footing, were routed away from the footing-column interface. Top block formwork was supported by the column formwork and at ground level. Top block transverse reinforcement was tied to column longitudinal reinforcement, and PVC sleeves were installed within top block formwork, as depicted in Figure 3.6b. Due to height, the delivery and placement of concrete to the column formwork required the assistance of a concrete boom truck pump and 12-ft drop hose. Concrete was pumped incrementally, with periodic pauses to raise the pump hose and facilitate vibratory consolidation of the concrete. The exposed top surface was trowel finished. After the appropriate cure time, formwork was removed, including cutting and removing the single-use circular forms.

Several months after column construction, CFRP jackets were installed by a professional team. Installation began with roughening of the concrete surface, using a grinder, to facilitate bond of epoxy to concrete. Dust from roughening was removed from the column using acetone. The CFRP wrap was cut to lengths approximately equal to one circumference of the column plus 12-inches. The epoxy was mixed in batches due to a 1-hour pot life at 70°F (21°C). After the first epoxy batch was mixed, an epoxy primer was applied to the columns using a nap roller. CFRP sheets were hand saturated using plastic trowels. Care was taken to ensure full fiber saturation without saturation so excessive that the sheet would settle once on the column. After saturating the fibers, the sheets were wrapped around the column and the plastic hand trowels were used to remove any entrapped air and excess saturate. The sheet had a lap length of 12-inches, with the lap intended to provide adequate bond. The seams had additional epoxy applied per manufacturer specifications. After the first layer, additional layers were applied with the start of the new layer on the opposite side of the column as the end of the previous layer, such that all seams were offset. After all 5 layers were applied, an epoxy paste was applied as an outer coating, and the columns were given at least 72 hours to cure before testing of the first column. A finished jacket is shown in Figure 3.4. Lacking of bulging in the jacket suggests that epoxy was appropriately applied, with bonding between layers.

Figure 3.4: CFRP Jacket Before Testing for C(CFRP)-4.0-#7(1.3)-0.05

Figure 3.5: Footing Construction

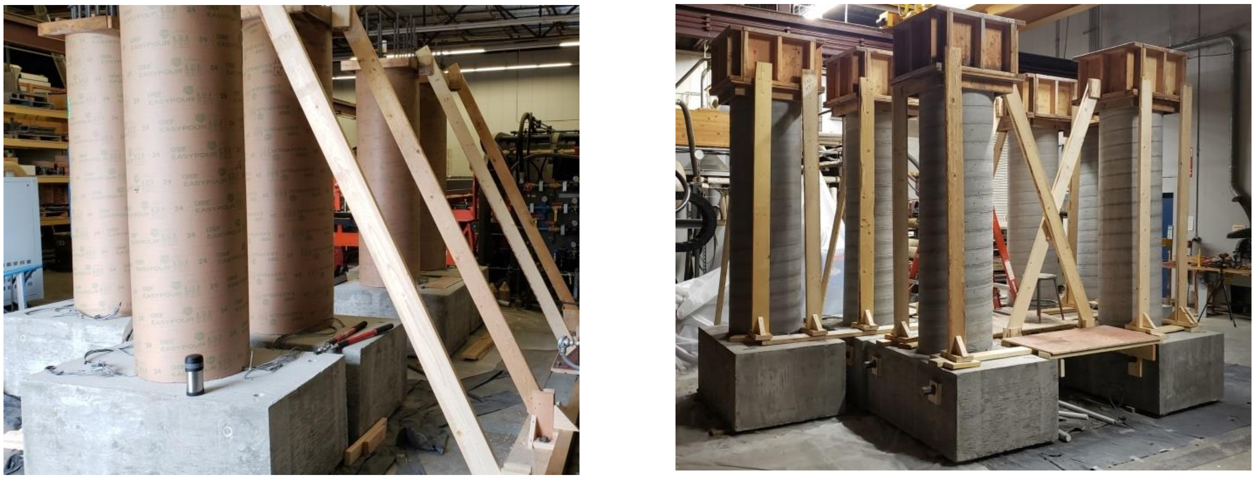

Figure 3.6: Construction: a) Bracing for Column Concrete Pour, and b) Bracing for Top Block Concrete Pour

3.1.3. Material Properties

3.1.3.1. Steel Reinforcement

A batch of #7, #5, and #3 Grade 40 reinforcement was manufactured specifically for this study, such that all column reinforcement in a given size was from the same heat. Three samples of #5 and #7 column longitudinal reinforcement were tested, with resulting stress-strain plots provided in Figure 3.7. Values of the resulting yield strength, f_y, ultimate strength, f_u, and percent elongation, are provided in Table 3.2.

Table 3.2: Measured Properties of Steel Reinforcement Obtained from Tensile Testing

#5 Grade 40				#7 Grade 40			
Sample I.D.	f_y [ksi]	f_u [ksi]	Elongation [%]	Sample I.D.	f_y [ksi]	f_u [ksi]	Elongation [%]
#5 Test 1	48.5	72.0	39	#7 Test 1	46.5	69.0	16
#5 Test 2	52.0	74.5	32	#7 Test 2	51.0	73.0	17
#5 Test 3	51.0	74.0	39	#7 Test 3	51.5	73.0	54
Average	50.5	73.5	36.7		49.8	71.7	29

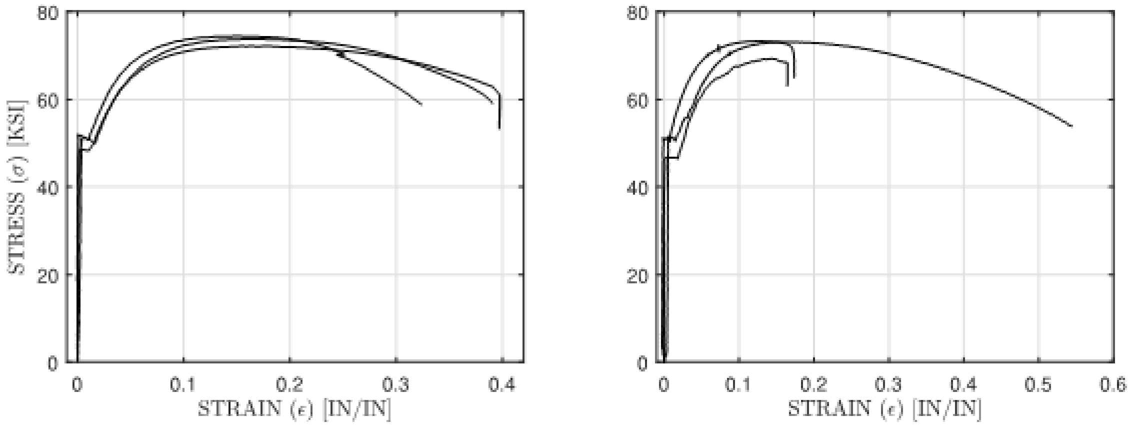

Figure 3.7: Longitudinal Steel Reinforcement Testing: a) #5 Stress-Strain Relationship, b) #7 Stress-Strain Relationship

3.1.3.2. Concrete

A single concrete supplier and mix design were used for the project. The mix used a 3/8-in maximum aggregate to reflect 3/4-in maximum aggregate at full-scale. The footings were poured separately from the columns and loading heads, as described in Section 3.2. 6” x 12” cylinders were prepared for the footing and the columns, respectively. Cylinders were stored in close proximity to the specimens. The footing cylinders were tested at 7-days, with the measured concrete compressive strength provided in Table 3.3. Four cylinders were tested within 3 days of each column test, and the results are provided in Table 3.4. A clear trend of strength increase with time is not evident from the data, and the average concrete compressive strength $(\bar{f}'_{c,test})$ was 3.949-ksi with a coefficient of variation of 0.059.

Table 3.3: Footing Concrete Compressive Strength from Cylinder Testing

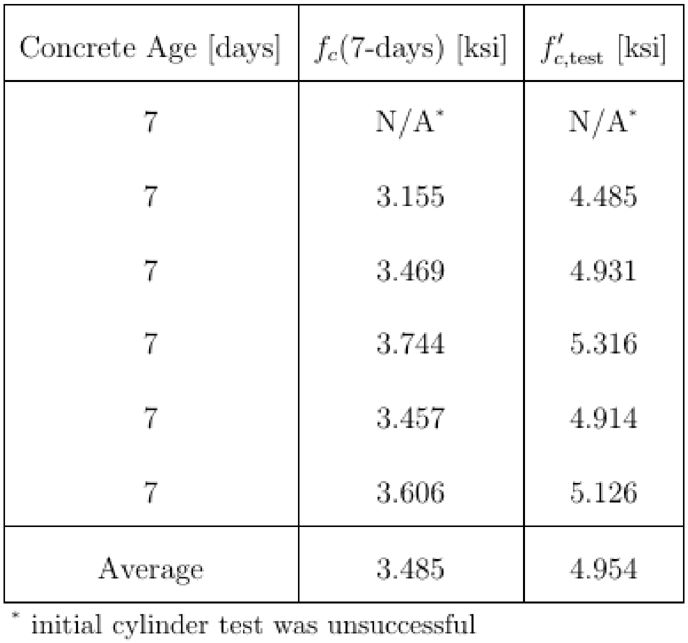

Concrete Age [days]	f_c(7-days) [ksi]	$f'_{c,\text{test}}$ [ksi]
7	N/A*	N/A*
7	3.155	4.485
7	3.469	4.931
7	3.744	5.316
7	3.457	4.914
7	3.606	5.126
Average	3.485	4.954

* initial cylinder test was unsuccessful

Table 3.4: Column Concrete Compressive Strength from Cylinder Testing

Column	Cylinder 1 f’c [ksi]	Cylinder 2 f’c [ksi]	Cylinder 3 f’c [ksi]	Cylinder 4 f’c [ksi]	Average f’c [ksi]	SD [ksi]
C(CFRP)-4.0-#7(1.3)-0.05	3.719	3.552	3.980	3.804	3.764	0.178
C(CFRP)-4.0-#5(1.4)-0.05	4.089	4.119	3.929	-	4.046	0.102
C(CFRP)-4.0-#7(2.7)-0.05	4.053	3.505	3.735	3.678	3.743	0.229
C(CFRP)-4.0-#7(1.3)-0.05-EQ	3.742	3.545	4.232	3.715	3.809	0.295
C(CFRP)-4.0-#7(1.3)-0.05-2X	4.478	4.295	4.038	3.821	4.158	0.288
C(CFRP)-4.0-#7(1.3)-0.15	3.851	3.997	4.447	4.405	4.175	0.296
Cumulative Average					3.949	0.232

3.1.3.3. Carbon Fiber Reinforced Polymer (CFRP)

Each CFRP jacket was comprised of Simpson Strong-Tie CSS-CUCF44, which is a unidirectional carbon fabric designed to be laminated with CSS-ES and CSS-UES saturant. It is specified to have 10% of the strength properties in the minor direction than the major direction. The major direction was oriented around the circumferences of the columns. Table 3.5 provides properties for the major direction, as specified in the ICC Report ESR-3404 (ICC ES, 2022).

Table 3.5: CFRP Properties in Major Direction

Property	Value
Dry Fiber Tensile Strength	670,000 psi
Dry Fiber Tensile Modulus	37,000,000 psi
Dry Fiber Elongation at Break	1.9 %
Dry Fiber Unit Weight	44.0 oz./yd.^{2}
Cured Composite Tensile Strength	128,000 psi
Cured Composite Tensile Modulus	14,200,000 psi
Cured Composite Elongation at Break	0.9 %
Cured Composite Thickness per Layer	0.08 in.

3.1.4. Test Set-Up

Using the set-up shown in Figure 3.8, tests were conducted in the Simpson Strong-Tie Experimental Testing Laboratory, which is part of the Composite Materials and Engineering Center (CMEC) at Washington State University. Prior to testing, the footing block of each test column was post-tensioned to the laboratory strong floor. A pair of steel channels spanning over each end of the footing blocks were used to engage more floor anchors. During testing, constant axial load and cyclic lateral displacement were applied to the test column. Lateral load and displacement was applied using a servo-controlled hydraulic actuator with 40-in stroke and capacity of 220-k in tension and 328-k in compression. The lateral actuator was post-tensioned to the top of the test column and was reacted by the laboratory strong wall. Axial load was applied using 60-ton hydraulic jack(s) manually controlled by a self-contained hydraulic power unit. Load was controlled through a pressure regulating valve integral with the power unit and monitored with 100-k low profile load cell(s). As shown in Figure 3.10, a single jack and load cell were used for five of the six tests, while three jacks and load cells were used for C(CFRP)-

4.0-#7(1.3)-0.05 due to the higher axial load. The application of vertically oriented axial load to simulate P-delta was a unique feature of this program relative to much of the prior research (e.g., Haroun and Elsanadedy, 2005), which used tendons anchored to the strong floor to apply axial load. Utilizing a roller and swiveling knuckle assembly, as depicted in Figure 3.9, the applied axial load was able to translate with the top of the column to remain vertical. A steel frame, comprised of four steel framing columns and three beams, was used to react the applied axial load and to prevent out of plane movement of the test column. The standard axial load configuration (5 of 6 tests) is depicted in Figure 3.9. The column with large axial load set-up configuration required an additional axial load roller and larger capacity clevis assembly. Additionally, steel plates were added between the test column and loading beam to distribute and collect the greater axial loads.

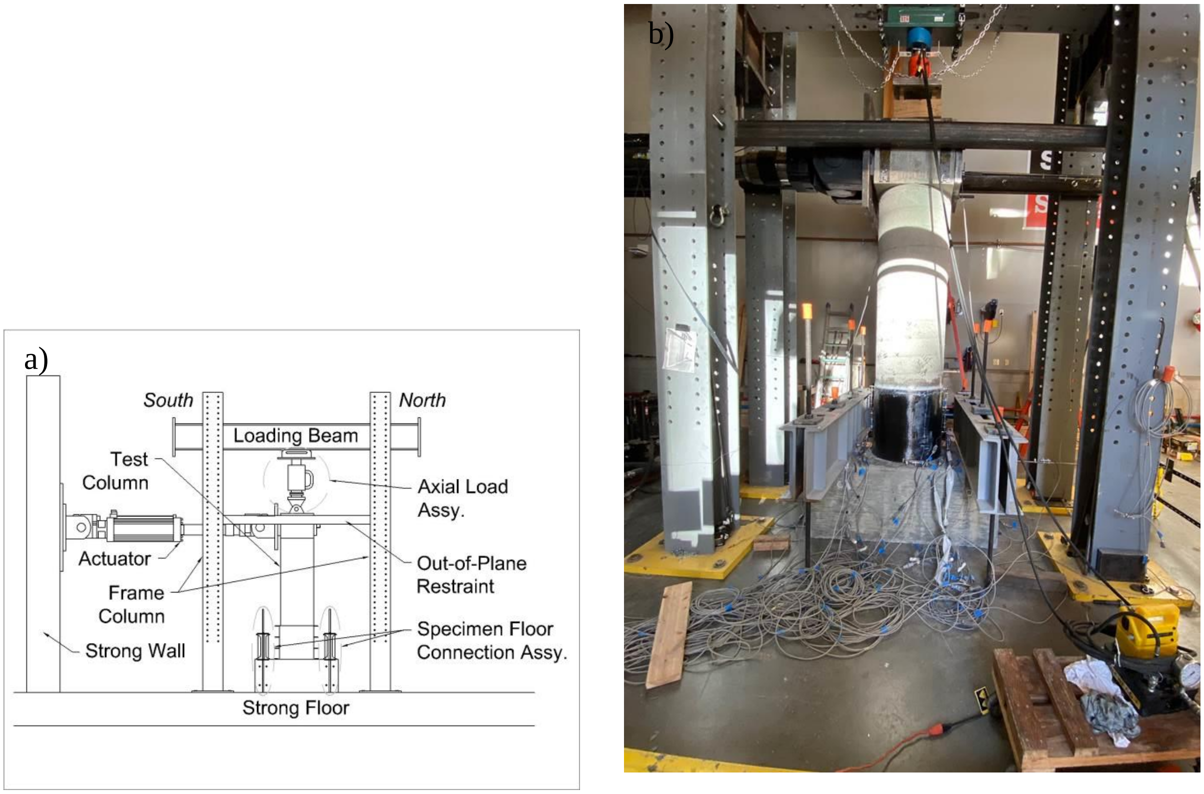

Figure 3.8: Test Set-up, $\frac{P_d}{A_g f'_c} = 0.05$: a) Schematic, b) Photo

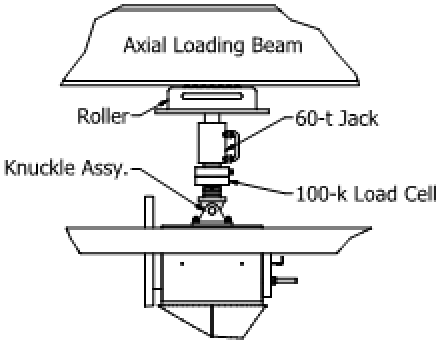

Figure 3.9: Axial Load Setup, $\frac{\boldsymbol{P_d}}{\boldsymbol{A_g f'_c}} = \mathbf{0.05}$

3.1.5. Instrumentation

Forces, strains, and displacements were recorded during testing. Five of the six tests used a single 100-k load cell to measure axial load, while the test column with higher axial load used three 100-k load cells. Displacement measurements of the column and footing relative to a stationary reference frame were obtained from linear variable differential transducers (LVDTs) and string potentiometers at the locations shown in Figure 3.10. Rotation of the footing was determined based on two vertical sensors located at each end of the footing. LVDTs spanning between the footing and 0.5-in above the footing were used to measure column sliding in the horizontal direction and bond slip in the vertical direction. Axial-flexural deformations within the jacketed region were measured using vertical sensors at the locations shown in Figure 3.13. To attach LVDTs, ¼-in threaded instrumentation rods were installed into the column core concrete by drilling approximately ½-inch diameter holes approximately 1” deep into the column and inserting the threaded instrumentation rods with fast drying epoxy. Post-installed ¼-in wedge anchors were alternatively used at the footing and loading head and at the relative measurements bridging the gaps between the footing-column and column-loading head.

For each column, 14 strain gauges were installed on each of the two longitudinal starter bars located closest to the column ends, as shown in Figure 3.10. As shown in Figure 3.11, the gauges were located in the column and footing and were arranged symmetrically above and below a location at ½-inch above the column-footing interface. The gauges were spaced at intervals of every fourth bar deformation. This arrangement of strain gauges in the anticipated plastic hinge region was intended to enable collection of data that would quantify the extent of strain penetration into the columns and footings. Installation of each strain gauge required removal of one bar deformation. Reinforcement bar deformation removal was limited to the surface area required to adhere a gauge to the bar, which was typically one-half of the circumferential deformation. The exception was full circumferential removal of the bar deformation at a location of ½–inch above the column-footing interface to facilitate the additional installation of a redundant gauge on the opposing side. Strain gauge wires were arranged to exit from the top of the footing.

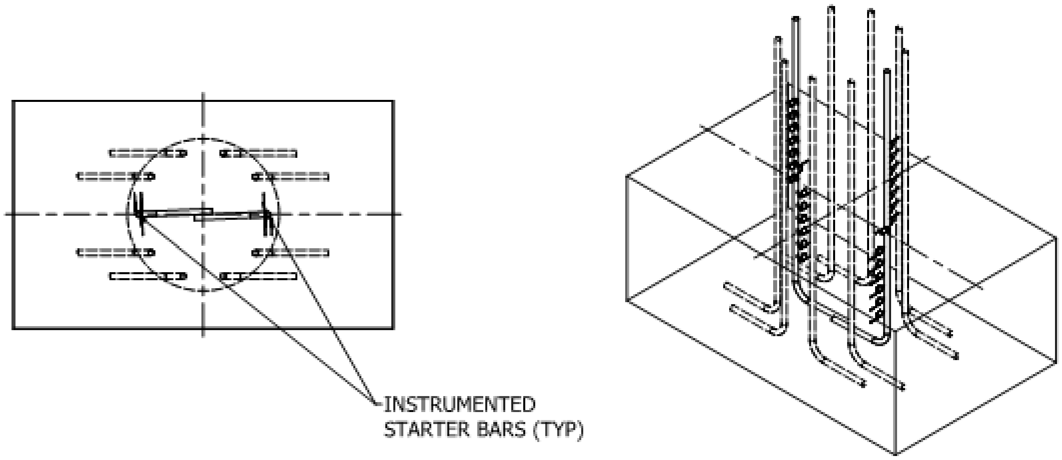

Figure 3.10: Instrumented Starter Bar Layout

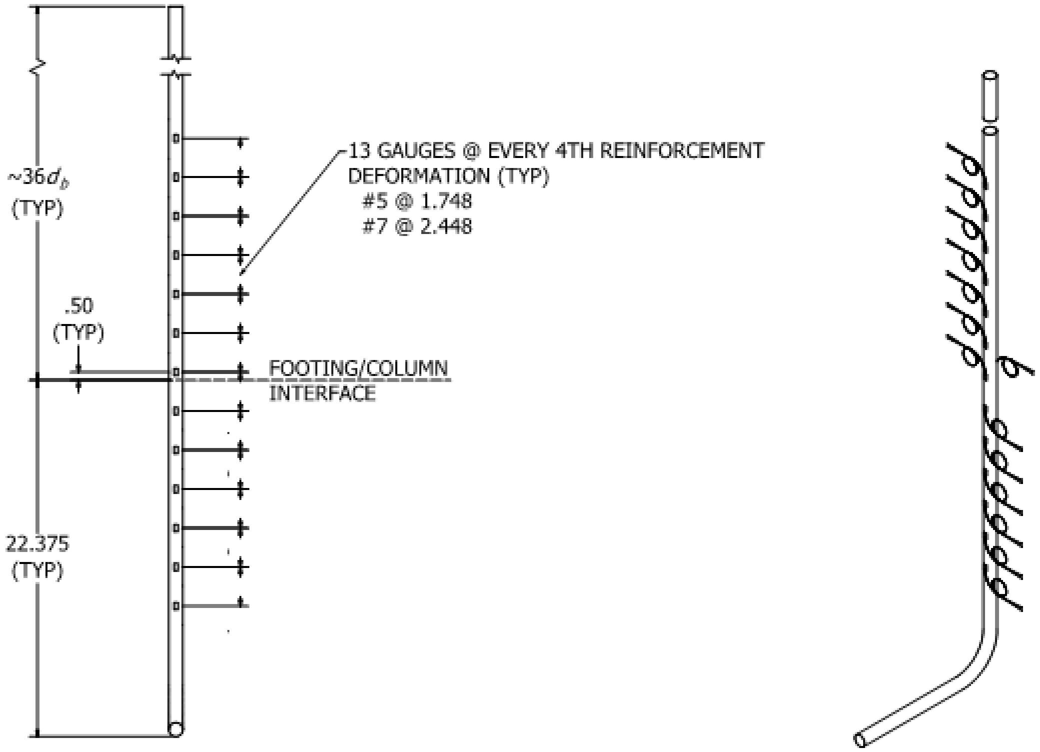

Figure 3.11: Strain Gauge Reinforcement Layout (Dimensions in Inches)

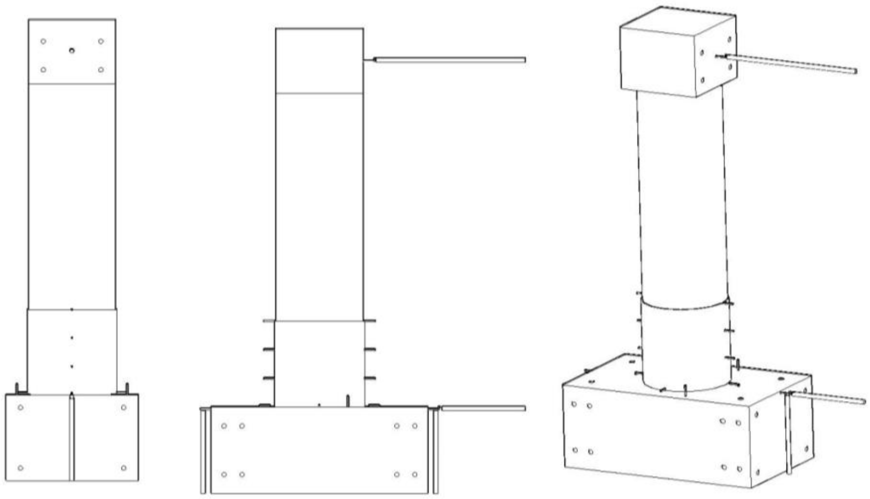

Figure 3.12: Stationary Reference Measurements

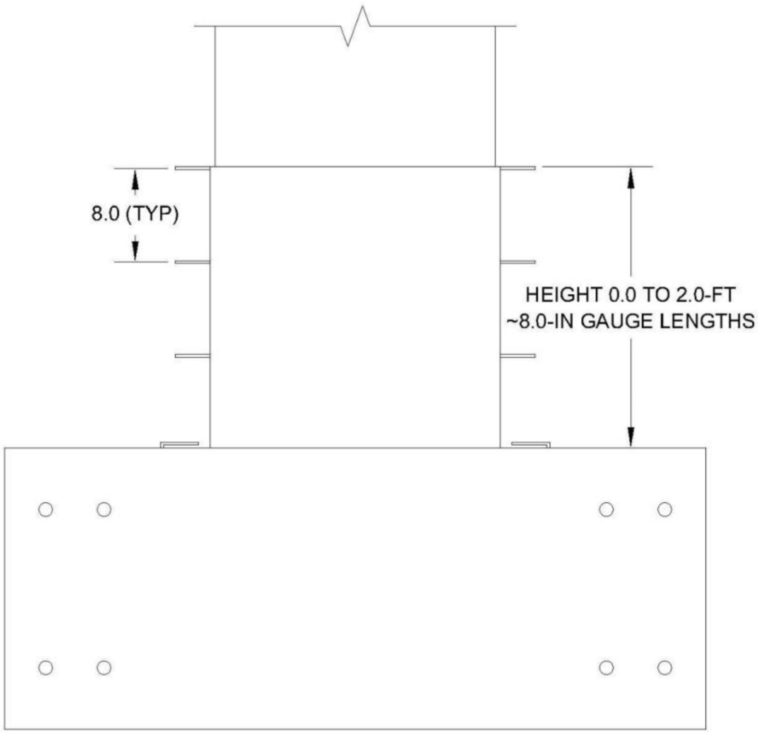

Figure 3.13: LVDT Instrumentation Layout (Dimensions in Inches)

3.1.6. Loading Protocol

A fully-reversed cyclic loading protocol was used for four of the six test columns, and one test was conducted using an earthquake loading protocol. These protocols were identical to those used by McGuiness et al (2021). The reversed-cyclic protocol began with force-controlled cycles, with three cycles each at 5-k, 10-k, and additional intervals of 10-k prior to the yield drift. Displacement control was employed thereafter, with six full cycles each at 1.0, 1.25, 1.5, 1.75, 2.0, and 2.5 times the yield drift, followed by two cycles each at 3.0, 3.5, 4.0, 5.0, 6.0, 8,0, 10.0, 12.5, 15.0, 20.0, and 25.0 times the yield drift, or until the test was completed. For cases in which testing was continued, additional cycles were applied at 25.0 times yield drift, δ_y/H.

C(CFRP)-4.0-#7(1.3)-0.05 used a modification of the reversed cyclic protocol that had twice the number of cycles at each increment. Consistent with the steel jacketed columns tested by McGuiness (2021), the yield drift was taken as 0.4% for C(S)-4.0-#7(1.3)-0.05, C(S)-4.0-#5(1.4)-0.05, and C(S)-4.0-#7(1.3)-0.05-2X and 0.5% for C(S)-4.0-#7(2.7)-0.05 and C(S)-4.0-#7(1.3)-0.15. C(S)-4.0-#7(1.3)-0.05-EQ was tested using an earthquake response history protocol that consisted of a main-shock and aftershock, as shown in Figure 3.36 with values provided in Table 3.6 and 3.7, respectively. For displacement-controlled cycles, the drift used to control the test was corrected to account for footing sliding and rotation.

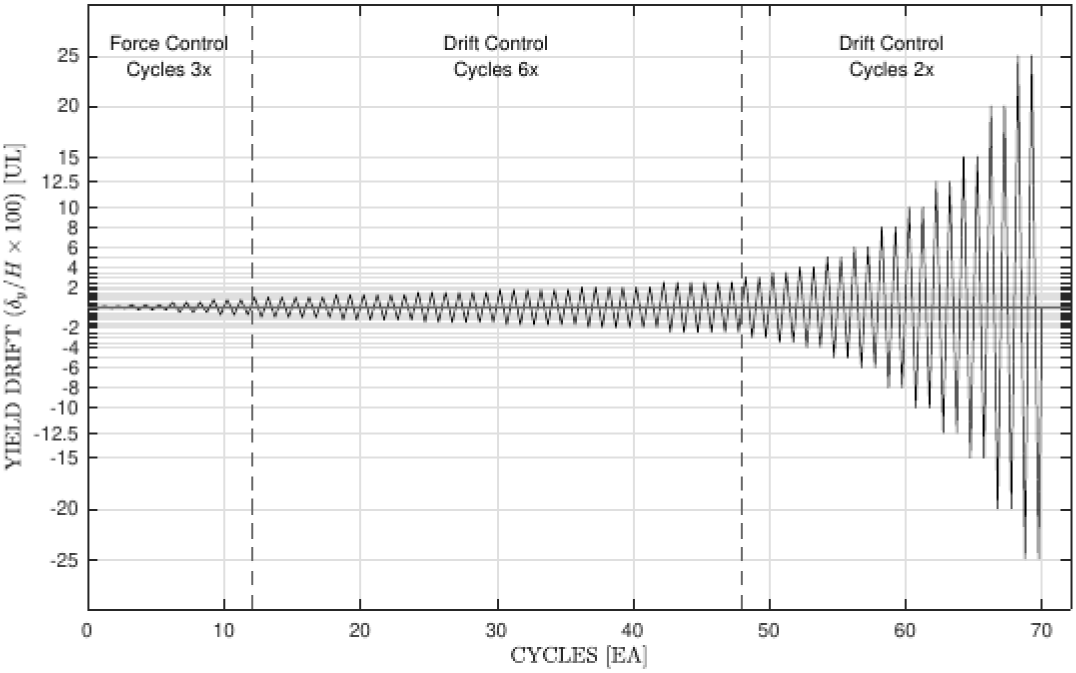

Figure 3.14: Standard Cyclic Loading Protocol

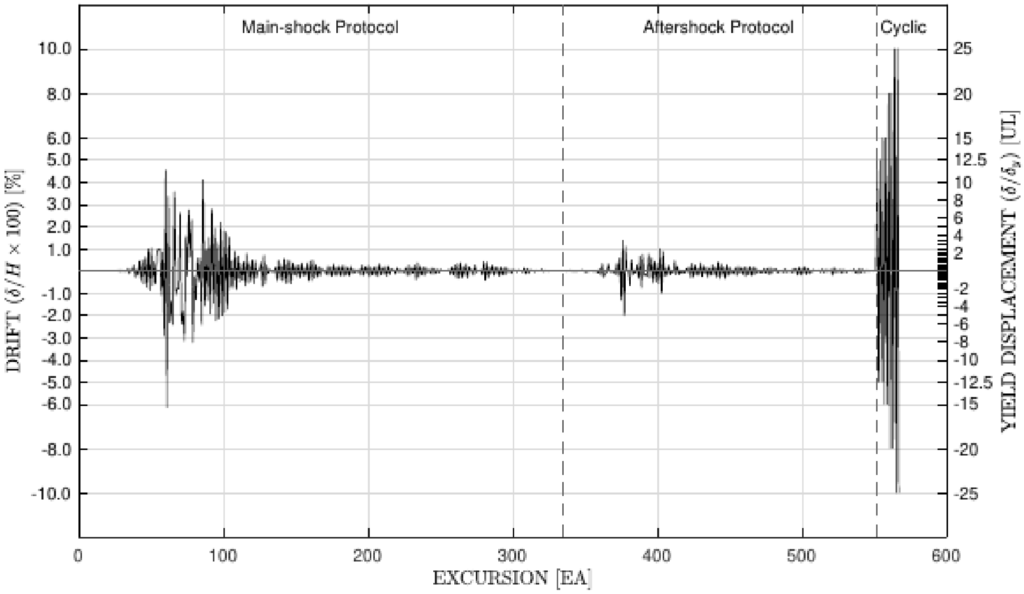

Figure 3.15: Earthquake Loading Protocol

Table 3.6: Main Shock Excursions and Drifts

#	Drift [%]	#	Drift [%]	#	Drift [%]	#	Drift [%]	#	Drift [%]
1	0.000	71	-2.396	141	-0.445	211	-0.167	281	-0.418
2	-0.011	72	-1.836	142	0.545	212	0.212	282	0.395
3	-0.005	73	-3.165	143	-0.550	213	-0.242	283	-0.333
4	-0.006	74	1.565	144	0.502	214	0.208	284	0.181
5	0.016	75	-0.240	145	-0.542	215	-0.165	285	-0.148
6	-0.003	76	2.746	146	0.468	216	0.099	286	0.249
7	-0.001	77	0.611	147	-0.571	217	-0.035	287	-0.212
8	-0.004	78	2.301	148	0.355	218	0.059	288	0.168
9	-0.002	79	-3.229	149	-0.185	219	-0.141	289	-0.146
10	-0.008	80	-0.268	150	0.252	220	0.140	290	0.179
11	0.000	81	-1.303	151	-0.290	221	-0.066	291	-0.247
12	-0.004	82	0.567	152	0.257	222	0.079	292	0.162
13	0.005	83	-0.468	153	-0.325	223	-0.077	293	-0.187
14	-0.002	84	0.569	154	0.350	224	0.035	294	0.165
15	-0.005	85	-2.447	155	-0.257	225	-0.082	295	-0.190
16	0.000	86	4.087	156	0.145	226	0.135	296	0.146
17	0.000	87	-1.566	157	-0.225	227	-0.232	297	-0.068
18	0.004	88	0.957	158	0.353	228	0.259	298	0.042
19	-0.011	89	-1.340	159	-0.452	229	-0.217	299	-0.118

20	-0.005	90	1.496	160	0.455	230	0.141	300	0.080
21	-0.006	91	-1.944	161	-0.442	231	-0.103	301	-0.038
22	0.004	92	2.784	162	0.491	232	0.249	302	0.040
23	0.003	93	-1.460	163	-0.337	233	-0.421	303	-0.060
24	0.004	94	1.911	164	0.276	234	0.376	304	0.044
25	0.004	95	-2.256	165	-0.296	235	-0.304	305	-0.018
26	0.023	96	1.260	166	0.190	236	0.219	306	0.021
27	-0.026	97	-2.155	167	-0.249	237	-0.185	307	-0.077
28	0.044	98	2.183	168	0.139	238	0.174	308	0.140
29	-0.055	99	-2.025	169	-0.033	239	-0.230	309	-0.132
30	0.025	100	1.794	170	0.018	240	0.168	310	0.102
31	-0.021	101	-1.856	171	-0.184	241	-0.082	311	-0.130
32	-0.021	102	1.752	172	0.217	242	0.060	312	0.058
33	-0.039	103	-1.727	173	-0.204	243	-0.127	313	0.008
34	0.119	104	1.510	174	0.187	244	0.136	314	0.011
35	-0.130	105	-0.758	175	-0.256	245	-0.145	315	-0.063
36	0.057	106	0.473	176	0.300	246	0.119	316	0.034
37	-0.004	107	-0.771	177	-0.210	247	-0.127	317	-0.023
38	0.251	108	0.869	178	0.184	248	0.063	318	0.016
39	-0.323	109	-0.852	179	-0.226	249	-0.081	319	-0.016
40	0.073	110	0.672	180	0.213	250	0.071	320	0.072
41	-0.195	111	-0.495	181	-0.221	251	0.000	321	-0.047
42	0.447	112	0.345	182	0.232	252	0.001	322	0.029
43	-0.460	113	-0.433	183	-0.253	253	0.000	323	-0.033
44	0.493	114	0.424	184	0.221	254	0.004	324	0.019
45	-0.593	115	-0.674	185	-0.211	255	-0.023	325	-0.024
46	0.625	116	0.785	186	0.157	256	0.070	326	0.013
47	-0.746	117	-0.541	187	-0.232	257	-0.183	327	-0.018
48	0.980	118	0.384	188	0.216	258	0.170	328	0.008
49	-0.855	119	-0.465	189	-0.132	259	-0.191	329	-0.014
50	1.019	120	0.482	190	0.086	260	0.261	330	0.004
51	-0.659	121	-0.566	191	-0.097	261	-0.340	331	-0.011
52	0.405	122	0.478	192	0.025	262	0.330	332	0.002
53	-0.590	123	-0.340	193	-0.070	263	-0.347	333	-0.009
54	0.930	124	0.021	194	0.087	264	0.373	334	0.000
55	0.924	125	0.011	195	-0.203	265	-0.319		
56	0.987	126	0.395	196	0.254	266	0.206		
57	-1.095	127	-0.708	197	-0.224	267	-0.223		
58	0.841	128	0.714	198	0.192	268	0.310		
59	-2.925	129	-0.590	199	-0.117	269	-0.342		
60	4.524	130	0.245	200	0.236	270	0.175		

61	-6.148	131	-0.117	201	-0.284	271	-0.048		
62	3.341	132	0.066	202	0.159	272	0.076		
63	-2.340	133	-0.045	203	-0.179	273	-0.205		
64	1.358	134	-0.036	204	0.183	274	0.251		
65	-2.432	135	-0.055	205	-0.310	275	-0.080		
66	3.553	136	0.161	206	0.202	276	0.021		
67	-1.108	137	-0.453	207	-0.277	277	-0.031		
68	-0.795	138	0.468	208	0.310	278	0.058		
69	-0.800	139	-0.402	209	-0.181	279	-0.196		
70	2.616	140	0.306	210	0.142	280	0.423		

Table 3.7: After-shock Excursions and Drifts

#	Drift [%]	#	Drift [%]	#	Drift [%]	#	Drift [%]	#	Drift [%]
1	-0.017	46	-0.01	91	-0.3	136	0.029	181	0.062
2	-0.013	47	-0.648	92	0.256	137	-0.092	182	-0.062
3	-0.024	48	0.503	93	-0.207	138	-0.098	183	0.057
4	-0.003	49	-0.161	94	0.129	139	0.114	184	-0.035
5	-0.024	50	-0.077	95	-0.209	140	-0.105	185	0.054
6	0.043	51	-0.079	96	0.364	141	0.111	186	-0.212
7	-0.034	52	0.263	97	-0.272	142	-0.16	187	0.155
8	-0.032	53	-0.351	98	0.231	143	0.149	188	-0.118
9	-0.035	54	0.666	99	-0.144	144	-0.139	189	0.06
10	-0.028	55	-0.77	100	0.17	145	0.063	190	-0.049
11	-0.028	56	0.752	101	-0.311	146	0.05	191	0.06
12	0.007	57	-0.215	102	0.13	147	0.086	192	-0.106
13	0.003	58	-0.147	103	-0.202	148	-0.102	193	0.075
14	0.043	59	-0.271	104	0.271	149	-0.009	194	-0.078
15	-0.031	60	0.773	105	-0.197	150	-0.026	195	0.035
16	-0.028	61	-0.32	106	0.196	151	-0.018	196	-0.078
17	-0.075	62	0.593	107	-0.309	152	-0.075	197	0.004
18	-0.016	63	-0.527	108	0.39	153	0.083	198	-0.006
19	-0.023	64	0.438	109	-0.362	154	-0.093	199	0.03
20	0.002	65	-0.492	110	0.312	155	0.035	200	-0.036
21	-0.021	66	0.34	111	-0.233	156	-0.045	201	0.079
22	-0.02	67	-0.579	112	0.181	157	0.018	202	-0.09
23	-0.021	68	0.982	113	-0.359	158	-0.088	203	0.025
24	-0.02	69	-1.005	114	0.277	159	0.105	204	-0.131
25	-0.092	70	0.855	115	-0.213	160	-0.08	205	0.108
26	0.098	71	-0.26	116	0.18	161	0.11	206	-0.87
27	-0.218	72	0.132	117	-0.154	162	-0.192	207	0.062

28	0.333	73	-0.225	118	0.04	163	0.157	208	0
29	-0.309	74	0.235	119	-0.125	164	-0.196		
30	0.095	75	-0.169	120	0.145	165	0.143		
31	-0.096	76	0.005	121	-0.232	166	-0.146		
32	0.317	77	-0.098	122	0.219	167	0.184		
33	-0.053	78	0.477	123	-0.117	168	-0.159		
34	-0.052	79	-0.169	124	0.142	169	0.11		
35	-0.058	80	0.212	125	-0.155	170	-0.139		
36	-0.057	81	-0.159	126	0.174	171	0.033		
37	-0.157	82	-0.011	127	-0.277	172	-0.078		
38	0.369	83	-0.117	128	0.161	173	0.061		
39	-0.225	84	0.001	129	-0.175	174	-0.013		
40	0.566	85	-0.1	130	0.194	175	0.02		
41	-1.321	86	0.105	131	-0.223	176	0.001		
42	1.37	87	-0.069	132	0.182	177	0.028		
43	-2.02	88	0.198	133	-0.191	178	-0.074		
44	1.103	89	-0.328	134	0.151	179	0.071		
45	-0.017	90	0.326	135	-0.107	180	-0.085		

3.2. Results and Discussion

3.2.1. Observed Damage

3.2.1.1 Concrete Damage

Photos that show damage at 4 δ/δ_y, 8 δ/δ_y, 15 δ/δ_y, 20 δ/δ_y, and the completion of testing are provided in Figure 3.16 and Figure 3.17, Figure 3.18 and Figure 3.19, Figure 3.20 and Figure 3.21, Figure 3.22 and Figure 3.23, and Figure 3.24 and Figure 3.25, respectively. Concrete crushing was not observed within the jacketed region, indicating that the jackets adequately confined the concrete. Damage generally concentrated at the top of the footing in the vicinity of the column, with spalling observed in the footing. Cracking was observed above the jacket. Strength degradation was associated with fracture of longitudinal reinforcement, which is described in more detail in Section 3.2.1.2, as spalling of concrete and longitudinal reinforcement buckling were not observed above the jacket. The exception was C(CFRP)-4.0-#7(1.3)-0.15, in which significant concrete damage and longitudinal reinforcement buckling, characteristic of a plastic hinge, occurred above the jacket. Spalling of concrete was first observed at the first cycle to 12.5(δ/δ_y) in the negative direction, with longitudinal bars visible at 15δ/δ_y (Figure 3.21.f). Spalling of concrete and buckling of longitudinal reinforcement occurred, as shown in Figure 3.24.f and Figure 3.25.f, until a state of axial failure was reached during the final cycle to 15(δ/δ_y). Extending the jacket further up the height of the column would likely have prevented this damage.

The cycles at which footing cracks, horizontal flexural cracks, vertical shear cracks, and spalling of footing concrete were first observed are provided in Table 3.8. Damage in all tests included splitting cracks on the top surface of the footing that would propagate down the long sides and horizontal cracks on the tension face of the column just above the jacket. The horizontal cracks closed when the load was reversed and would propagate as the test progressed. In cycles after 8δ/δ_y, horizontal cracks extended up to 64-inches from the column base. The extent of flexural cracks varied significantly between tests in both severity and how far they propagated up the column. Flexural cracks began to develop between 30-kip and 3.5 δ/δ_y for all columns. C(CFRP)-4.0-#7(1.3)-0.15 is the only column in which flexural cracks developed prior to footing cracks. The flexural cracks progressed faster in terms of quantity, length, and severity for C(CFRP)-4.0-#7(1.3)-0.15 with a measured 0.068 inch wide crack at the first cycle to 8δ/δ_y in the negative direction (Figure 3.19.f). The flexural cracks continued to grow as the test progressed, with vertical cracks connecting the horizontal flexural cracks being noticed at the first cycle to 12.5 δ/δ_y.

Diagonal cracks near mid-depth of the column, which were characterized as shear cracks, were observed for C(CFRP)-4.0-#5(1.4)-0.05, C(CFRP)-4.0-#7(2.7)-0.05, C(CFRP)-4.0-#7(1.3)-0.05-2X, and C(CFRP)-4.0-#7(1.3)-0.15. For C(CFRP)-4.0-#7(1.3)-0.05-2X, a shear crack was first observed at 12.5 δ/δ_y, while shear cracks were not observed for C(CFRP)-4.0-#7(1.3)-0.05 and C(CFRP)-4.0-#7(1.3)-0.05-EQ, which differed from C(CFRP)-4.0-#7(1.3)-0.05-2X only in loading protocol.

Significant torsion was observed for C(CFRP)-4.0-#7(1.3)-0.05-EQ, and test was stopped before reaching the third cycle at 10% drift, as the base of the column had ratcheted roughly 1.5 inches out of plane. The Final photos of the column shown in figure 3.9.d, show that the column scraped off the cover of the footing all the way down to the upper reinforcement as it moved out of plane.

Table 3.8: Concrete Damage Onset

Column ID	Footing Cracks	Flexure Cracks	Shear Cracks	Footing Spalling
C(CFRP)-4.0-#7(1.3)-0.05	5-k (2nd)	$2(\delta/\delta_y)$ (1st)	N/A	$15(\delta/\delta_y)$ (1st)
C(CFRP)-4.0-#5(1.4)-0.05	$1(\delta/\delta_y)$ (1st)	$1.25(\delta/\delta_y)$ (1st)	$4(\delta/\delta_y)$ (1st)	$15(\delta/\delta_y)$ (1st)
C(CFRP)-4.0-#7(2.7)-0.05	$1.75(\delta/\delta_y)$ (2nd)	$3.5(\delta/\delta_y)$ (2nd)	$5(\delta/\delta_y)$ (1st)	$10(\delta/\delta_y)$ (1st)
C(CFRP)-4.0-#7(1.3)-0.05-EQ	Start of test	$1.12(\delta/\delta_y)$ (1st)	N/A	$12.5(\delta/\delta_y)$ (1st)
C(CFRP)-4.0-#7(1.3)-0.05-2X	Start of test	30-k (1st)	$12.5(\delta/\delta_y)$ (1st)	$10(\delta/\delta_y)$ (1st)
C(CFRP)-4.0-#7(1.3)-0.15	$1.25(\delta/\delta_y)$	40-k (1st)	$8(\delta/\delta_y)$ (2nd)	$10(\delta/\delta_y)$ (1st)

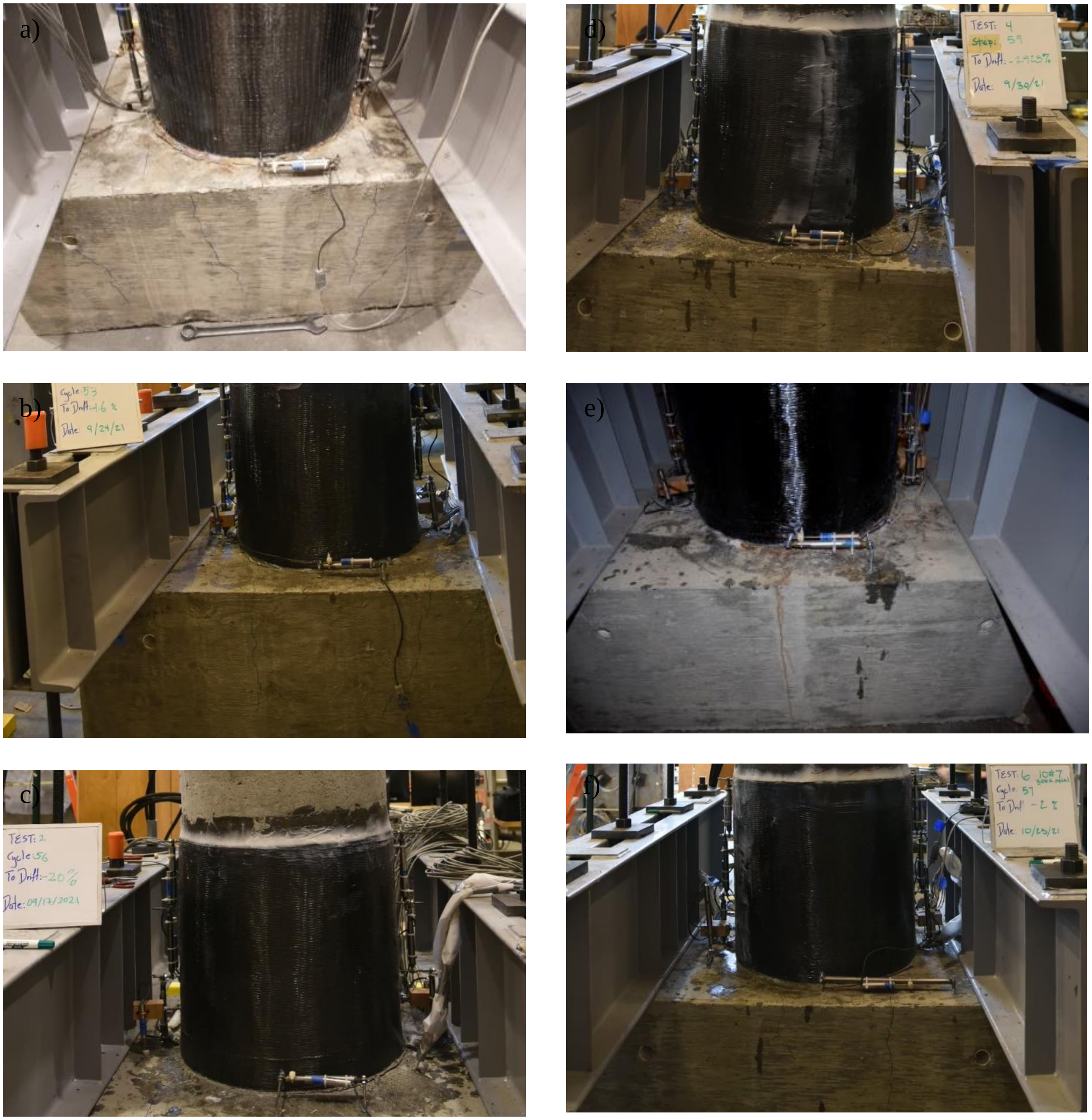

Figure 3.16. Concrete Damage at Base at $\boldsymbol{4.0\delta/\delta_y}$ (2.55$\boldsymbol{\delta/\delta_y}$ for C(CFRP)-4.0-#7(1.3)-0.05-EQ) for: a) C(CFRP)-4.0-#7(1.3)-0.05, b) C(CFRP)-4.0-#5(1.4)-0.05, c) C(CFRP)-4.0-#7(2.7)-0.05, d) C(CFRP)-4.0-#7(1.3)-0.05-EQ, e) C(CFRP)-4.0-#7(1.3)-0.05-2X, and f) C(CFRP)-4.0-#7(1.3)-0.15

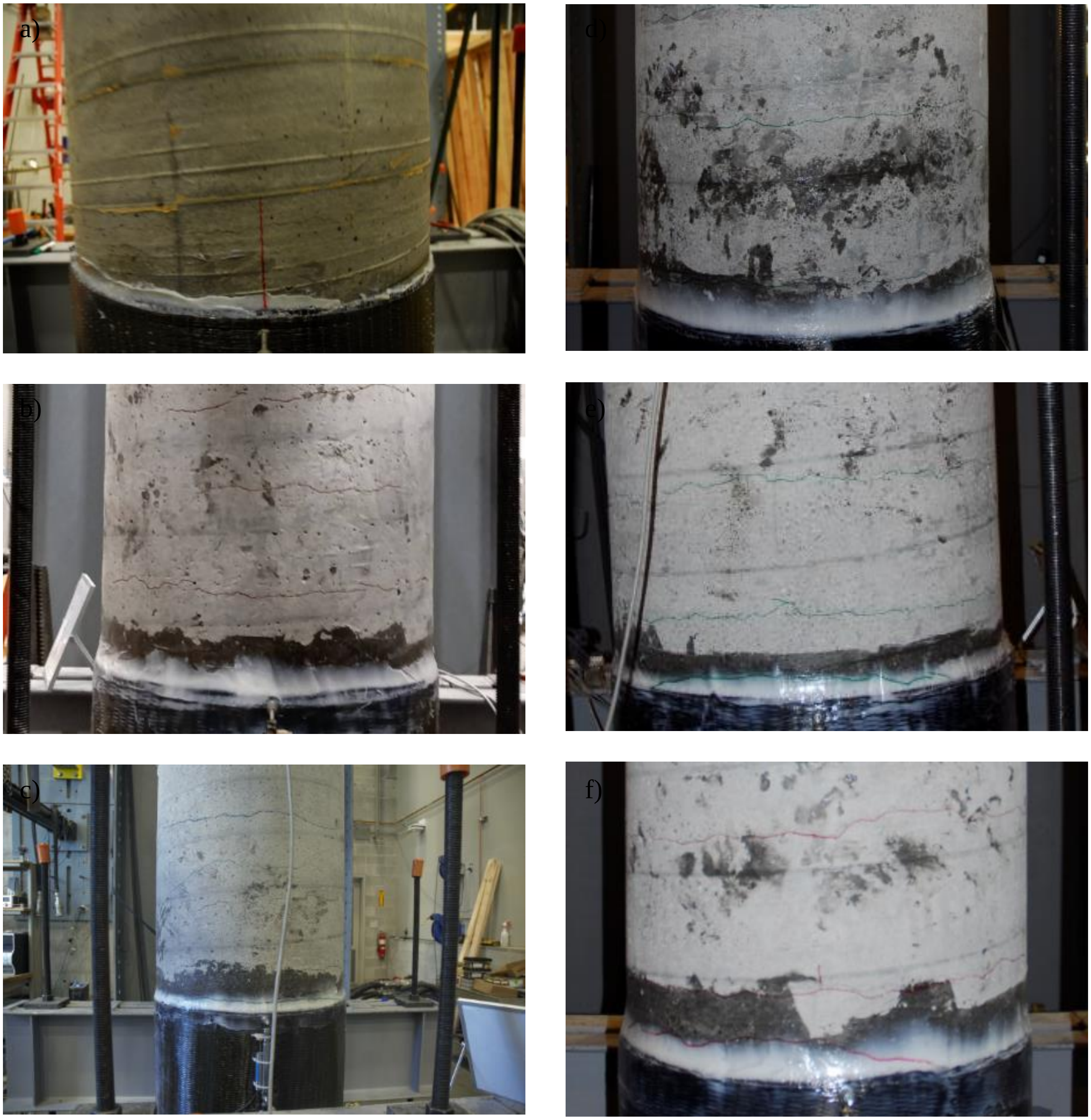

Figure 3.17. Concrete Damage Above Jacket at $\boldsymbol{4.0\delta/\delta_y}$ (2.55$\boldsymbol{\delta/\delta_y}$ for C(CFRP)-4.0-#7(1.3)-0.05-EQ) for: a) C(CFRP)-4.0-#7(1.3)-0.05, b) C(CFRP)-4.0-#5(1.4)-0.05, c) C(CFRP)-4.0-#7(2.7)-0.05, d) C(CFRP)-4.0-#7(1.3)-0.05-EQ, e) C(CFRP)-4.0-#7(1.3)-0.05-2X, and f) C(CFRP)-4.0-#7(1.3)-0.15

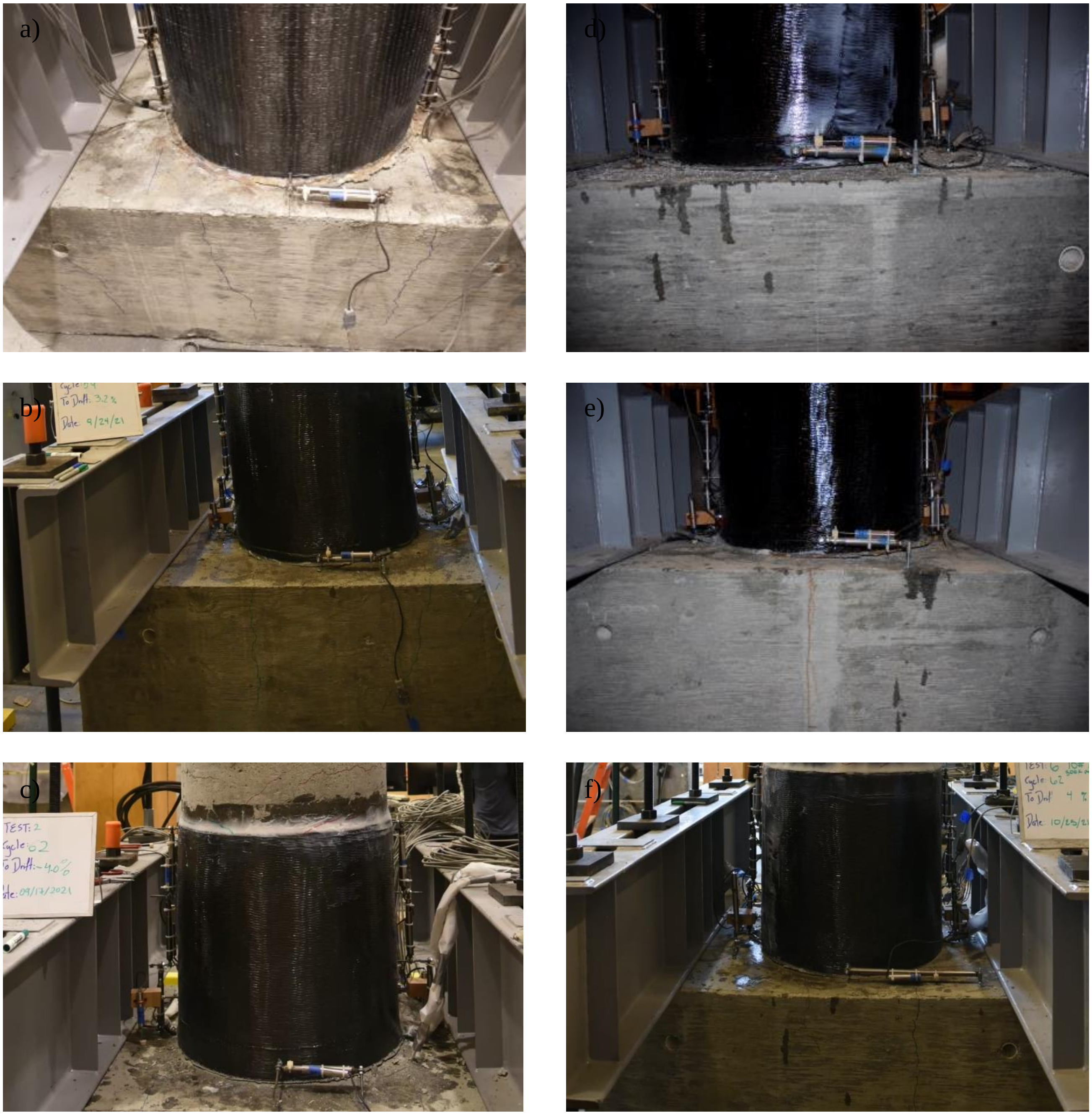

Figure 3.18. Concrete Damage at Base at $\boldsymbol{8.0\delta/\delta_y}$ (7.3$\boldsymbol{\delta/\delta_y}$ for C(CFRP)-4.0-#7(1.3)-0.05-EQ) for: a) C(CFRP)-4.0-#7(1.3)-0.05, b) C(CFRP)-4.0-#5(1.4)-0.05, c) C(CFRP)-4.0-#7(2.7)-0.05, d) C(CFRP)-4.0-#7(1.3)-0.05-EQ, e) C(CFRP)-4.0-#7(1.3)-0.05-2X, and f) C(CFRP)-4.0-#7(1.3)-0.15

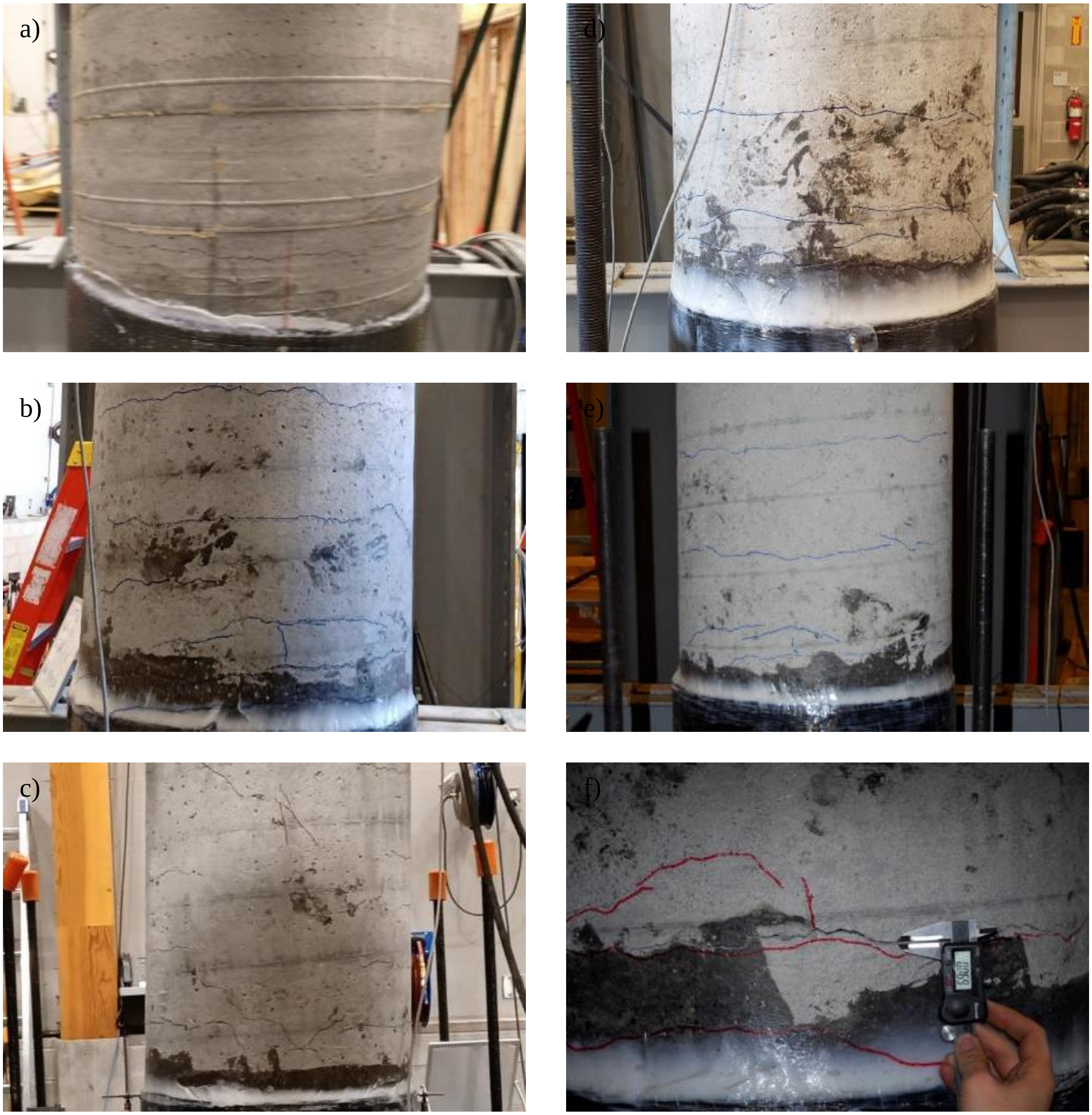

Figure 3.19. Concrete Damage Above Jacket at $\mathbf{8.0}\boldsymbol{\delta/\delta_y}$ (7.3$\boldsymbol{\delta/\delta_y}$ for C(CFRP)-4.0-#7(1.3)-0.05-EQ) for: a) C(CFRP)-4.0-#7(1.3)-0.05, b) C(CFRP)-4.0-#5(1.4)-0.05, c) C(CFRP)-4.0-#7(2.7)-0.05, d) C(CFRP)-4.0-#7(1.3)-0.05-EQ, e) C(CFRP)-4.0-#7(1.3)-0.05-2X, and f) C(CFRP)-4.0-#7(1.3)-0.15

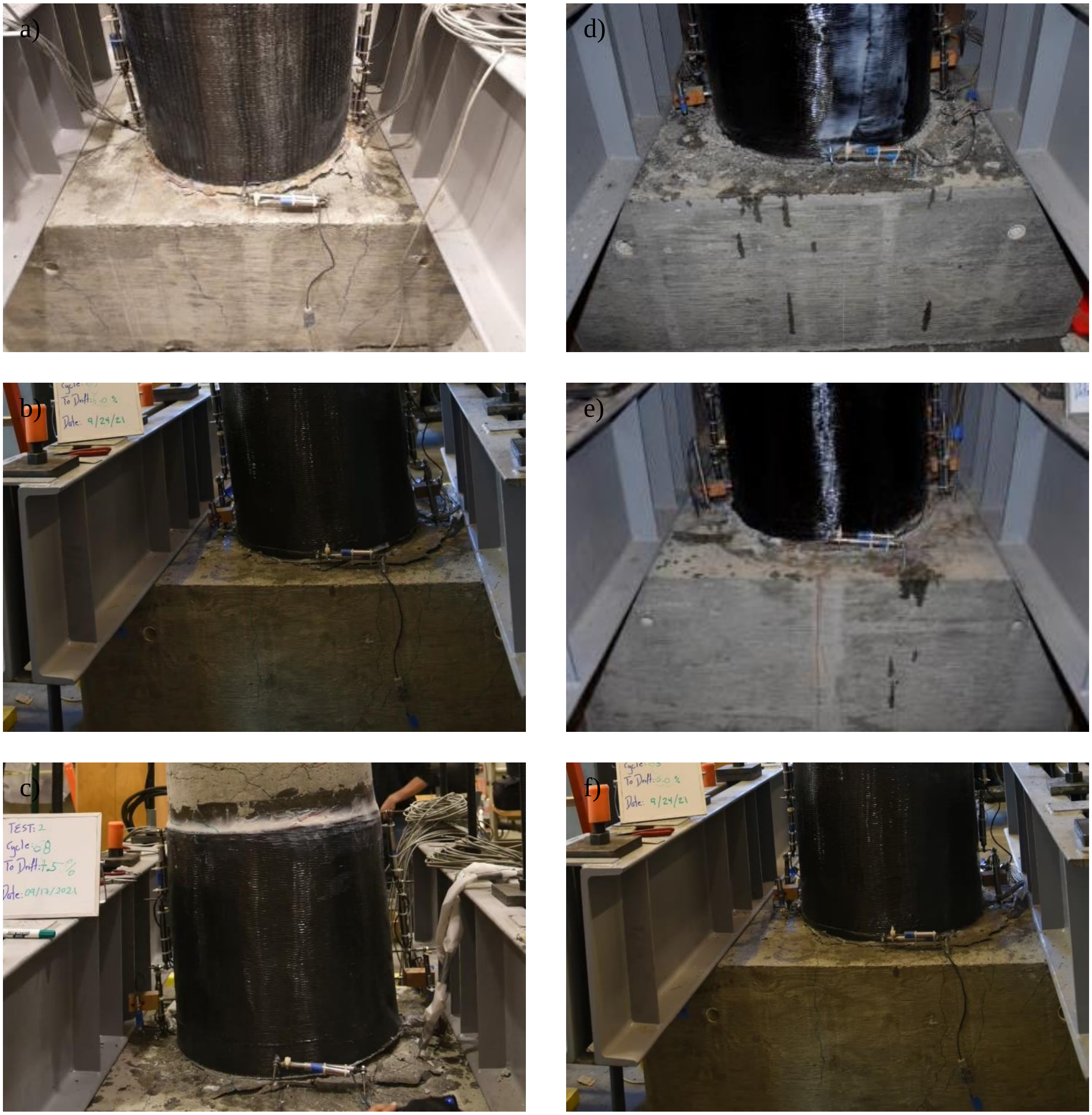

Figure 3.20. Concrete Damage at Base at $15\delta/\delta_y$ for: a) C(CFRP)-4.0-#7(1.3)-0.05, b) C(CFRP)-4.0-#5(1.4)-0.05, c) C(CFRP)-4.0-#7(2.7)-0.05, d) C(CFRP)-4.0-#7(1.3)-0.05-EQ, e) C(CFRP)-4.0-#7(1.3)-0.05-2X, and f) C(CFRP)-4.0-#7(1.3)-0.15

Figure 3.21. Concrete Damage Above Jacket at 15$\boldsymbol{\delta/\delta_y}$ for: a) C(CFRP)-4.0-#7(1.3)-0.05, b) C(CFRP)-4.0-#5(1.4)-0.05, c) C(CFRP)-4.0-#7(2.7)-0.05, d) C(CFRP)-4.0-#7(1.3)-0.05-EQ, e) C(CFRP)-4.0-#7(1.3)-0.05-2X, and f) C(CFRP)-4.0-#7(1.3)-0.15

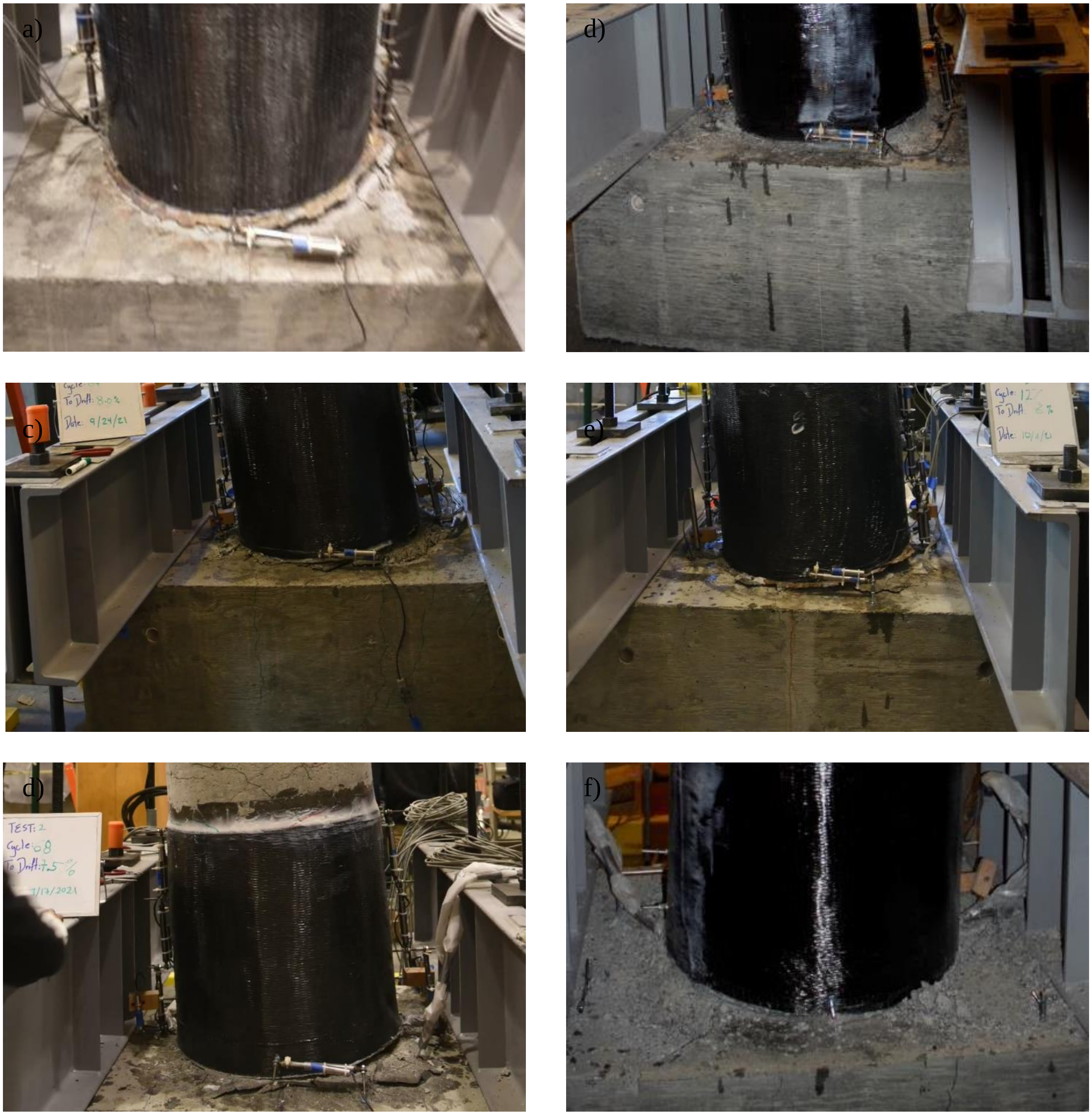

Figure 3.22. Concrete Damage at Base at 20$\boldsymbol{\delta/\delta_y}$ (at $\mathbf{15}\boldsymbol{\delta/\delta_y}$ for C(CFRP)-4.0-#7(1.3)-0.15) for: a) C(CFRP)-4.0-#7(1.3)-0.05, b) C(CFRP)-4.0-#5(1.4)-0.05, c) C(CFRP)-4.0-#7(2.7)-0.05, d) C(CFRP)-4.0-#7(1.3)-0.05-EQ, e) C(CFRP)-4.0-#7(1.3)-0.05-2X, and f) C(CFRP)-4.0-#7(1.3)-0.15

Figure 3.23. Concrete Damage Above Jacket at 20$\boldsymbol{\delta}/\boldsymbol{\delta_y}$ (at $\mathbf{15}\boldsymbol{\delta}/\boldsymbol{\delta_y}$ for C(CFRP)-4.0-#7(1.3)-0.15) for: a) C(CFRP)-4.0-#7(1.3)-0.05, b) C(CFRP)-4.0-#5(1.4)-0.05, c) C(CFRP)-4.0-#7(2.7)-0.05, d) C(CFRP)-4.0-#7(1.3)-0.05-EQ, e) C(CFRP)-4.0-#7(1.3)-0.05-2X, and f) C(CFRP)-4.0-#7(1.3)-0.15

Figure 3.24. Concrete Damage at Base at Completion of Testing for: a) C(CFRP)-4.0-#7(1.3)-0.05, b) C(CFRP)-4.0-#5(1.4)-0.05, c) C(CFRP)-4.0-#7(2.7)-0.05, d) C(CFRP)-4.0-#7(1.3)-0.05-EQ, e) C(CFRP)-4.0-#7(1.3)-0.05-2X, and f) C(CFRP)-4.0-#7(1.3)-0.15

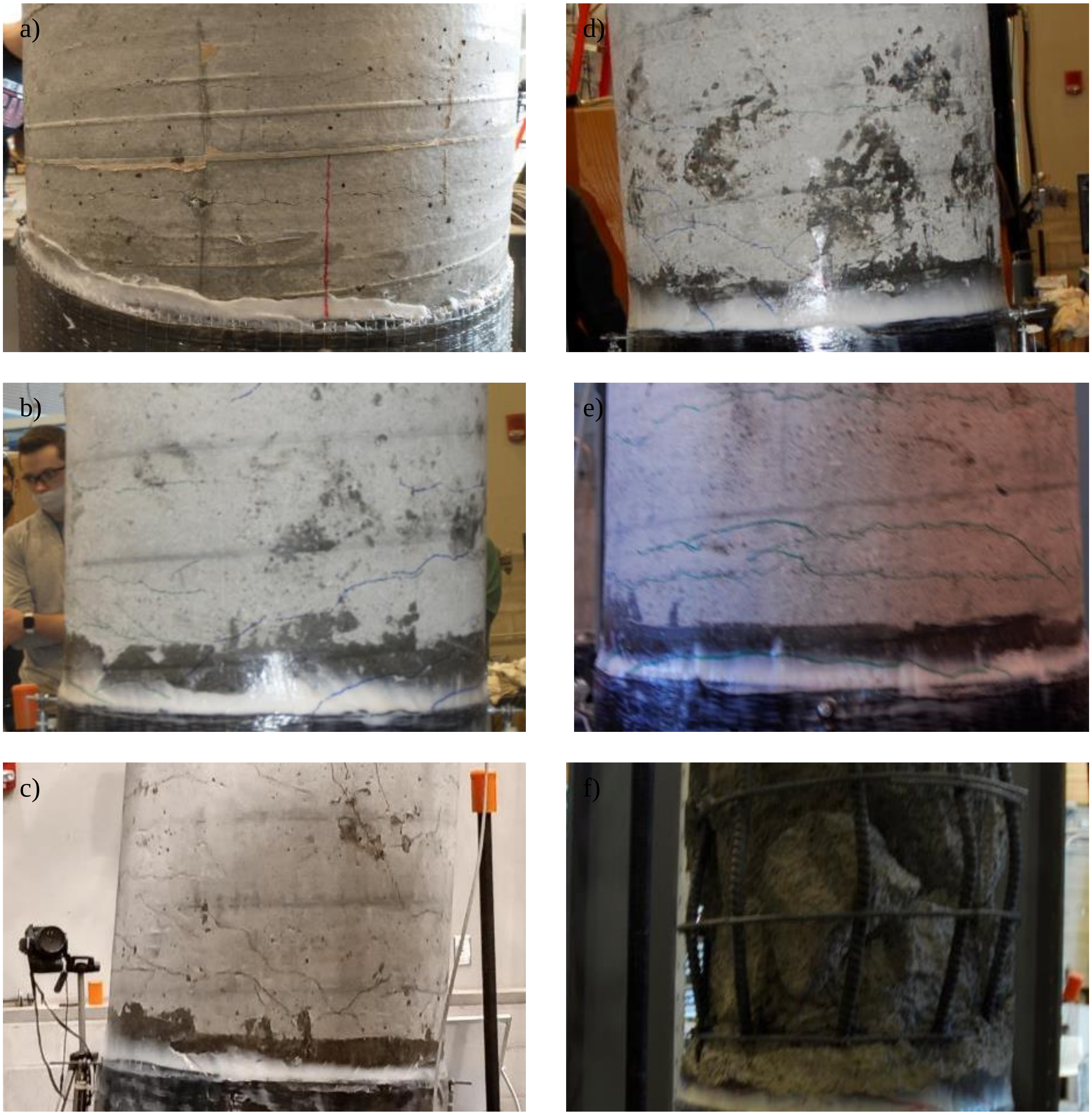

Figure 3.25. Concrete Damage Above Jacket at Completion of Testing for: a) C(CFRP)-4.0-#7(1.3)-0.05, b) C(CFRP)-4.0-#5(1.4)-0.05, c) C(CFRP)-4.0-#7(2.7)-0.05, d) C(CFRP)-4.0-#7(1.3)-0.05-EQ, e) C(CFRP)-4.0-#7(1.3)-0.05-2X, and f) C(CFRP)-4.0-#7(1.3)-0.15

3.2.1.2 Fatigue Fracture of Longitudinal Reinforcement

In all cases, low-cycle fatigue fracture of longitudinal reinforcement occurred near the footing-column interface. Concrete cracks that formed at the footing-column interface, as shown in Figure 3.16, were attributed to longitudinal reinforcement bond slip. The sequence of reinforcement fractures in each loading direction is provided in Table 3.9 and Table 3.10. For each of the five tests with fully reversed-cyclic loading, a level of variability is evident in Table 3.9. For C(CFRP)-#7(1.4)-0.05-EQ, the first positive and negative fractures occurred at the same cycle, despite higher demands in the negative direction during the earthquake and aftershock protocols. In the columns containing more than one bar fracture, the second fracture occurred in the same or immediately succeeding excursion. Due to torsional ratcheting at the base, shown in Figure 3.24.d, testing of C(CFRP)-4.0-#7(1.3)-0.05-EQ was stopped before more than six bars had fractured. Only one bar fractured for C(CFRP)-4.0-#7(1.3)-0.15 due to plastic hinging above the CFRP jacket, as shown in Figure 3.25.f.

Table 3.9: Sequence of Longitudinal Bar Fractures

Bar Fracture	Column Name					
	C(CFRP)-4.0- #7(1.3)-0.05	C(CFRP)-4.0-#5(1.4)-0.05	C(CFRP)-4.0-#7(2.7)-0.05	C(CFRP)-4.0-#7(1.3)-0.05-EQ	C(CFRP)-4.0-#7(1.3)-0.05-2X	C(CFRP)-4.0-#7(1.3)-0.15
1st Pos. (+)	@ 4.26% 1st to +8.0%	@ 5.22% 1st to +8.0%	@ 6.39% 2nd to +7.5%	@ 4.75% 1st to +10.0%	@ -1.62% 2nd to +6.0%	–
1st Neg. (–)	@ -5.28% 2nd to -6.0%	@ -5.02% 2nd to -6.0%	@ -4.20% 2nd to -7.5%	@ -4.74% 1st to -10.0%	@ -0.22% 1st to -6.0%	@ -0.26% 1st to -7.5%
2nd Pos. (+)	@ 2.10% 2nd to +8.0%	@ 5.92 % 1st to +8.0%	@ 0.83% 1st to +10.0%	@ 7.06% 1st to +10.0%	@ 5.80% 1st to +8.0%	–
2nd Neg. (–)	@ -2.18% 2nd to -8.0%	@ -5.77% 2nd to -6.0%	@ -6.08% 2nd to -7.5%	@ -6.82% 1st to -10.0%	@ 0.24% 3rd to -6.0%	–
3rd Pos. (+)	@ 7.39% 1st to +10.0%	@ 3.00% 2nd to +8.0%	@ 6.42% 1st to +10.0%	@ 1.10 2nd to +10.0%	@ 4.61% 2nd to +8.0%	–
3rd Neg. (–)	@ -4.38% 2nd to -8.0%	@ -3.63% 1st to -8.0%	@ 0.80% 1st to -10.0%	@ -9.09% 1st to -10.0%	@ -3.83% 3rd to -6.0%	–
4th Pos. (+)	@ 2.61% 3rd to +10.0%	@ 3.73% 2nd to +8.0%	@ 7.97% 1st to +10.0%	–	–	–
4th Neg. (–)	@ -9.14 4th to -10.0%	@ -4.30% 1st to -8.0%	@ -6.62% 1st to -10.0%	–	@ -7.08% 4th to -8.0%	–
5th Pos. (+)	@ 8.88% 4th to +10.0%	@ 6.70 % 2nd to +8.0%	@ 8.40% 1st to +10.0%	–	–	–
5th Neg. (–)	–	@ -4.49% 2nd to -8.0%	@ -5.51% 2nd to -10.0%	–	@ -9.72% 2nd to -10.0%	–

6th Pos. (+)	N.A.	@ 7.38% 2nd to +8.0%	@ 6.46% 2nd to +10.0%	N.A.	N.A.	N.A.
6th Neg. (–)	N.A.	@ -7.25% 2nd to -8.0%	@ -7.83 2nd to -10.0%	N.A.	N.A.	N.A.
7th Pos. (+)	N.A.	@ 7.11% 1st to +10.0%	@ 9.89% 2nd to +10.0%	N.A.	N.A.	N.A.
7th Neg. (–)	N.A.	@ -7.68% 2nd to -8.0%	@ -7.85% 6th to -10.0%	N.A.	N.A.	N.A.
8th Pos. (+)	N.A.	@ 9.34% 3rd to +10.0%	@ 0.15% 4th to +10.0%	N.A.	N.A.	N.A.
8th Neg. (–)	N.A.	@ -9.59% 2nd to -10.0%	@ -9.25% 7th to -10.0%	N.A.	N.A.	N.A.
9th Pos. (+)	N.A.	@ 6.46% 4th to +10.0%	@ 8.23% 4th to +10.0%	N.A.	N.A.	N.A.
9th Neg. (–)	N.A.	@ -8.03% 3rd to -10.0%	–	N.A.	N.A.	N.A.
10th Pos. (+)	N.A.	@ 9.01% 4th to +10.0%	@ -5.89% 5th to +10.0%	N.A.	N.A.	N.A.
10th Neg. (–)	N.A.	–	–	N.A.	N.A.	N.A.

Table 3.10: Summary of Cycles at which Longitudinal Bars Fractured

Cycle at Bar Fracture		Column Name				
$\frac{\delta}{\delta_y}$ (Cycle Number)	Drift	C(CFRP)-#7(1.3)-0.05	C(CFRP)-4.0-#5(1.4)-0.05	C(CFRP)-4.0-#7(2.7)-0.05	C(CFRP)-4.0-#7(1.3)-0.05-2X	C(CFRP)-4.0-#7(1.3)-0.15
15 (1)-	6.0%*, 7.5%†				1	1
15 (2)+	7.5%†			1	2	
15 (2)-	6.0%*, 7.5%†	1	1, 2	2, 3		
15 (3)-	6.0%‡				3, 4	
20 (1)+	8.0%*, 10.0%†	2	3, 4	4, 5, 6, 7	5	
20 (1)-	8.0%*, 10.0%†		5, 6	8, 9		
20 (2)+	8.0%*, 10.0%†	3	7, 8, 9, 10	10, 11	6	
20 (2)-	8.0%*, 10.0%†	4, 5	11, 12, 13	12, 13		
20 (4)+	10.0%†			14, 15		
20 (4)-	8.0%*				7	
20 (5)+	10.0%†			16		
20 (6)-	10.0%†			17		
20 (7)-	10.0%†			18		
25 (1)+	10.0%*	6	14			
25 (2)-	10.0%*		15		8	
25 (3)+	10.0%*	7	16			
25 (3)-	10.0%*		17, 18			
25 (4)+	10.0%*	8	19			
25 (4)-	10.0%*	9				

* for C(CFRP)-4.0- #7(1.3)-0.05, C(CFRP)-4.0-#5(1.4)-0.05, and C(CFRP)-4.0-#7(1.3)-0.05-2X

† for C(CFRP)-4.0-#7(2.7)-0.05 and C(CFRP)-4.0-#7(1.3)-0.15

‡ 3rd and 4th cycles of 15 $\delta/\boldsymbol{\delta_y}$ only completed in the extended loading protocol of C(CFRP)-4.0-#7(1.3)-0.05-2X

3.2.2. Load-Deformation

The lateral load-deformation response is provided in Figure 3.26 for all tests. All columns were flexure-yielding. In general, minimal pinching is evident in the hysteretic responses, indicative of favorable energy dissipation. The level of pinching for C(CFRP)-4.0-#7(1.3)-0.15, which incurred damage above the jacketed region, was greater than the other tests. The sequence of longitudinal bar fractures is indicated on the plots, and the degradation in lateral load resistance occurred primarily due to bar fractures. P-delta demands also reduced lateral load resistance, with quantification of P-delta effects provided in Section 3.3. The values for peak shear demand, V_{max}, normalized peak base moment, M_{max}/M_n, displacement at peak demand, δ_{max}, and drift at peak demand, $\left(\frac{\delta}{H}\right)_{max}$, are provided in Table 3.11 for each test column in both the positive and negative loading direction. M_{max} is defined as:

$$M_{max} = V_{max}H + P\Delta \tag{3-1}$$

where H is the height of the column, P is the axial load, Δ is the column lateral displacement measured at the point of lateral load application, and V_{max} is the maximum shear. As shown in Table 3.11, M_{max}/M_n ranged from 1.244 to 1.435 for the six columns and ranged from 1.279 to 1.345 for the four tests with identical loading protocol. M_{max}/M_n was smallest for C(CFRP)-4.0-#7(1.3)-0.05-2X, suggesting that the increased number of cycles led to a reduction in strength. M_{max}/M_n was highest for C(CFRP)-4.0-#7(1.3)-0.05-EQ, likely due to a large cycle earlier in the cycle sequence than that of the fully reversed cyclic tests. For all tests M_{max}/M_n was within 4% for both the positive and negative loading directions.

Lateral failure was defined to have occurred when the lateral load at a maximum cycle peak first dropped below 20% of the peak lateral load and did not return to this level during subsequent cycles. A maximum cycle peak is defined as a cycle peak that had lateral displacement greater than or equal to any previous peak in that loading direction. The maximum cycle peak prior to the cycle at which lateral failure occurred in the positive and negative loading direction is provided in Table 3.12 for each column. All columns reached lateral failure between 12.5 δ/δ_y and 20.0δ/δ_y. C(CFRP)-4.0-#7(1.3)-0.05-EQ had the greatest displacement before lateral failure occurred in either loading direction. C(CFRP)-4.0-#7(1.3)-0.05 reached the same level of displacement before lateral failure as C(CFRP)-4.0-#7(1.3)-0.05-EQ in the positive direction but not the negative direction. C(CFRP)-4.0-#7(1.3)-0.05-EQ and C(CFRP)-4.0-#7(1.3)-0.05-2X had the greatest difference between the positive and negative loading directions. Both columns had increased strength in the negative loading direction with a 3.7% of M_n increase for C(CFRP)-4.0-#7(1.3)-0.05-EQ and a 3.4% of M_n increase for C(CFRP)-4.0-#7(1.3)-0.05-2X. The discrepancies between the positive and negative cycles of C(CFRP)-4.0-#7(1.3)-0.05-EQ may be attributed to asymmetry in the loading cycles of the earthquake protocol. Of the other four tests, none had greater than a 1% difference in peak moment between the corresponding positive and negative loading directions.

The first bar fracture occurred during the excursion at which lateral failure occurred, with the exception of C(CFRP)-4.0-#7(1.3)-0.15, in which the first bar fractured after lateral failure occurred and the loss in strength was attributed to the concrete damage described in Section 3.2.1.1. The majority of longitudinal reinforcement fractures occurred during the portion of the cyclic excursion beyond zero lateral displacement. While some fractures were reported during unloading, they were in the minority, occurring twice for C(CFRP)-4.0-#7(1.3)-0.05-2X and once for C(CFRP)-4.0-#7(2.7)-0.05. Fractures occurring on the loading excursions typically were associated with an immediate loss of strength. Fractures occurring on the unloading excursions led to a reduction in the rate of loading increase.

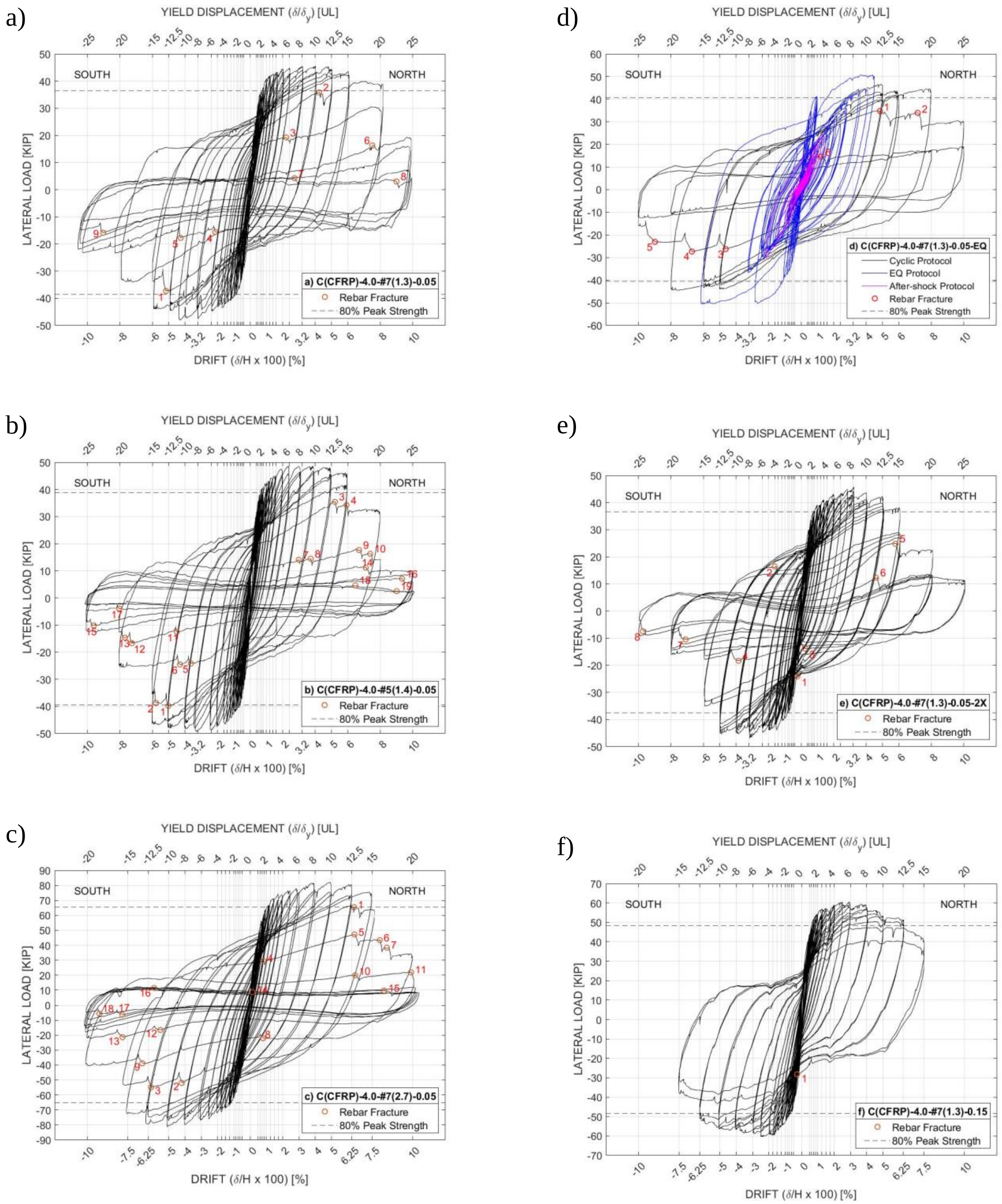

Figure 3.26. Lateral Load Deformation: a) C(CFRP)-4.0-#7(1.3)-0.05, b) C(CFRP)-4.0-#5(1.4)-0.05, c) C(CFRP)-4.0-#7(2.7)-0.05, d) C(CFRP)-4.0-#7(1.3)-0.05-EQ, e) C(CFRP)-4.0-#7(1.3)-0.05-2X, f) C(CFRP)-4.0-#7(1.3)-0.15

Table 3.11: Peak Demands, Displacements, and Drifts

Load	Parameter	C(CFRP) -4.0- #7(1.3)- 0.05	C(CFRP) -4.0- #5(1.4)- 0.05	C(CFRP) -4.0- #7(2.7)- 0.05	C(CFRP) -4.0- #7(1.3)- 0.05-EQ	C(CFRP) -4.0- #7(1.3)- 0.05-2X	C(CFRP) -4.0- #7(1.3)- 0.15
Peak Shear	V_{max}^{+} [K]	45.46	48.7	82.0	50.8	45.7	60.6
	V_{max}^{-} [K]	48.0	49.3	81.3	50.6	46.9	60.5
	δ_{max}^{+} [IN]	3.91	2.30	4.74	3.57	3.09	2.41
	δ_{max}^{-} [IN]	4.10	3.13	4.90	5.90	3.04	2.33
	$\left(\frac{\delta}{H}\right)_{max}^{+}$ [%]	3.92	2.36	4.85	3.64	3.18	2.51
	$\left(\frac{\delta}{H}\right)_{max}^{-}$ [%]	4.41	3.30	5.10	6.24	3.21	2.43
Peak Base Moment	$\frac{M_{max}^{+}}{M_n}$	1.331	1.317	1.345	1.398	1.244	1.327
	$\frac{M_{max}^{-}}{M_n}$	1.279	1.315	1.336	1.435	1.278	1.327
	δ_{max}^{+} [IN]	7.88	4.73	4.74	4.24	3.09	3.77
	δ_{max}^{-} [IN]	9.85	4.64	4.90	5.90	4.72	5.64
	$\left(\frac{\delta}{H}\right)_{max}^{+}$ [%]	8.05	4.89	4.85	4.33	3.18	3.92
	$\left(\frac{\delta}{H}\right)_{max}^{-}$ [%]	10.4	4.87	5.10	6.24	4.96	5.88

Table 3.12: Deformation Capacity at Lateral Failure

Column I.D.	Lateral Failure			
	$\frac{\delta}{\delta_y}$ (Cycle Number)		Drift [%]	
	(+)	(−)	(+)	(−)
C(CFRP)- #7(1.3)-0.05	20.0 (1) +	15.0 (1) −	8.0	6.0
C(CFRP)-4.0-#5(1.4)-0.05	15.0 (2) +	15.0 (1) −	6.0	6.0
C(CFRP)-4.0-#7(2.7)-0.05	15.0 (1) +	15.0 (1) −	7.5	7.5
C(CFRP)-4.0-#7(1.3)-0.05-EQ	20.0 (1) +	20.0 (1) −	8.0	8.0
C(CFRP)-4.0-#7(1.3)-0.05-2X	15.0 (1) +	12.5 (4) −	6.0	5.0
C(CFRP)-4.0-#7(1.3)-0.15	12.5 (2) +	12.5 (2) −	6.25	6.25

3.2.3 Backbone Modeling

Bilinear backbone models, suitable for implementation into computer software used for conducting nonlinear time history analyses, were fit to the load-displacement response of each tested column in both the positive and negative loading direction, as shown in Figure 3.27.a through Figure 3.32.a for the applied shear demand and Figure 3.27.b through Figure 3.32.b for an effective shear demand that accounts for P-delta. Effective shear was computed as the base moment, including P-delta, divided by the column height of 96 inches. The procedure in ASCE/SEI-41 Section 7.4.3.2.4 (ASCE, 2017) was used for bilinear modeling. Although this procedure is prescribed for fitting a backbone model to results of a pushover analysis of a building, it was used for component modeling in this study. The first step in the procedure was the formulation of a test data backbone, which consisted of a piecewise linear fit to peaks of initial cycles, defined as any cycle that has a larger displacement that any previous cycle. The bilinear model was formulated by placing the terminal points at the origin and maximum load. The first line in the bilinear model intersected the test data backbone at 60% of the yield force. The yield point, located at the intersection of the lines in the bilinear model, was determined such that the area under the bilinear model was equal to the area under the test data curve between the origin and maximum load. Base moment, including P-delta, was used to determine the excursion with maximum loading.

From the backbone models, the effective stiffness and post-yield stiffness, K_e and K_p, respectively, were taken as the slope of the first and second lines of the bilinear model, respectively, as shown in Figure 3.33, and computed as:

$$K_e = \frac{V_y}{\delta_y} \tag{3-2}$$

$$K_p = \frac{V_{max} - V_y}{\delta_{max} - \delta_y} \tag{3-3}$$

where V_y and δ_y are the base shear and displacement at yielding, respectively, and V_{max} and δ_{max} are the maximum shear and corresponding displacement, respectively, all determined by the bilinear backbone modeling procedure. Values of K_e and K_p for both the applied shear and effective shear backbones are provided in Table 3.13 for each of the six test columns in each of the two loading directions. Assuming all deformation in the cantilever column was due to bending, K_e was converted to an effective flexural rigidity, I_{eff} , as:

$$EI_{eff} = \frac{V_y H^3}{3\delta_y} = \frac{H^3}{3} K_e \tag{3-4}$$

where H is the height of the column. Resulting values for $(EI)_{eff}$ and $(EI)_{eff}/\left(E_c I_g\right)$ are additionally reported in Table 3.13 where E_c is the modulus of elasticity of concrete, and I_g is the moment of inertia of the gross concrete column section without the CFRP jacket included. The average tested concrete strength from all column cylinder tests, shown in Table 3.4, was 3.95-ksi, was used to compute $E_c = 3580$-ksi using:

$$E_c[ksi] = 57\sqrt{f_C' \ [psi]} \tag{3-5}$$

ACI 318-19 Section 19.2.2.1. C(CFRP)-4.0-#7(1.3)-0.15 had the largest $(EI)_{eff}$ in both directions, likely attributed to increased concrete strength from the increased axial loads. C(CFRP)-4.0-#7(1.3)-0.05 had the lowest $(EI)_{eff}$ in the positive direction and C(CFRP)-4.0-#7(1.3)-0.05-EQ had the lowest $(EI)_{eff}$ in the negative direction. Since these columns only differ in loading protocol it is not surprising that their $(EI)_{eff}$ values are similar. The three columns with the same layout, C(CFRP)-4.0-#7(1.3)-0.05, C(CFRP)-4.0-#7(1.3)-0.05-EQ, and C(CFRP)-4.0-#7(1.3)-0.05-2X, had an average $(EI)_{eff}/\left(E_c I_g\right)$ of 0.433 with a COV of 10.5% in the positive direction and 0.458 with a COV of 19.7% in the negative direction.

Bilinear models and test data backbones, normalized by lateral load at yielding determined from the bilinear model fit, are provided in Figure 3.34 and Figure 3.35, respectively. Directional variability was evident from the asymmetry of $(EI)_{eff}$ values for C(CFRP)-4.0-#7(1.3)-0.05, C(CFRP)-4.0-#5(1.4)-0.05, C(CFRP)-4.0-#7(2.7)-0.05, and C(CFRP)-4.0-#7(1.3)-0.05-EQ. C(CFRP)-4.0-#7(1.3)-0.15 had the lowest directional variability of the 6 columns with the negative direction having only 0.03% increase in $(EI)_{eff}$ compared to the positive direction. C(CFRP)-4.0-#5(1.4)-0.05 and C(CFRP)-4.0-#7(1.3)-0.05-EQ are the only columns to have a lower $(EI)_{eff}$ in the negative direction than the positive direction.

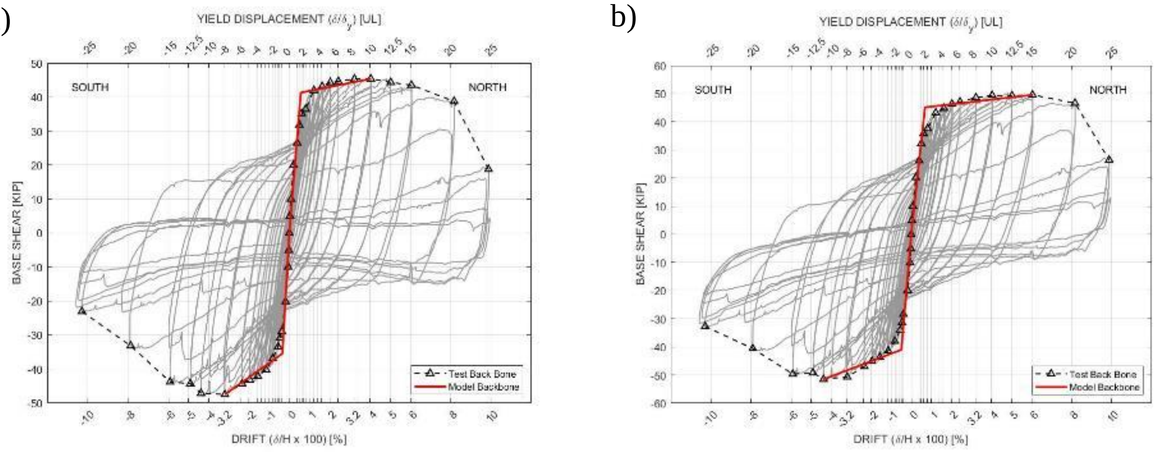
a)
b)

Figure 3.27. Backbone Model Fit for C(CFRP)-4.0-#7(1.3)-0.05: a) Base Shear, b) Effective Base Shear

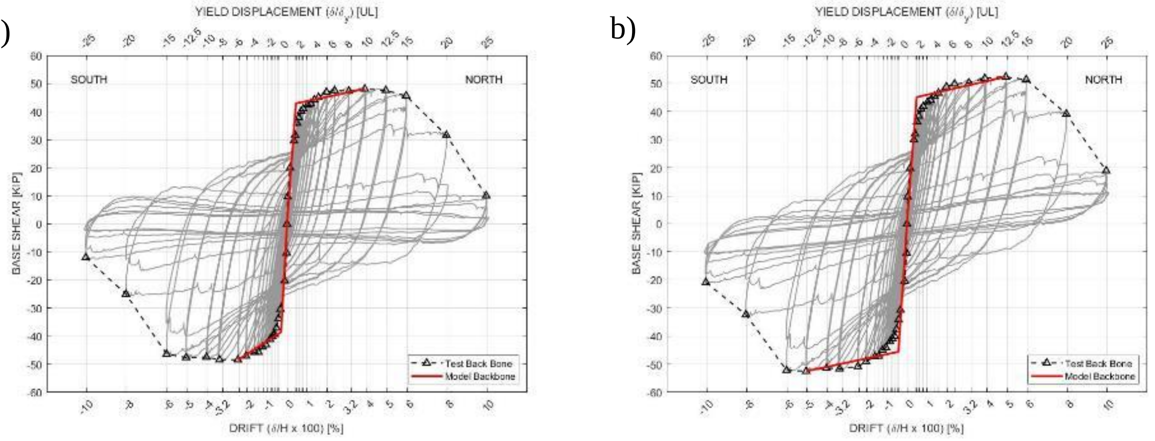
a)
b)

Figure 3.28. Backbone Model Fit for C(CFRP)-4.0-#5(1.4)-0.05: a) Base Shear, b) Effective Base Shear

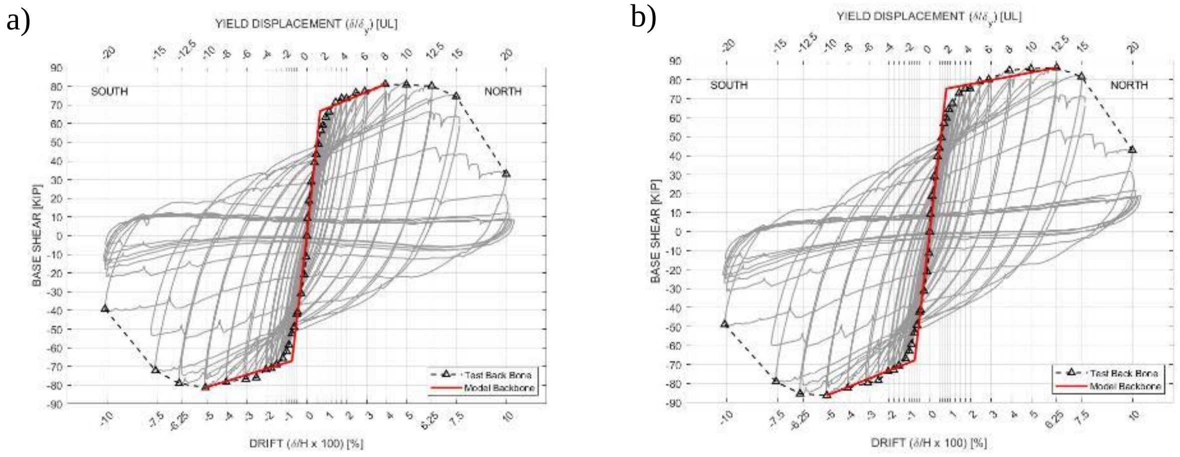

Figure 3.29. Backbone Model Fit for C(CFRP)-4.0-#7(2.7)-0.05: a) Base Shear, b) Effective Base Shear

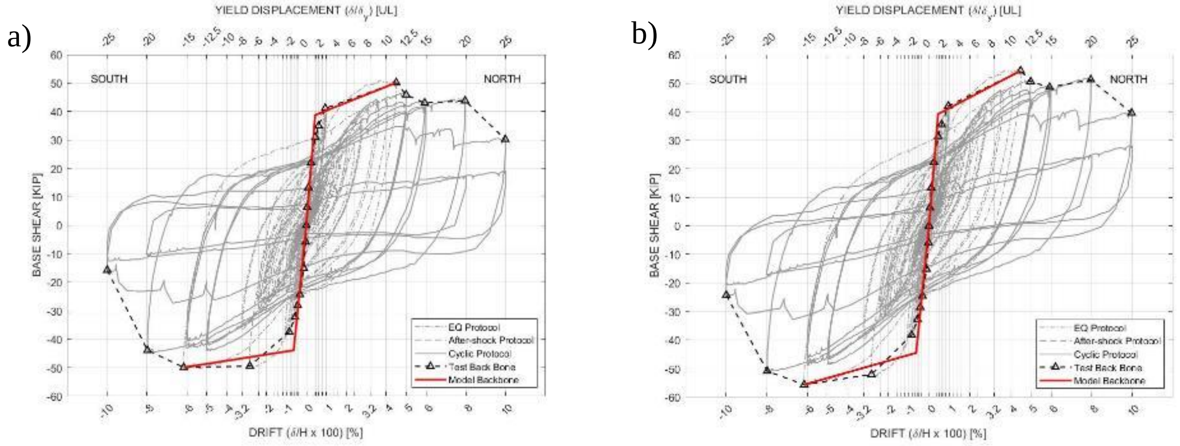

Figure 3.30. Backbone Model Fit for C(CFRP)-4.0-#7(1.3)-0.05-EQ: a) Base Shear, b) Effective Base Shear

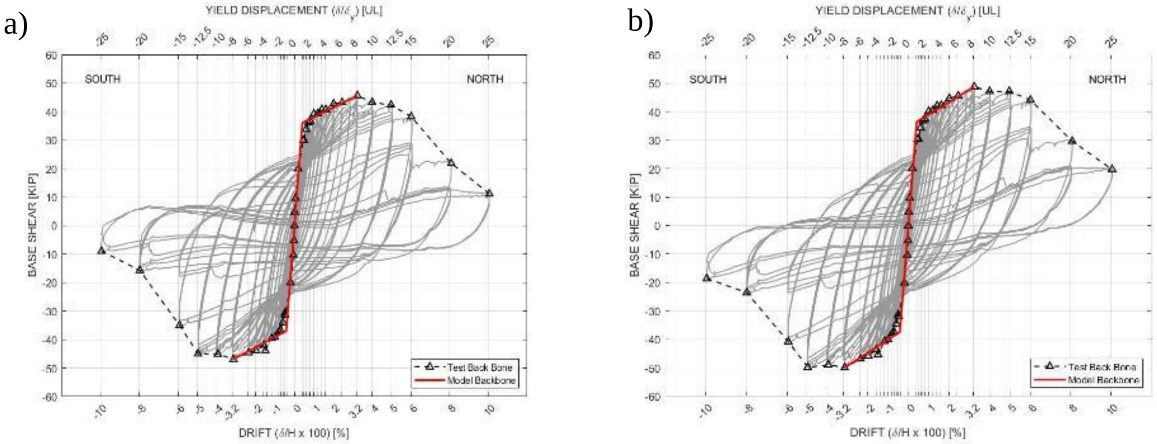

Figure 3.31. Backbone Model Fit for C(CFRP)-4.0-#7(1.3)-0.05-2X: a) Base Shear, b) Effective Base Shear

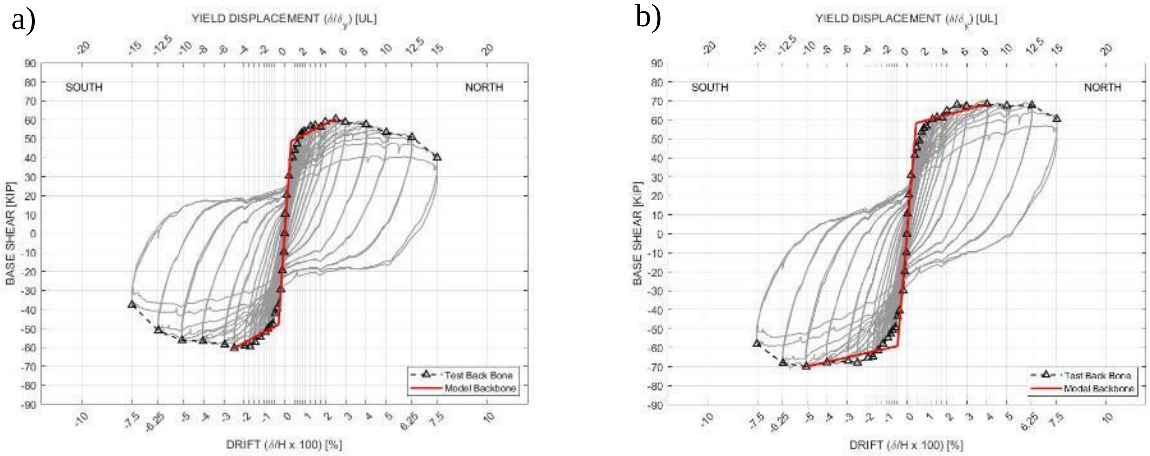

Figure 3.32. Backbone Model Fit for C(CFRP)-4.0-#7(1.3)-0.15: a) Base Shear, b) Effective Base Shear

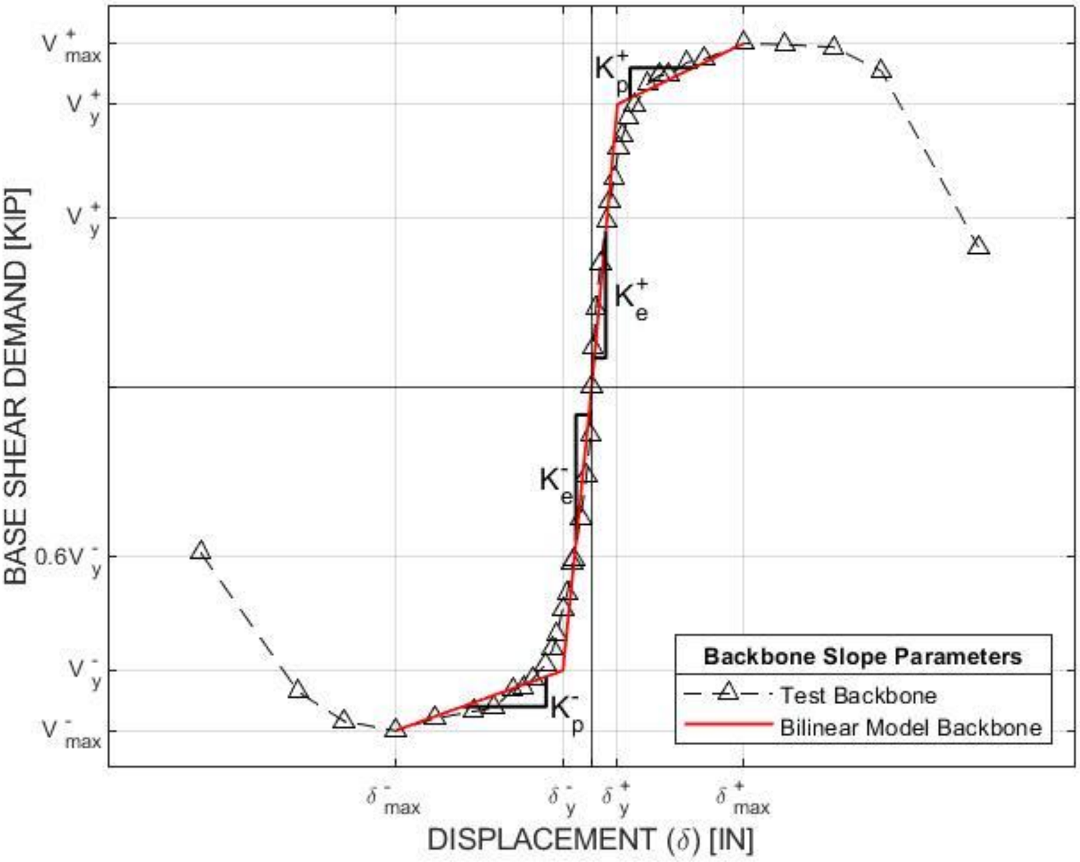

Figure 3.33. Bilinear Model Backbone Slope Parameters

Table 3.13: Stiffness and Strength of Backbone Models

Load	Parameter	C(CFRP) -4.0- #7(1.3) -0.05	C(CFRP) -4.0- #5(1.4) -0.05	C(CFRP) -4.0- #7(2.7) -0.05	C(CFRP) -4.0- #7(1.3) -0.05-EQ	C(CFRP) -4.0- #7(1.3) -0.05-2X	C(CFRP) -4.0- #7(1.3) -0.15
Base Shear	$K_e(+)^\dagger$	75.23	104.32	99.78	90.74	90.98	156.18
	$K_p(+)^\dagger$	1.217	4.587	1.564	2.915	3.511	5.573
	$K_e(-)^\dagger$	107.68	93.79	137.27	72.03	91.89	168.39
	$K_p(-)^\dagger$	4.393	3.422	4.792	1.134	3.786	5.918
	$(EI)_{eff}(+)^\ddagger$	2.219	3.077	2.943	2.676	2.683	4.606
	$\frac{(EI)_{eff}}{E_C I_g}(+)^\S$	0.3803	0.5274	0.5045	0.4587	0.4600	0.7896
	$(EI)_{eff}(-)^\ddagger$	3.176	2.766	4.048	2.124	2.710	4.966
	$\frac{(EI)_{eff}}{E_C I_g}(-)^\S$	0.5443	0.4741	0.6940	0.3641	0.4646	0.8513
Effective Base Shear	$K_e(+)^\dagger$	68.36	96.19	96.76	91.67	92.05	131.13
	$K_p(+)^\dagger$	86.08	212.73	169.49	389.23	453.15	295.79
	$K_e(-)^\dagger$	86.64	94.87	110.67	73.01	92.88	131.16
	$K_p(-)^\dagger$	281.22	446.02	156.50	210.75	481.44	246.10
	$(EI)_{eff}(+)^\ddagger$	2.106	2.837	2.854	2.703	2.715	3.867
	$(EI)_{eff}(-)^\ddagger$	2.555	2.798	3.264	2.153	2.739	3.868
	$\frac{(EI)_{eff}}{E_C I_g}(+)^\S$	0.3456	0.4863	0.4892	0.4634	0.4654	0.6629
	$\frac{(EI)_{eff}}{E_C I_g}(-)^\S$	0.4378	0.4796	0.5595	0.3691	0.4696	0.6631

† [kip/in]
‡ [kip-in^2 $\times 10^7$]
§[UL]

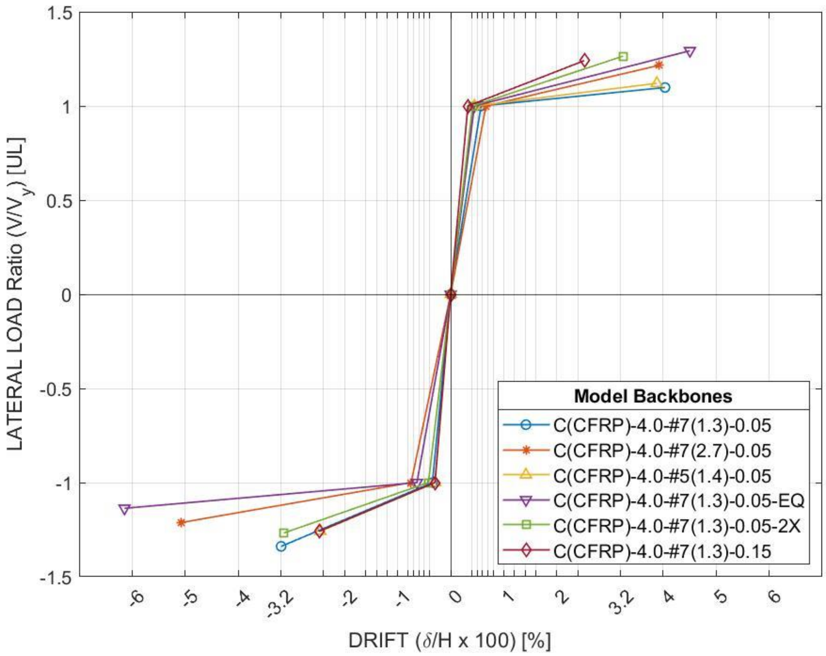

Figure 3.34. Normalized Bilinear Backbone Model Plots

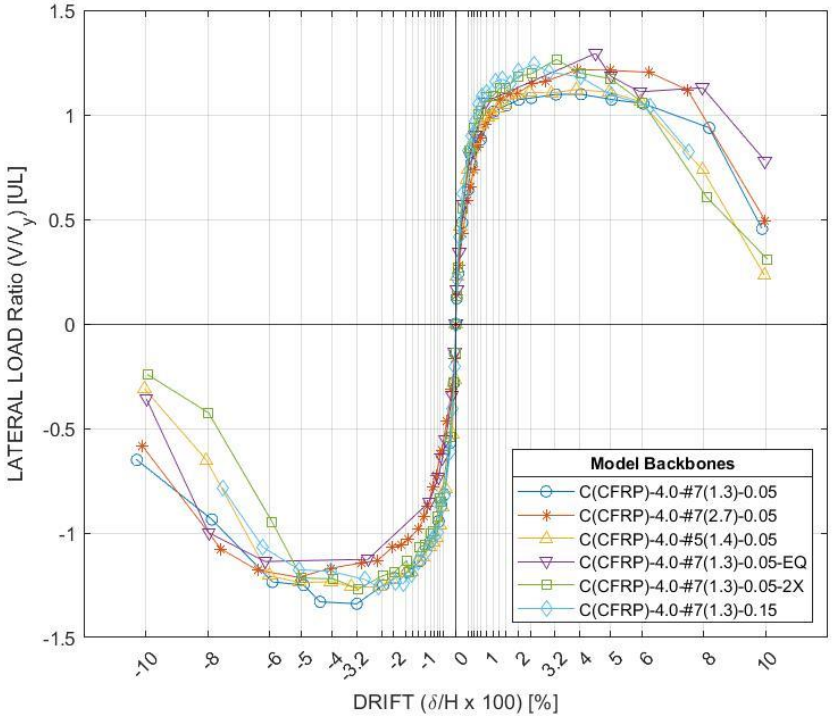

Figure 3.35. Normalized Test Data Backbone Plots

3.2.4. Effective Secant Stiffness

Effective secant stiffness, K_{sec}, was determined for each initial cycle (i.e., each point on the test data backbone) as the slope of the line from the origin to that point. Assuming all deformation in the cantilever column was due to bending, K_{sec} was converted to an effective flexural rigidity, $(EI)_{sec}$, as:

$$(EI)_{sec} = \frac{K_{sec}H^3}{3} = \frac{VH^3}{3\delta} \tag{3-6}$$

Plots of $EI_{sec}/\left(E_C I_g\right)$ versus drift with data points connected by lines are provided in Figure 3.36. As expected, C(CFRP)-4.0-#7(2.7)-0.05 and C(CFRP)-4.0-#7(1.3)-0.15, which had greater longitudinal reinforcement ratio and higher axial load, respectively, than the other columns, exhibited greater stiffness at given drift levels. Minor variation was observed between C(CFRP)-#7(1.3)-0.05, C(CFRP)- #7(1.3)-0.05-EQ, and C(CFRP)-4.0-#7(1.3)-0.05-2X, which had the same longitudinal reinforcement layout and axial load.

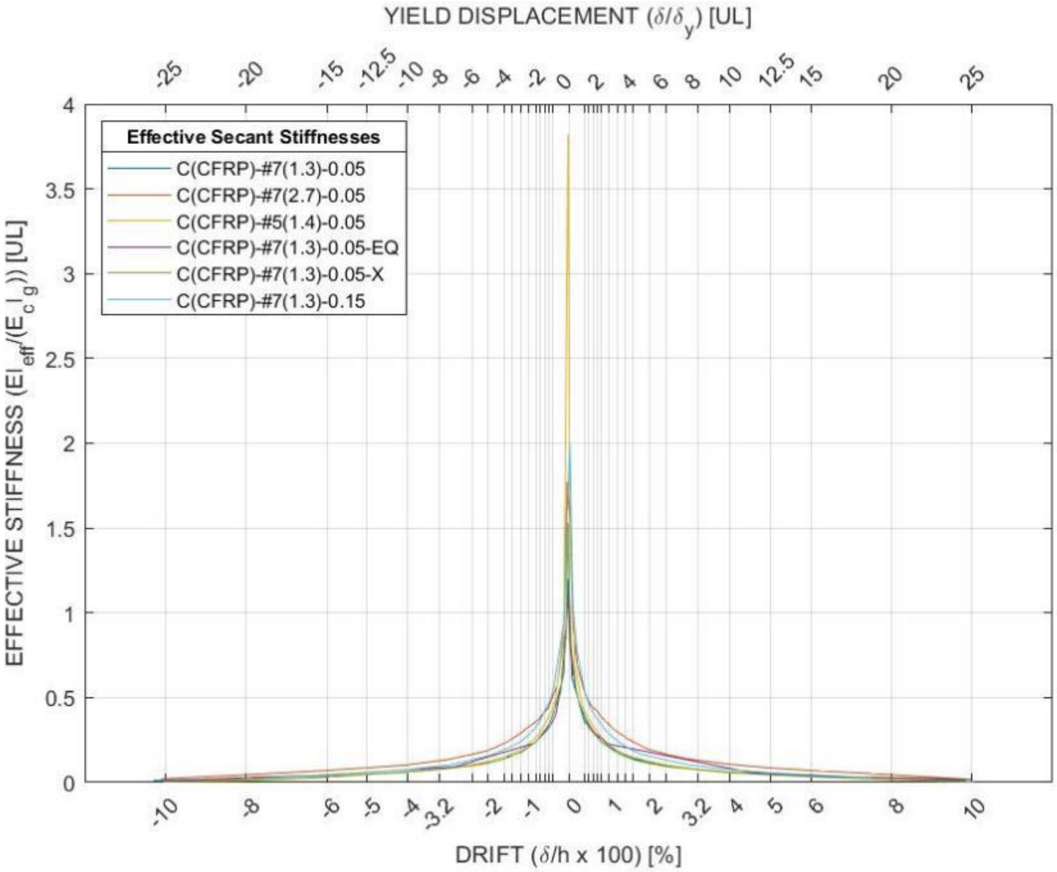

Figure 3.36. Effective Secant Stiffness Plots

3.2.5. Reinforcement Strain

Measurements obtained from the strain gauges shown in Figure 3.10 and Figure 3.11 were plotted in Figures 4.22 through Figures 4.26 for initial cycle peaks at various drift levels. Negative values on the y-axes indicate strain gauges in the footing. Yield strain, ϵ_y, is shown on the plots and was determined from the reinforcement stress-strain data provided in Figure 3.7. During positive loading excursions, the South reinforcement was in tension and the North reinforcement was in compression. Gauges tended to become damaged as testing progressed, leading to sparser data at increased drift levels. Some gauges malfunctioned before testing commenced, and these data were omitted. Gauge results for C(CFRP)-4.0-#7(1.3)-0.05 were not available due issues with gauges. Two gauges were used at 0.05-in above the column-footing interface, and, when both gauges were functioning, average values were reported.

Generally, strains increased with greater magnitude excursions. Most columns had larger strain in the tension than compression direction, as expected, and this trend was most prominent for C(CFRP)-4.0-#5(1.4)-0.05 and C(CFRP)-4.0-#7(1.3)-0.05-EQ. C(CFRP)-4.0-#7(1.3)-0.05-EQ, C(CFRP)-4.0-#7(1.3)-0.05-2X, and C(CFRP)-4.0-#7(1.3)-0.15 all exhibited higher strains further from the column-footing interface, whereas C(CFRP)-4.0-#5(1.4)-0.05 exhibited higher strains closer to the column-footing interface. Reinforcement yielding was reached in all columns. C(CFRP)-4.0-#7(1.3)-0.05-EQ and C(CFRP)-4.0-#7(1.3)-0.15 both exhibited reinforcement yielding at the sensor farthest below the column-footing interface. C(CFRP)-4.0-#7(1.3)-0.05-EQ also exhibited reinforcement yielding at the sensor farthest above the column footing interface. All other columns exhibited at least 80% of the yield strain in one of the sensors at least 8-in away from the column-footing interface.

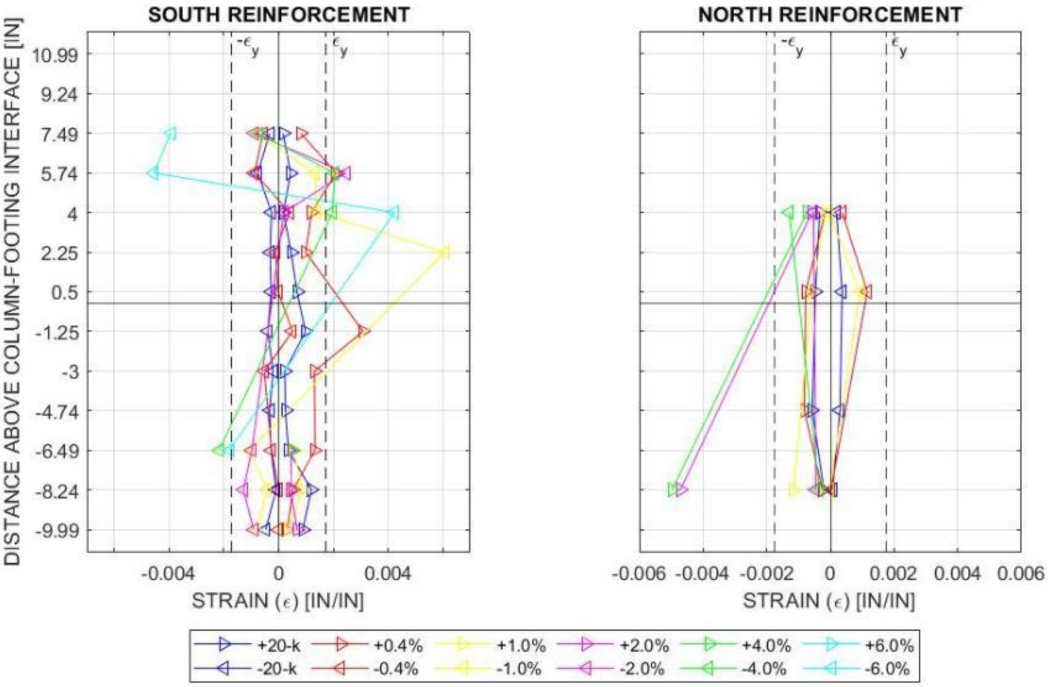

Figure 3.37. Strain Measured in Longitudinal Reinforcement at Cycle Peaks, C(CFRP)-4.0-#5(1.4)-0.05

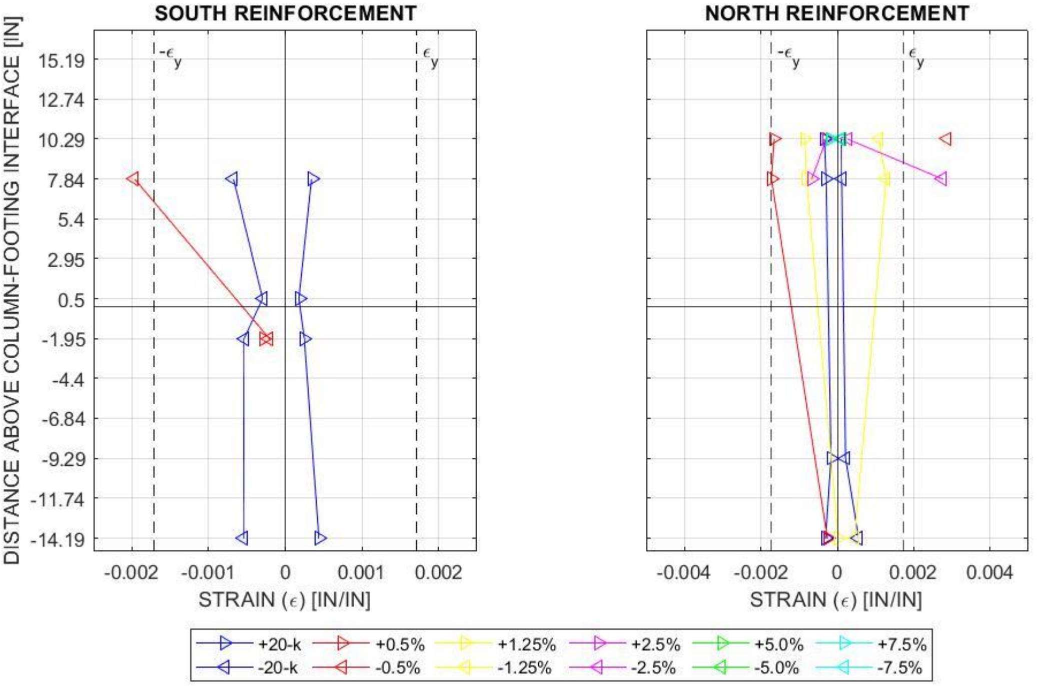

Figure 3.38. Strain Measured in Longitudinal Reinforcement at Cycle Peaks, C(CFRP)-4.0-#7(2.7)-0.05

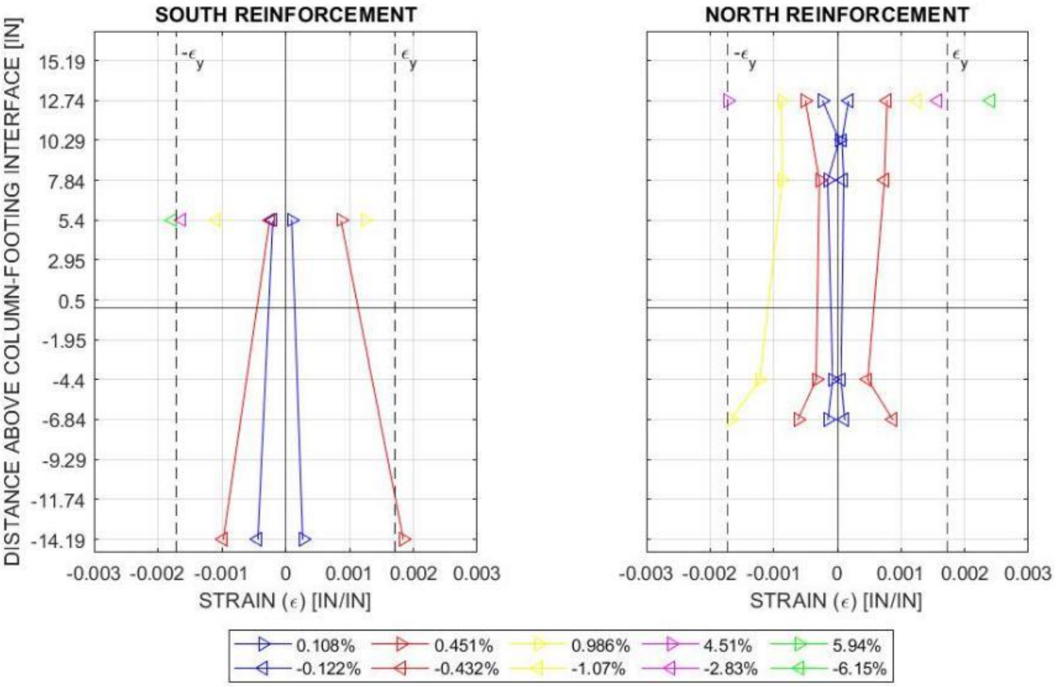

Figure 3.39. Strain Measured in Longitudinal Reinforcement at Cycle Peaks, C(CFRP)-4.0-#7(1.3)-0.05-EQ

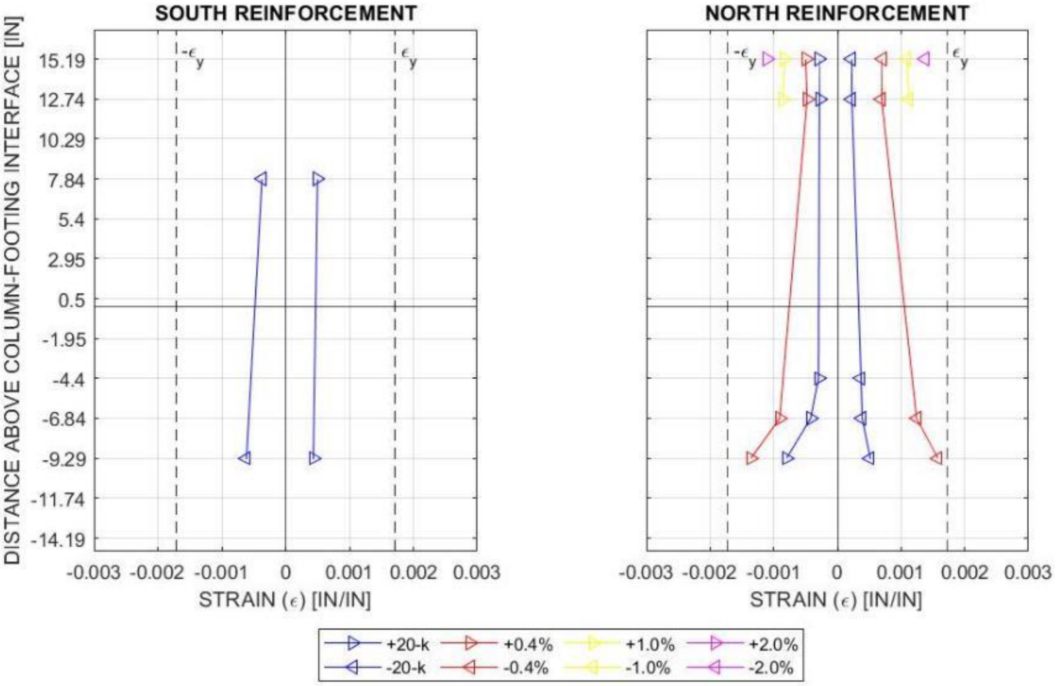

Figure 3.40. Strain Measured in Longitudinal Reinforcement at Cycle Peaks, C(CFRP)-4.0-#7(1.3)-0.05-2X

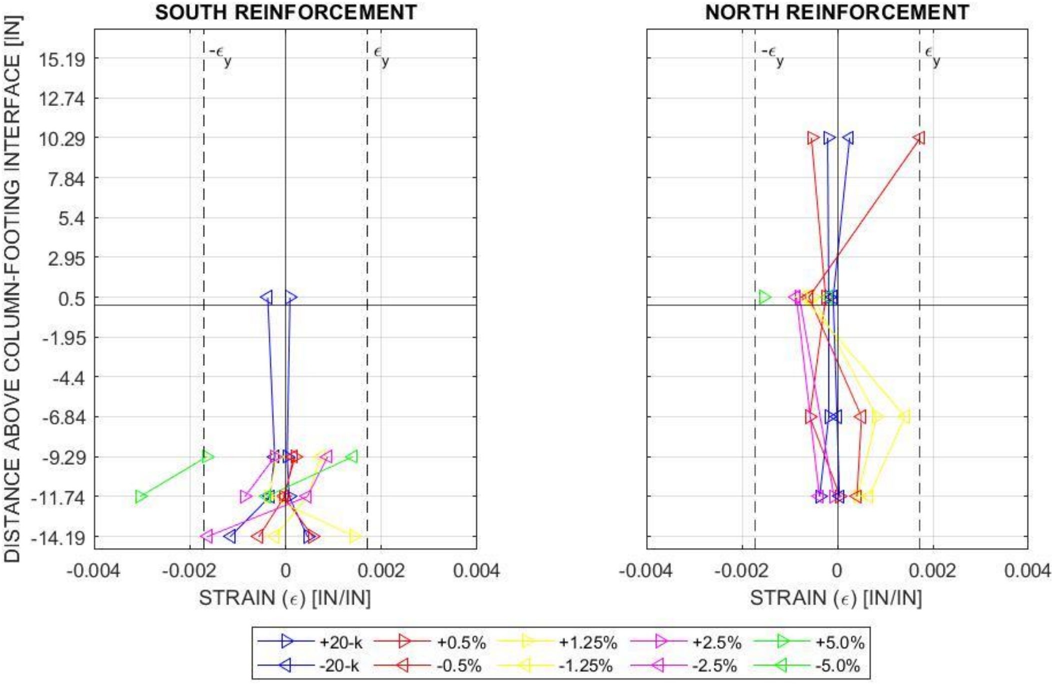

Figure 3.41. Strain Measured in Longitudinal Reinforcement at Cycle Peaks, C(CFRP)-4.0-#7(1.3)-0.15

3.2.6. Column Curvature

Curvature was determined using the vertically oriented LVDTs in the column, shown in Figure 3.13. At each height increment, curvature was determined using the two North-South Sensors, with plots of the values provided in Figure 3.42. Results were more limited at advanced deformation levels due to damage interfering with instrumentation. It is evident that curvature demand concentrated in the lower 6 inches of the columns. However, at a height of 0.5-in, the deformation is primarily due to bond slip and extension, such that the strain determined from the LVDTs over the lower 0.5-in is not reflective of true curvature. Column curvatures excluding data for the lower 0.5-in are provided in Figure 3.43. The calculated yield curvatures shown in Figure 3.42 and Figure 3.43 were computed using moment-curvature analysis with the steel reinforcement material properties provided in Table 3.2 and the concrete material properties provided in Table 3.3. Measured curvature did not exceed calculated yield curvature at locations more than 4-in above the column-footing interface. The exception was C(CFRP)-4.0-#7(1.3)-0.15, in which curvature exceeded the calculated yield curvature at 12-in above the column-footing interface at 2% and greater drift in the positive direction and 4% and greater drift in the negative direction. It is noted that data was excluded from Figure 3.42 and Figure 3.43 due to issues with sensors.

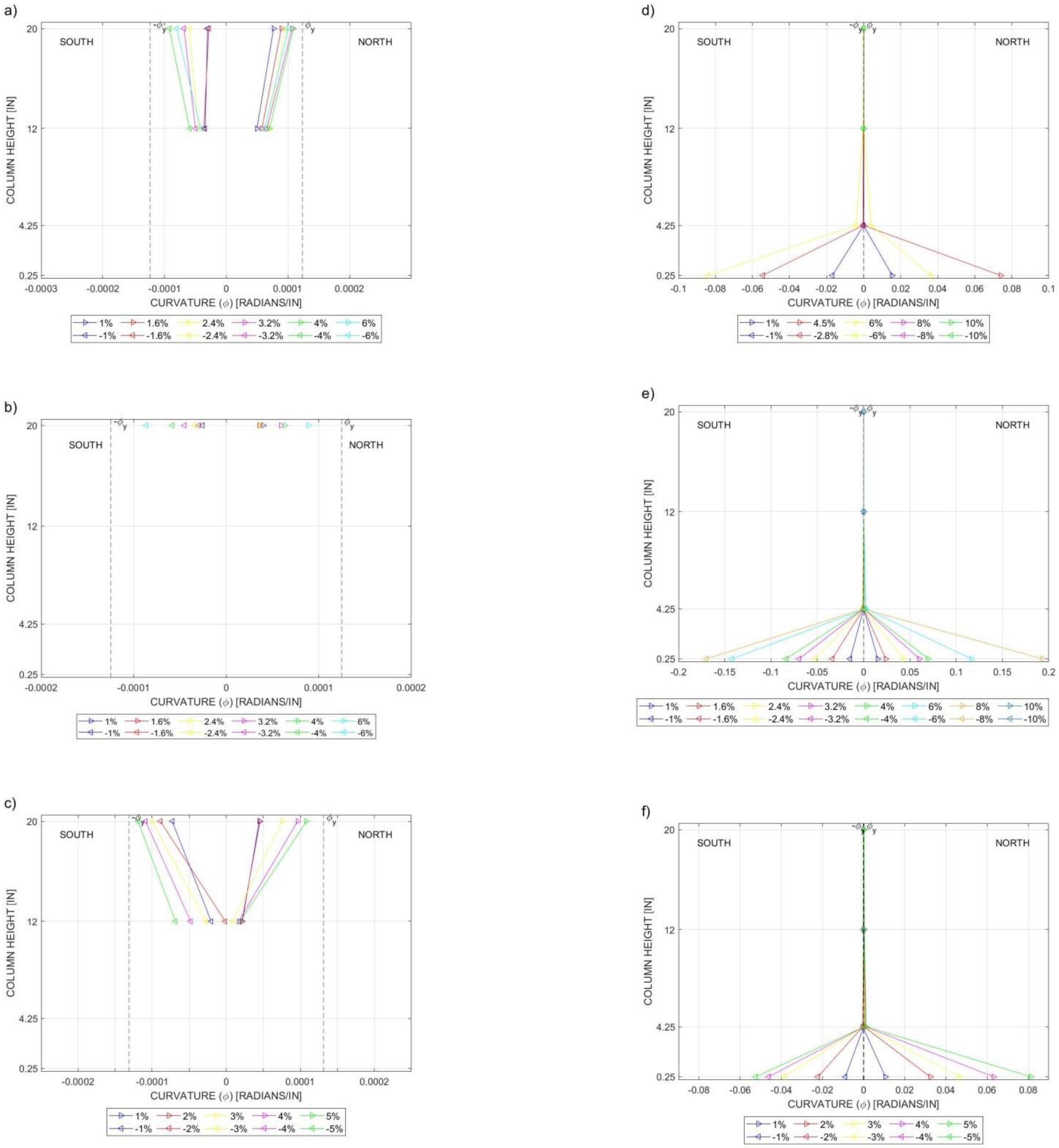

Figure 3.42. Measured Curvature: a) C(CFRP)-4.0-#7(1.3)-0.05, b) C(CFRP)-4.0-#5(1.4)-0.05, c) C(CFRP)-4.0-#7(2.7)-0.05, d) C(CFRP)-4.0-#7(1.3)-0.05-EQ, e) C(CFRP)-4.0-#7(1.3)-0.05-2X, f) C(CFRP)-4.0-#7(1.3)-0.15

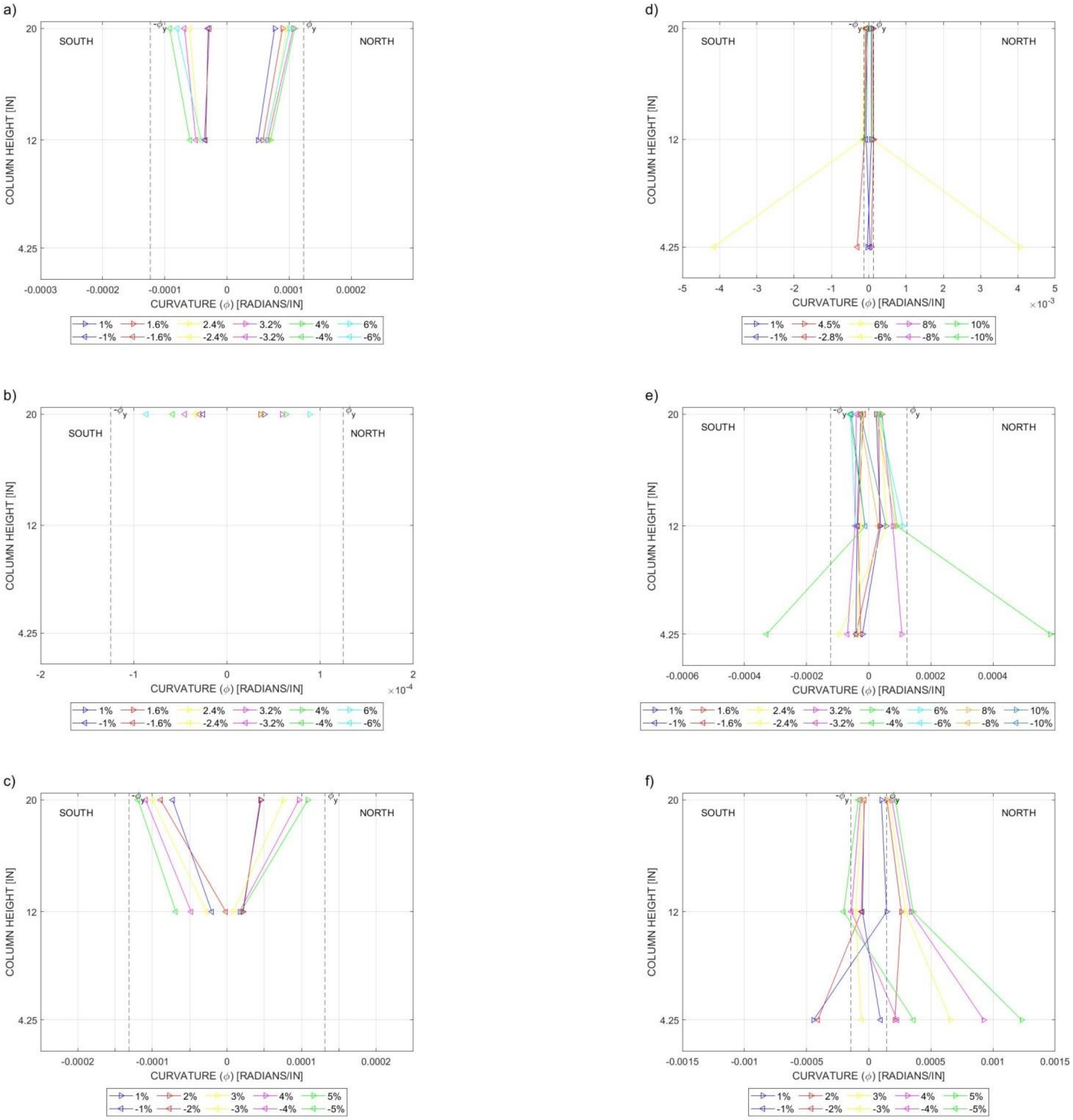

Figure 3.43. Measured Curvature Excluding Bond Slip: a) C(CFRP)-4.0-#7(1.3)-0.05, b) C(CFRP)-4.0-#5(1.4)-0.05, c) C(CFRP)-4.0-#7(2.7)-0.05, d) C(CFRP)-4.0-#7(1.3)-0.05-EQ, e) C(CFRP)-4.0-#7(1.3)-0.05-2X, f) C(CFRP)-4.0-#7(1.3)-0.15

3.2.7. Shear Sliding and Base Rotation

Shear sliding and base twisting were determined using the horizontally oriented sensors spanning from the footing to the base of the column, with sensor locations shown in Figure 3.12. Plots of shear sliding and base twisting versus base shear are provided in Figure 3.43 and Figure 3.44, respectively, with clockwise and counter-clockwise indicating column twist direction relative to the footing. Data for C(CFRP)-4.0-#7(1.3)-0.05 were omitted due to sensor error. Included data for all columns were more limited at advanced deformation levels due to damage interfering with instrumentation. C(CFRP)-4.0-#7(2.7)-0.05 had the most shear sliding of any test, reaching almost 0.7-in of sliding in both directions. C(CFRP)-4.0-#7(1.3)-0.15 had the least shear sliding and base rotation, with less than 0.15-in of shear sliding in both directions and a maximum base twisting rotation of 0.0042 radians in the clockwise direction and 0.0000 radians in the counter clockwise direction. C(CFRP)-4.0-#5(1.4)-0.05, C(CFRP)-4.0-#7(2.7)-0.05, C(CFRP)-4.0-#7(1.3)-0.05-EQ, and C(CFRP)-4.0-#7(1.3)-0.05-2X had more shear sliding in the negative loading direction, while C(CFRP)-4.0-#7(1.3)-0.15 had more shear sliding in the positive loading direction. C(CFRP)-4.0-#7(1.3)-0.05-EQ had the most discrepancy in shear sliding in the positive and negative directions, with 1.92 times as much shear sliding in the negative direction than in the positive direction. This column had the most base rotation of any of the columns, with a maximum base twisting rotation of 0.094 radians in the clockwise direction and 0.033 radians in the counter clockwise direction. The twisting caused out-of-plane translation due to ratcheting, as described in Section 3.2.1.1.

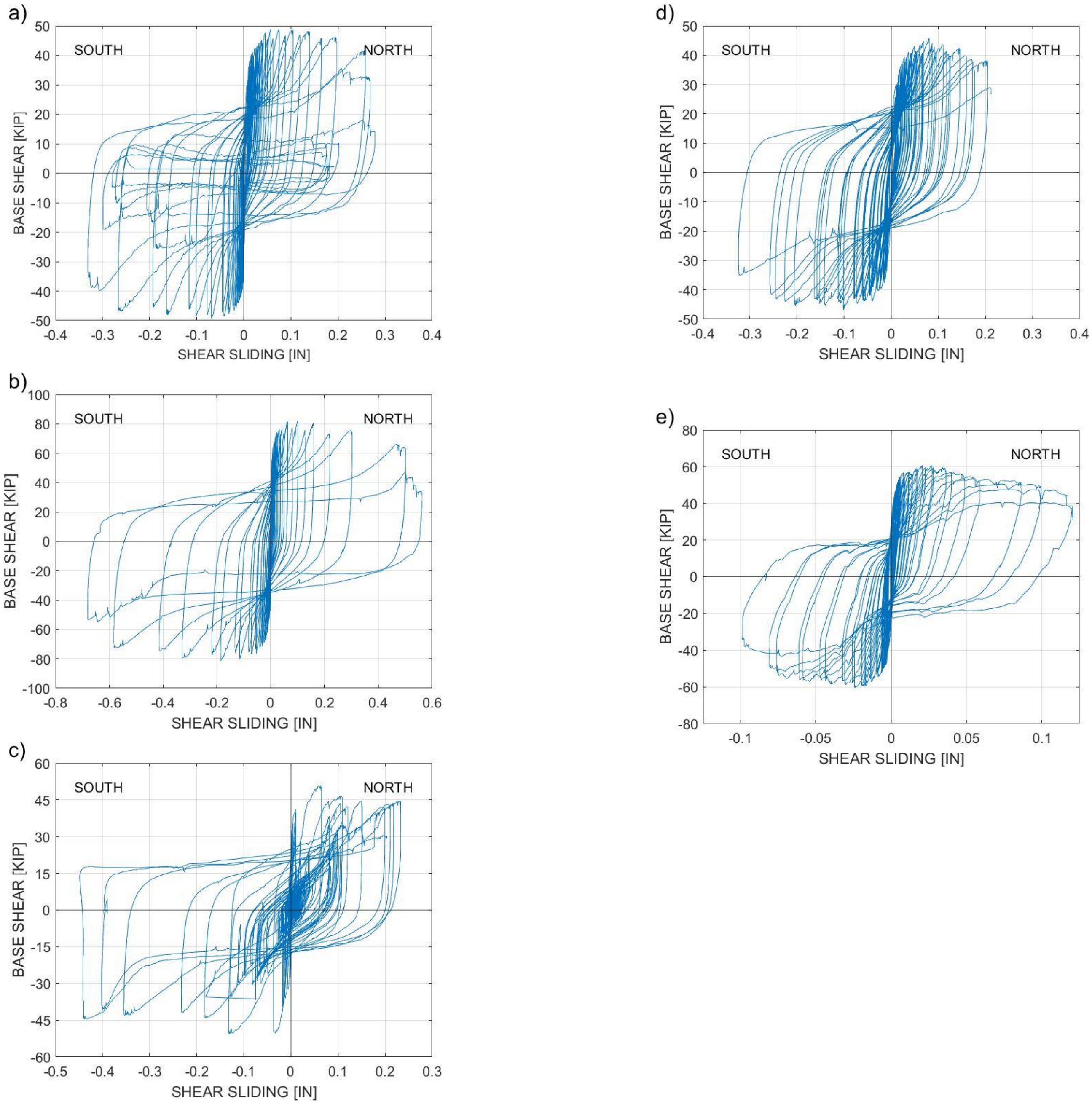

Figure 3.44. Shear Sliding: a) C(CFRP)-4.0-#5(1.4)-0.05, b) C(CFRP)-4.0-#7(2.7)-0.05, c) C(CFRP)-4.0-#7(1.3)-0.05-EQ, d) C(CFRP)-4.0-#7(1.3)-0.05-2X, e) C(CFRP)-4.0-#7(1.3)-0.15

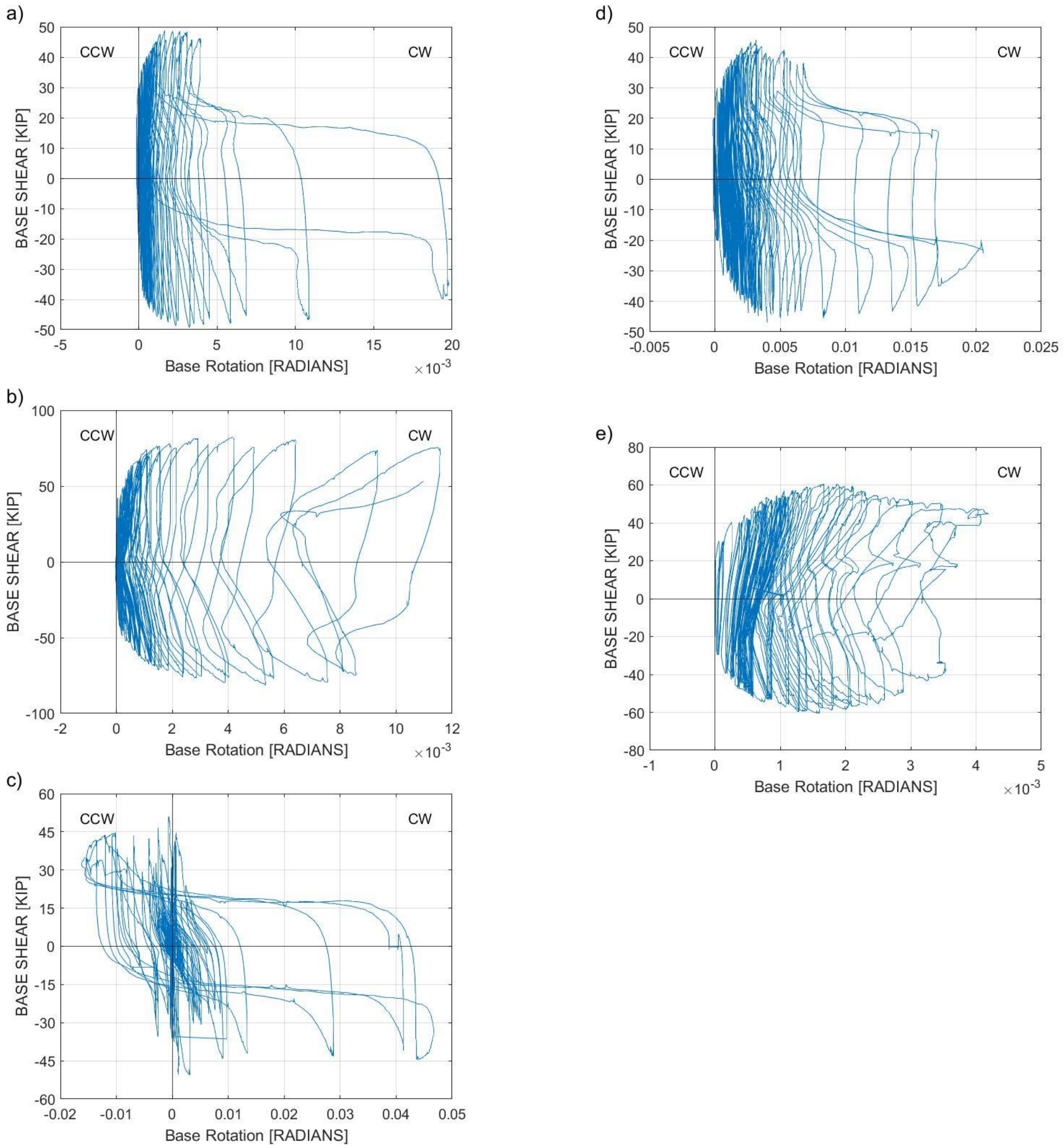

Figure 3.45. Base Rotation: a) C(CFRP)-4.0-#5(1.4)-0.05, b) C(CFRP)-4.0-#7(2.7)-0.05, c) C(CFRP)-4.0-#7(1.3)-0.05-EQ, d) C(CFRP)-4.0-#7(1.3)-0.05-2X, e) C(CFRP)-4.0-#7(1.3)-0.15

3.2.8. Components of Deformation

The components of deformation for the six tests at peaks of initial cycles are provided in Figure 3.45. The components are provided as a percentage of the overall column displacement and drift. "Flexure in the Jacket" was determined from the curvature over the height of the jacket, using curvature values shown in Figure 3.42 with constant curvature assumed over the length of the sensor (i.e., center of rotation at mid-height of the sensor length). This did not include the curvature in the bottom 0.5-in of the column, which contained bar slip and elongation. The lower 0.5-in of the column, which was included separately in the figure as "Bond Slip/Elongation", was determined from the rotation measured over the lower 0.5-in of the column. The shear sliding described in Section 3.2.7 is included in Figure 3.45 as "shear sliding". Estimated shear deformation, presented in Figure 3.45 as "Estimated Shear", was computed as:

$$\Delta_{shear} = \frac{Vh}{(A_V G)_{eff}} \qquad (3\text{-}8)$$

where V is the shear force at the base of the column, h is the height of the column shear span, and $(A_v G)_{eff}$, is the effective shear rigidity, which was computed using the recommended value in Appendix A of ACI 318-19 as:

$$(A_V G)_{eff} = 0.4 E_c A_g \qquad (3\text{-}7)$$

where E_c is the concrete modulus of elasticity of concrete and A_g is the gross cross-sectional area. The “Other” category is the displacement or drift not accounted for by the previously mentioned components. This includes flexural deformation above the jacket, as well as any sources of error. For C(CFRP)-4.0-#5(1.4)-0.05 and C(CFRP)-4.0-#7(2.7)-0.05 the “Other” category constitutes everything but shear sliding and estimated shear displacement, due to sensor error described in Section 3.2.6. Similarly, C(CFRP)-4.0-#7(1.3)-0.05 was omitted due to the sensor malfunctions described in Sections 4.2.6 and 4.2.7.

As evident from Figures 4.31.c. through 4.31.e., the majority of the deformation occurred at the bottom 0.5-in of the column, with shear sliding contributing minimally to the overall deformation. Shear sliding between -5.6% and 12.7%for all columns. Flexure in the jacket also contributed minimally to the overall deformation with a minimum contribution of -10.8% and a maximum contribution of 7.0% for C(CFRP)-4.0-#7(1.3)-0.05-EQ, C(CFRP)-4.0-#7(1.3)-0.05-2X, and C(CFRP)-4.0-#7(1.3)-0.15. The estimated shear deformation had a maximum contribution of 11.8% across all columns. The majority of the deformation was due to bond slip/elongation and other sources. The contribution from bond slip and elongation generally increased as drift increased. An increase in “other” with increase in damage above the jacket was evident in the negative direction for C(CFRP)-4.0-#7(1.3)-0.15, which failed above the jacket, as described in Section 3.2.1.1.

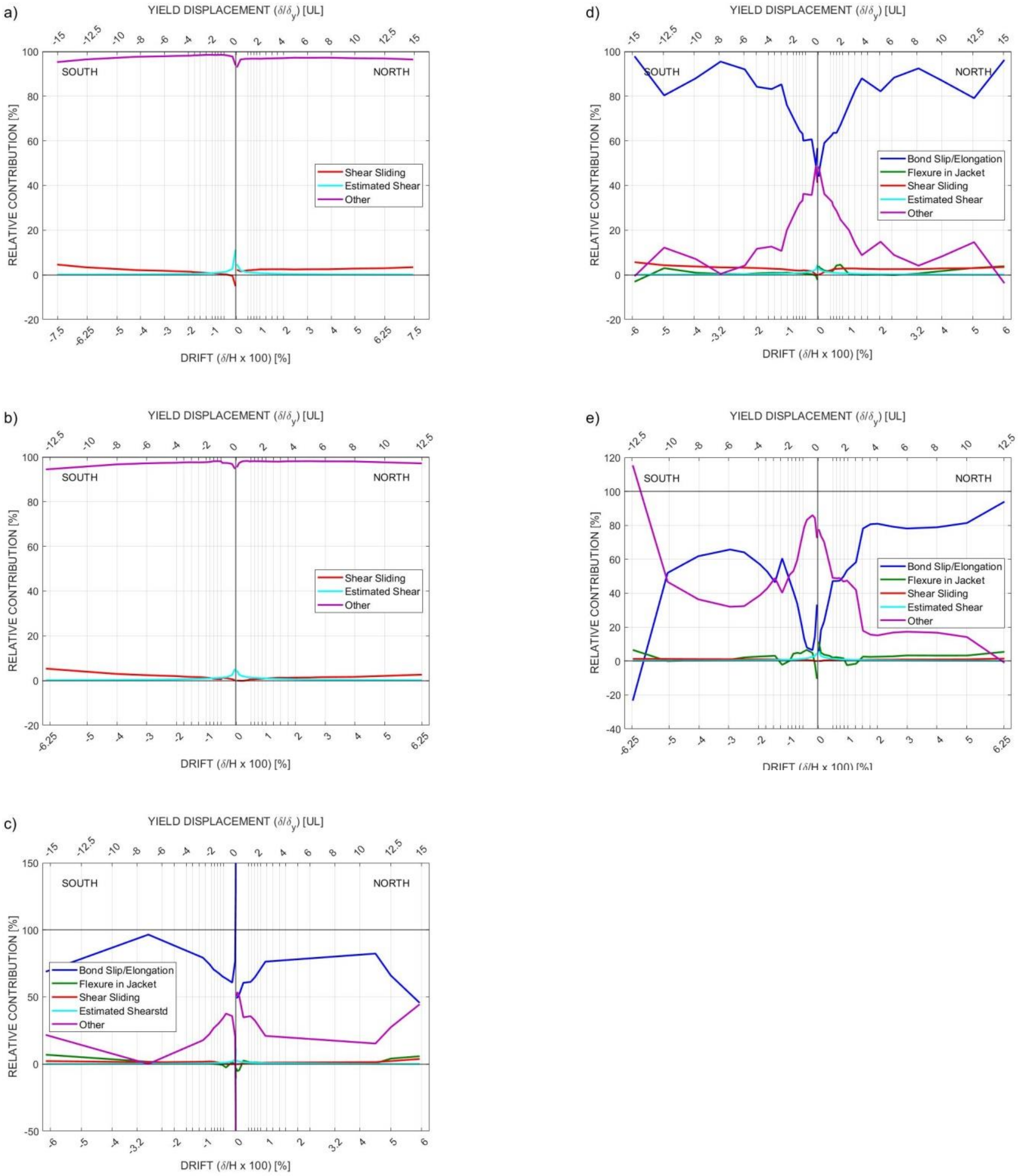

Figure 3.46. Components of Deformation: a) C(CFRP)-4.0-#5(1.4)-0.05, b) C(CFRP)-4.0-#7(2.7)-0.05, c) C(CFRP)-4.0-#7(1.3)-0.05-EQ, d) C(CFRP)-4.0-#7(1.3)-0.05-2X, e) C(CFRP)-4.0-#7(1.3)-0.15

4. Column Modeling

4.1. Methodology

Failure of the FRP jacket retrofitted bridge columns was due to low-cycle fatigue fracture of longitudinal reinforcement. Predicting the drift and cycle at failure for a given column is contingent upon predicting low-cycle fatigue failure of longitudinal reinforcement. Many existing models for low-cycle fatigue fracture of reinforcement are based on plastic strain history (Uriz and Mahin, 2008; Huang and Mahin, 2008; Kanvinde, 2004; Padilla-Llano et al., 2018). A column hinge rotation model was used to formulate a relationship between the strain in the reinforcement and the column drift.

The column model, shown in Figure 4.1, consisted of a linear elastic line element, a fiber section element over the 1" clear cover to the footing top reinforcement, and a bond slip element at the footing column interface and at 1" into the footing. The spread of plasticity into the column was not modeled, as it was evident from test data in Section 3.2.6 that the spread of plasticity in the jacketed region was minimal. The use of a fiber section in the concrete cover was intended to account for the concrete spalling that occurred, as described in Section 3.2.1.1. The bond slip elements were intended to model strain penetration into the footing and into the jacket. In this model, the plastic hinge length, L_p, was 1", which was concrete cover dimension, and plastic deformation was modeled to occur in the fiber section element and in the two zero-length bond slip elements. Rotation in the plastic hinge, θ_p, is related to drift ratio as:

$$\theta_p = \frac{(\Delta - \Delta_y)}{\left(H + \frac{L_p}{2}\right)} = \frac{\Delta_p}{\left(H + \frac{L_p}{2}\right)} \tag{4-1}$$

where Δ is the total lateral displacement at the top of the column, Δ_y is the lateral displacement at yield, Δ_p is the plastic lateral displacement, H is the column clear height, and $L_p/2$ is the height of the plastic hinge center of rotation below the base of the column. Previous research (Chai et al, 1991) has shown that plastic curvature in steel jacket retrofitted columns concentrates at the base at the gap between the steel jacket and the foundation. Because L_p is small relative to the height of the column, plastic hinge rotation may be approximated as plastic drift ratio:

$$\theta_p = \frac{\Delta_p}{(H - H_{hinge})} = \frac{\Delta_p}{\left(H - \frac{L_{gap}}{2}\right)} \approx \frac{\Delta_p}{H} \tag{4-2}$$

Resulting in a linear relationship between plastic rotation and drift ratio.

Assuming plane section behavior and uniform strain over the height of the fiber section element, plastic tensile strain in the outermost longitudinal reinforcement, $\varepsilon_{p,t}$, is:

$$\varepsilon_{p,t} = \varepsilon_s - \varepsilon_y = \phi_p(d - c) = \frac{\theta_p}{L_p}(d - c) \approx \frac{\Delta_p/H}{L_p}(d - c) = \frac{\Delta_p/H}{L_{gap} + Cd_b}(d - c) \tag{4-3}$$

where ε_s is the tensile strain in the outermost tensile longitudinal reinforcement, ε_s is the yield strain of the outermost tensile longitudinal reinforcement, ϕ_p is the plastic curvature, d is the depth to the outermost tensile longitudinal reinforcement, and c is the neutral axis depth. Similarly, the plastic compression strain in the outermost longitudinal reinforcement, $\varepsilon_{p,c}$, is:

$$\varepsilon_{p,c} = \varepsilon_s - \varepsilon_y = \phi_p(c-d') = \frac{\theta_p}{L_p}(c-d') \approx \frac{\Delta_p/H}{L_p}(c-d') = \frac{\Delta_p/H}{L_{gap}+Cd_b}(c-d') \quad (4\text{-}4)$$

where d’ is the compression strain in the outermost compressive longitudinal reinforcement and L_p is from Equation (4-2) based on the recommendation by Chai et al (1994).

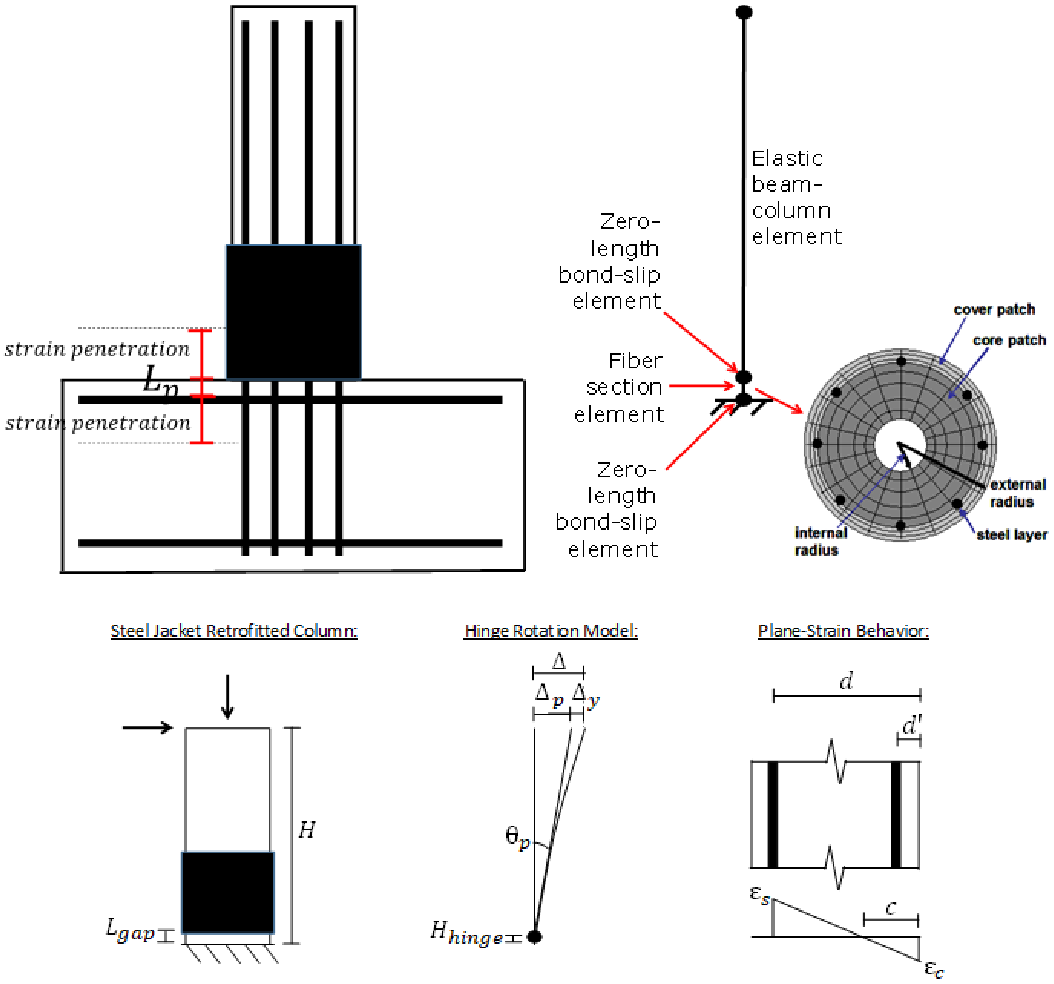

Figure 4.1. Column Deformation Model

The column model was formulated in OpenSees (McKenna, year) as a linear elastic beam element with a displacement based fiber element of length L_p = 1-in. The model is intended to be efficient for use in nonlinear time history analyses and enabled the recording of stress and strain in longitudinal reinforcement. In this manner the strain history in the longitudinal reinforcement could be directly related to the drift history of the column, without needing to explicitly implement Equations (4) and (5) in the code.

The stiffness of the unjacketed column was determined using the method of Elwood and Eberhard (2009), which accounts for the contribution from flexure, shear, and bond slip as:

$$\Delta = \Delta_{flexure} + \Delta_{slip} + \Delta_{shear} \tag{4-5}$$

$$\Delta_{flexure} = \frac{H^2\phi_y}{3} \tag{4-6}$$

$$\Delta_{slip} = \frac{Hd_b f_y \phi_y}{8u} = \frac{Hd_b f_y \phi_y}{8\left(9.6\sqrt{f_c'}\right)} \tag{4-7}$$

$$\Delta_{shear} = \frac{M_y}{A_v G_{eff}} = \frac{M_y}{(0.85D)(0.2E_c)} \tag{4-8}$$

where H is the height of the column, is the yield curvature, d_b is the diamater of longitudinal reinforcement, fy is the yield strength of longitudinal reinforcement, u is the bond stress, M_y is the yield moment, A_v is the area of the cross-section resisting shear, D is the diamater of the column, G_{eff} if the effective shear modulus, and E_c is the modulus of elasticity of concrete. M_y was determined from moment-curvature analysis at first yield of reinforcement. For the bond slip contribution, Zhao and Sritharan (2007) was used in place of Eq. (5-8):

$$\Delta_{slip} = 0.1\left[\frac{d_b f_y}{4\sqrt{f'c}}(2\alpha+1)\right]^{\frac{1}{\alpha}} + 0.013 \tag{4-9}$$

where α is the parameter used in local bond-slip relation and was taken as 0.4 as done in Zhao and Sritharan (2007). The increase in stiffness from the FRP jacket was determined using the approach recommended by Chai et al (1994) for steel jackets, which accounts for the bond transfer length needed to develop full composite action of the jacket and column. As this was an FRP jacket, the gap length, L_{gap}, and grout thickness, t_{grout}, were both zero. The CFRP jacket cured composite tensile modulus and tensile strength shown in Table 3.5 were used in place of the steel jacket elastic modulus and yield strength. Once the stiffness of the column, *k*, was determined, it was implemented into the model as the elastic flexural rigidity, $(EI)_{elastic}$, of the elastic element, computed as:

$$(EI)_{elastic} = \frac{\frac{M_y}{H}\left(H - \frac{L_{gap}}{2} - \frac{L_p}{2}\right)^3}{3\Delta_{elastic}} = \frac{\frac{M_y}{H}\left(H - \frac{L_{gap}}{2} - \frac{L_p}{2}\right)^3}{3\left(\frac{M_y}{Hk} - \phi_y L_p\left(H - \frac{L_{gap}}{2}\right)\right)} \tag{4-10}$$

where M_y and ϕ_y was determined from moment-curvature analysis using the Mander et al (1988) confined concrete model. This computation of $(EI)_{elastic}$ accounts for the flexibility in the fiber element based on the displacement at yield due to curvature in the fiber, such that the elastic stiffness in the model is expected to match the computed value for *k* at yield.

Concrete was modeled using Concrete02 in OpenSees. The Mander et al (1988) model for confined concrete was used to determine the confined concrete compressive strength, f'_{cc}, and the strain at which f'_{cc} is reached, ε_{cc}. The ultimate concrete stress and strain were modeled as $0.2f'_{cc}$ and $5\varepsilon_{cc}$, respectively. λ in the Concrete02 model, which is the ratio between unloading slope and initial slope, was taken as 0.1.. Reinforcement was modeled using ReinforcingSteel, with the tangent at initial strain hardening taken as $0.01E_s$. Strain hardening was initiated at ε_{sh} and strain at peak stress was reached at ε_{ult}. Reinforcement in the bond-slip elements was modeled with Bond SP01. Yield slip, s_y, was computed using Eq. (5-8) from Elwood and Eberhard (2008) utilizing the yield curvature determined from a moment-curvature analysis of the column not accounting for confinement. Slip at ultimate strength, s_u, was taken as 30 times the yield slip, consistent with Zhao and Sritharan (2007). The values for initial hardening slope in the monotonic slip versus bar stress response, b, and the pinching factor for the cyclic slip versus bar response, R, were taken as 0.3 and 0.7, respectively.

The stress-strain response of the outermost longitudinal reinforcement at both ends of the column was recorded during the OpenSees analysis. The strain history of the reinforcement was then implemented in an existing low-cycle fatigue model that was used to estimate the point of fracture of the outermost longitudinal bar based on the accumulated plastic strain. The low-cycle fatigue model was implemented in Matlab, such that failure was determined through post-processing of the data collected from the OpenSees analysis.

Modeling of low-cycle fatigue was based on the Coffin (1954 and 1971) and Manson (1965) formulation:

$$\varepsilon_p = \varepsilon_0 \left(2N_f\right)^{-m} \tag{4-11}$$

where ε_p is the plastic strain amplitude of each constant amplitude half cycle, ε_0 is a material constant that approximately indicates the plastic strain amplitude at which one half cycle will cause failure, $2N_f$ is the number of constant amplitude half cycles to failure, and m is a material constant that indicates the sensitivity between ε_i and N_f. Equation (4-11) may be re-arranged to determine the number of constant amplitude half cycles at ε_p needed to reach failure:

$$2N_f = 10^{(-m)^{-1}\log\left(\frac{\varepsilon_p}{\varepsilon_0}\right)} \tag{4-12}$$

The accumulation of damage was based on Minor's Rule:

$$DI = \sum \frac{2n_i}{2N_f} \tag{4-13}$$

where $2n_i$ is the number of half cycles at a specific value of ε_p, and $2N_f$ is determined for that same value of ε_p using Equation (4-12). For an individual half cycle, $2n_i = 1$, such that the damage of each half cycle is $(2N_f)^{-1}$. When the accumulation of half-cycles causes the damage index, DI, to exceed 1.0, fatigue failure occurs. Although rainflow counting is often used to define full cycles, the use of half-cycles enables the analysis to progress sequentially without a need for rainflow counting. In this case, a half-cycle is defined to be bounded by two load reversals, such that the amplitude of a half cycle is one-half of the strain bounded by two load reversals.

4.2. Results and Discussion

The method to compute the stiffness of each column, described in the previous section, was validated to data from the column tests described in Chapter 4. The stiffness values from the model and test data are provided in Table 4.1 for each test. The stiffness from test data was consistent with the values in Table 3.13, which were determined from fitting a backbone model to test data, as desribed in Section 3.2.3. It is evident from Table 4.1 that the model predicted the stiffness with a percent error that was less than 25% for all tests. The average percent error was 2.04% in the positive direction (i.e., overprediction of stiffness). Given the level of variability in stiffness observed in the tests, the use of this method to determine stiffness was deemed appropriate.

Table 4.1: Effective Stiffness from Model and Tests

Column Name	Effective Stiffness		
	Test [kip/in]	Model [kip/in]	% Error
C-#7(1.3)-0.05	77.5	89.63	15.65
C-#5(1.4)-0.05	95.53	98.19	2.78
C-#7(2.7)-0.05	103.715	115.65	11.51
C-#7(1.3)-0.05-EQ	82.34	89.63	8.85
C-#7(1.3)-0.05-X	92.465	89.63	-3.07
C-#7(1.3)-0.15	131.145	100.34	-23.49

The model was validated to the six columns tested in this study, which were described in Chapter 4. The fit between model and tests is provided in Figure 4.2. The model provided a reasonable fit to the test data, with the exception of an underestimate of the strength for x and an overestimate of the level of pinching in the load-deformation hysteresis of x. The model did not capture the strength degradation observed in the test of C(CFRP)-#7(1.3)-0.15, as damage occurred above the jacketed region. The model prediction of fracture of the first longitudinal bar is indicated in the figures. The model under predicted fracture for each of the six tests.

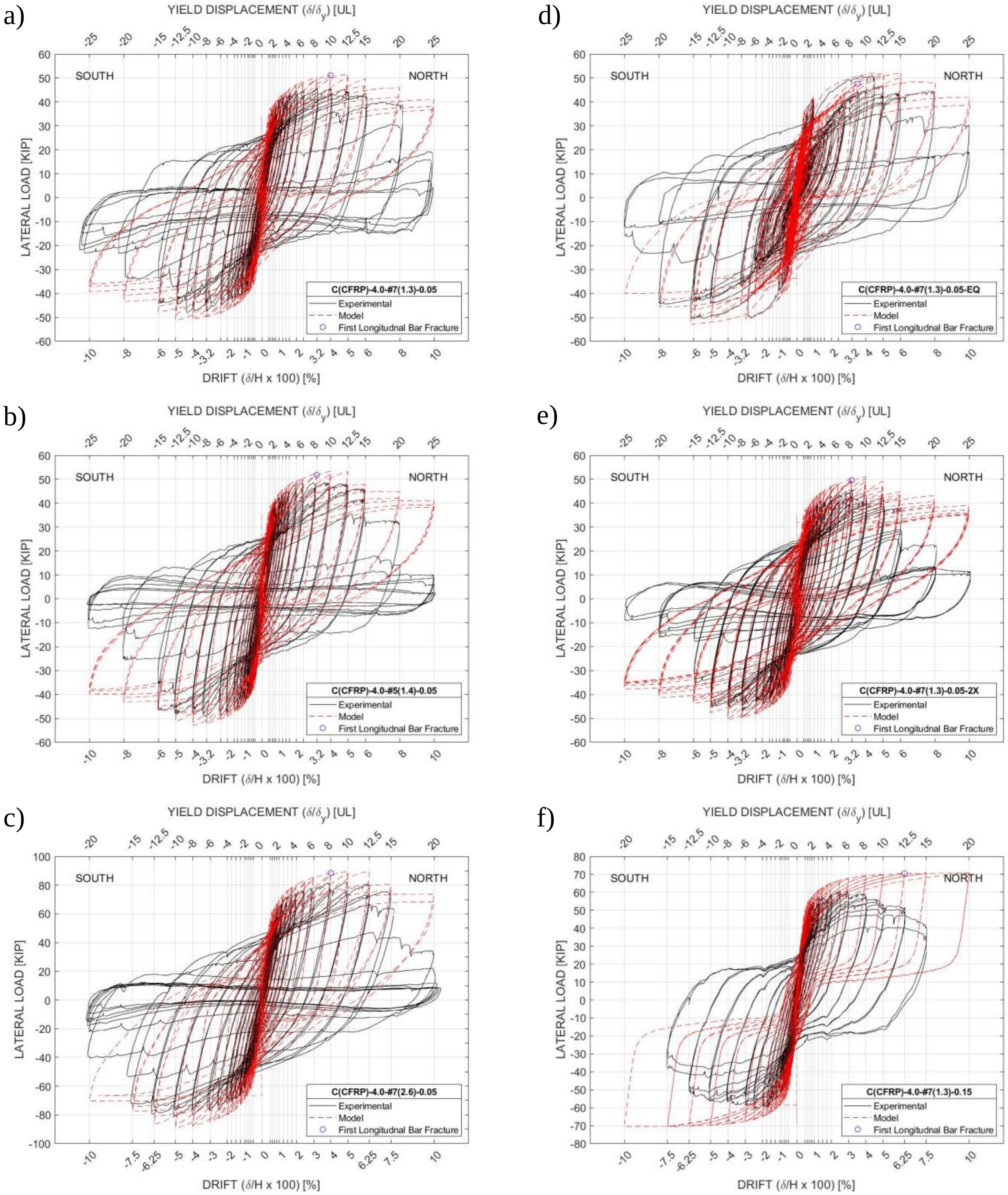

Figure 4.2. Column Load-Deformation Response for Model and Tests: a) C(CFRP)-4.0-#7(1.3)-0.05, b) C(CFRP)-4.0-#5(1.4)-0.05, c) C(CFRP)-4.0-#7(2.7)-0.05, d) C(CFRP)-4.0-#7(1.3)-0.05-EQ, e) C(CFRP)-4.0-#7(1.3)-0.05-2X, f) C(CFRP)-4.0-#7(1.3)-0.15

5. Conclusions

Retrofit of reinforced concrete bridge columns with jackets is a commonly implemented strategy to increase column ductility in earthquakes. Six FRP jacket retrofitted reinforced concrete bridge columns were designed, constructed and tested. Five of the six columns were nominally identical to a set of recently tested steel jacket retrofitted columns. Test variables included bar size of longitudinal reinforcement, longitudinal reinforcement ratio, axial load ratio, and loading protocol, with inclusion of a variable amplitude earthquake time history for one of the columns. These test variables were selected due to the influence on the strain history in the longitudinal reinforcement, as strength degradation in the test columns was expected to be due to fatigue fracture of longitudinal reinforcement. The range of values for the test variables was intended to reflect the range of variation of these parameters in the Washington State DoT inventory.

Using test results from the columns and reinforcement tests, a model was developed to estimate the load-deformation response and fatigue fracture of longitudinal reinforcement in steel jacket retrofitted reinforced concrete columns. The model consisted of a linear elastic element with a plastic hinge at the base. The plastic hinge length included the gap between the bottom of the steel jacket and the footing as well as additional length to account for bond slip of reinforcement due to strain penetration into the footing and into the steel jacketed region. Strain history determined from the model was used in an existing fatigue model to estimate the drift at fatigue fracture of longitudinal reinforcement. The model was validated with existing test data.

The following conclusions on FRP jacket retrofitted reinforced concrete bridge columns were reached:

- Concrete damage is limited to the cover concrete at the top of the footing. Cracking concentrated at the column-footing interface, and the crack at this location became wide at increased deformation demand levels. This crack is indicative of bond slip of longitudinal reinforcement. The extent of spalling of cover concrete at the top of the footing varied for the test columns, with the extent of damage most limited for the column with the largest axial load.
- Fracture of the first longitudinal bar in the test columns occurred during cycles at 12.5 or 15.0 times the yield displacement. Axial failure was reached for one of the test columns upon fracture of the final longitudinal bar. This occurred at 20.0 times the yield displacement, which was a drift of 10% for these two columns.
- Minimal pinching, indicative of favorable hysteretic energy dissipation, was observed in the load-deformation responses of the test columns. Strength degradation was primarily due to low-cycle fatigue fracture of longitudinal reinforcement.
- Peak base moment on the column was larger by as much as 40% for the test column with variable amplitude earthquake protocol. The largest excursions in the earthquake protocol were associated with a significant reduction in strength upon the next occurrence of reaching this drift level, and larger drift in the excursion was associated with a larger reduction in strength. The level of strength drop observed for this test prior to bar fracture was not observed in tests with fully reserved cyclic protocols prior to bar fracture, and this is attributed to the difference in cycle content.

- 90% of column deformation was attributable to bond slip of longitudinal reinforcement. The next greatest contribution was column sliding shear at the footing--column interface. Flexure and shear deformation in the retrofit columns, beyond the plastic hinge region, were minimal, becoming increasingly insignificant at larger drifts. Measured curvature over a distance of 0.5” to 8.0” above the column base was significantly larger than locations further up in the column. This was indicative of yielding, lack of composite action, or both, at this location.
- Lateral failure was defined to have occurred when the lateral load at a maximum cycle peak first dropped below 20% of the peak lateral load and did not return to this level during subsequent cycles. A maximum cycle peak is defined as a cycle peak that was greater than or equal to any previous peak in that loading direction. Lateral failure corresponded to fracture of the first longitudinal bar. All test columns reached 12.5 to 15.0 times the yield displacement prior to lateral failure.
- The predicted stiffness used in the model matched the measured stiffness from the test columns with a percent error that was less than 25% for all tests and an average percent error of 2.04% overprediction. Overall, the retrofitted column model provided a reasonable fit to test data with an underprediction of first bar fracture.

References

ACI 374.2R-13 (2013). “Guide for Testing Reinforced Concrete Structural Element under Slowly Applied Simulated Seismic Loads”. American Concrete Institute, Farmington Hills, Michigan.

ACI 440.2R-17 (2017). “Guide for the Design and Construction of Externally Bonded FRP Systems for Strengthening Concrete Structures”. American Concrete Institute, Farmington Hills, Michigan.

Atwater, B. F., Nelson, A. R., Clague, J. J., Carver, G. A., Yamaguchi, D. K., Bobrowsky, P. T., Bourgeois, J., Darienzo, M. E., Grant, W. C., Hemphill-Haley, E., Kelsey, H. M., Jacoby, G. C., Nishenko, S. P., Palmer, S. P., Peterson, C. D., and Reinhart, M. A. 1995. “Summary of Coastal Geologic Evidence for Past Great Earthquakes at the Cascadia Subduction Zone.” Earthquake Spectra, 11(1), 1–18.

Breña, S. F., and Schlick, B. M. (2007). "Hysteretic Behavior of Bridge Columns with FRP Jacketed Lap Splices Designed for Moderate Ductility Enhancement." Journal of Composites for Construction, 11(6): 565-574.

Buckle, I.G. (1994). The Northridge, California Earthquake of January 17, 1994: Performance of Highway Bridges. Technical Report NCEER-94-0008, National Center for Earthquake Engineering Research, State University of New York at Buffalo, Buffalo, NY, 136 pp.

Chai, Y.H., Priestley, M.J.N., and Seible, F. (1991). Seismic Retrofit of Circular Bridge Columns for Enhanced Flexural Performance. ACI Structural Journal, 88(5): 572-584.

Chai, Y.H., Priestley, M.J.N., and Seible, F. (1994). Analytical Model for Steel-Jacketed RC Circular Bridge Columns. Journal of Structural Engineering, 120(8): 2358-2376.

EERI (1990). Loma Prieta Earthquake Reconnaissance Report-(Supplement to Volume 6). Earthquake Spectra, Earthquake Engineering Research Institute, 448 pp.

EERI. (1994). Northridge Earthquake January 17, 1994, Preliminary Reconnaissance Report," No. 94-01, J. F. Hall, ed., Earthquake Engineering Research Institute, Oakland, Calif., 1994, p. 104.

Federal Highway Administration. (2006). Seismic Retrofitting Manual for Highway Structures: Part 1 – Bridges. U.S. Department of Transportation, Federal Highway Administration, Research, Development, and Technology, McLean, VA.

Fung, G. G., Lebeau, R. J., Klein, E. D., Belvedere, J., and Goldschmidt, A. F. (1971). Field Investigation of Bridge Damage in the San Fernando Earthquake. Technical Report, Bridge Department, Division of Highways, California Department of Transportation, Sacramento, CA, 209 pp.

Ghosh, K. K., and Sheikh, S. A. (2007). “Seismic upgrade with carbon fiber-reinforced polymer of columns containing lap-spliced reinforcing bars.” ACI Structural Journal, 104(2): 227-236.

Goldfinger, C., Nelson, C. H., Morey, A. E., Johnson, J. E., Patton, J. R., Karabanov, E., Gutiérrez-Pastor, J., Eriksson, A. T., Gràcia, E., Dunhill, G., Enkin, R. J., Dallimore, A., and Vallier, T. (2012). Turbidite Event History—Methods and Implications for Holocene Paleoseismicity of the Cascadia Subduction Zone, U.S. Geological Survey Professional Paper 1661–F, 170 p.

Haroun, M. A., and Elsanadedy, H. M. (2005a). "Behavior of Cyclically Loaded Squat Reinforced Concrete Bridge Columns Upgraded with Advanced Composite-Material Jackets". Journal of Bridge Engineering, 10(6): 741-748.

Haroun, M. A., and Elsanadedy, H. M. (2005b). "Fiber-Reinforced Plastic Jackets for Ductility Enhancement of Reinforced Concrete Bridge Columns with Poor Lap-Splice Detailing". Journal of Bridge Engineering, 10(6): 749-757.

Huang, Y. and Mahin, S. A. (2010). “Simulating the inelastic seismic behavior of steel braced frames including the effects of low-cycle fatigue.” PEER Report 2010/104, University of California, Berkeley, CA.

Kanvinde, A. (2004). “Micromechanical simulation of earthquake-induced fracture in steel structures.” PhD Dissertation, Stanford University, Stanford, CA.

Krawinkler H. (1992). Guidelines for Cyclic Seismic Testing of Components of Steel Structure, ATC-24. Redwood City, California: Applied Technology Council.

Mander, J.B., Priestley, M.J.N., and Park, R. (1988). Observed Stress-Strain Behavior of Confined Concrete. Journal of Structural Engineering, 114(8): 1827-1849.

National Institute of Standards and Technology. (1990). Performance of Structures during the Loma Prieta Earthquake of October 17, 1989. NIST Publication 778, Jan. 1990.

Padilla-Llano, D. A., Hajjar, J.F., Eatherton, M.R., Easterling, S.W., and Schafer, B.W. (2018). "Cyclic fracture simulation framework for stability and collapse simulation in steel structures," Proc. of the Structural Stability Research Council, Baltimore, MD.

Priestley, M. J. N., and Seible, F. (1991). "Seismic assessment and retrofit of bridges." Struct. Sys. Res. Pro)., Rep. No. SSRP·91/103, University of California at San Diego, Calif.

Priestley, M.J.N., Seible, F., Xiao, Y., and Verma, R. (1994a). Steel Jacket Retrofitting of Reinforced Concrete Bridge Columns for Enhanced Shear Strength—Part 1: Theoretical Considerations and Test Design. ACI Structural Journal, 91(4): 394-405.

Priestley, M.J.N., Seible, F., Xiao, Y., and Verma, R. (1994b). Steel Jacket Retrofitting of Reinforced Concrete Bridge Columns for Enhanced Shear Strength—Part 2: Test Results and Comparison with Theory. ACI Structural Journal, 91(5): 537-551.

Uriz, P., and Mahin, S.A. (2008). Toward Earthquake-Resistant Design of Concentrically Braced Steel-Frame Structures. PEER Report 2008/08, Pacific Earthquake Engineering Research Center, College of Engineering, University of California, Berkeley, CA, 401 pp.

Xiao, Y., and Ma, R. (1997). Seismic Retrofit of RC Circular Columns Using Prefabricated Composite Jacketing. Journal of Structural Engineering, 123(10): 1357-1364.